Searches for proton radioactivity from highly-deformed nuclei

Peter Munro MSci (Hons.)

Thesis submitted for the degree of Doctor of Philosophy in the College of Science and Engineering

School of Physics

University of Edinburgh

2006

Abstract

Proton radioactivity from the highly neutron-deficient nuclide ^{135}Tb has been identified using a new double-sided silicon strip detector (DSSD) system at the Fragment Mass Analyser at Argonne National Laboratory. The decay occurs with an energy of $E_p = 1179(7)$keV and a half-life $t_{1/2} = 940^{+320}_{-220}\mu$s. ^{135}Tb was produced via the bombardment of a ^{92}Mo target with a 315MeV ^{50}Cr beam, and is the first isotope to be detected from a (p6n) evaporation channel in heavy ion fusion-evaporation reactions. Proton decay rate calculations suggest that this nuclide has a large prolate deformation, in agreement with the predictions of the Möller-Nix mass model and the experimental observations of the neighbouring odd-even lanthanide proton emitters ^{131}Eu and ^{141}Ho.

An unsuccessful search for the predicted proton emitters ^{125,126}Pm, using the (p6n) and (p5n) evaporation channels respectively, is also reported. The non-observation of ^{126}Pm is consistent with mass model Q_p predictions, but the non-observation of proton emission from ^{125}Pm suggests a Q_p value which differs significantly from predictions, or places an upper limit on the production cross-section of this nucleus.

The Q_p predictions of the Möller-Nix and Liran-Zeldes mass models are compared with the currently available data set of experimentally-derived Q_p values for proton-unbound nuclei in the region of observed proton radioactivity. Both models are found to perform reasonably well and provide useful predictions in this extremely neutron-deficient region.

Declaration

This thesis has been composed by myself.

The experimental work described in this thesis was performed by myself and fellow collaborators; the data analysis is my own work.

No portion of the work referred to in this thesis has been submitted in support of an application for another degree qualification of this or any other university or other institute of learning.

Acknowledgements

Thanks to the following colleagues and collaborators: Cary Davids, Tom Davinson, Nick Harrington, Zhong Liu, Hassan Mahmud, the late Tad Pennington, Andrew Robinson, Ewan Roche, Dariusz Seweryniak and my supervisor Professor Phil Woods.

Funding for this PhD research was provided by the Engineering and Physical Sciences Research Council (EPSRC).

Thanks to Emily and my parents.

Contents

List of Figures

List of Tables

Chapter 1

Introduction

1.1 Exotic Nuclei

The ultimate limits of nuclear stability for exotic neutron-deficient or neutron-rich nuclides are defined by the proton and neutron drip-lines: the points at which it becomes energetically possible for a nucleus to spontaneously emit a nucleon from its ground state, with the Q-value of this decay mode given by the proton or neutron separation energy. All isotopes beyond the drip-lines are therefore unbound, but some isotopes which are close to the proton drip-line may still exist for a long enough time for their properties to be investigated experimentally, due to the hindrance effect of the Coulomb barrier on the emission of a charged particle. The study of such exotic nuclei is more challenging than the study of nuclei close to stability because the nuclear half-life reduces rapidly as one moves further from the valley of stability. Figure 1.1 shows the chart of nuclides, a plot of atomic number Z against neutron number N, with the stable isotopes represented as

black squares and the various possible decay modes represented by colours. For stable nuclei of low mass A, the ratio of neutrons to protons is $\sim$1, but increases significantly with increasing mass due to the mutual Coulomb repulsion between the protons in the nucleus, so that the heaviest known stable nuclei have a neutron-to-proton ratio of >1.5. The Coulomb force also causes the proton drip-line to be much closer to the valley of stability than its neutron counterpart.

On each side of the valley of stability are regions where nuclei decay via the weak interaction by emission of a β particle (an electron for the neutron-rich side or a positron for the neutron-deficient side) and a neutrino, which converts a proton to a neutron or vice versa. Proton-rich nuclei may also capture an atomic electron to convert a proton to a neutron. β decay has the effect of moving the nucleus towards the valley of stability without changing its number of nucleons: the energy available for the decay process comes from the difference between the binding energies of the parent and daughter nuclei. The available decay energy increases further from stability, meaning that the decay process occurs on a faster timescale (i.e. the decay half-life decreases). Other decay modes become possible far from stability, such as β-delayed nucleon emission, where the β decay of a precursor nucleus populates an excited state in the daughter so high in energy that it is unbound to the emission of one or more particles. β-delayed emission of protons, neutrons and α particles, which occurs on a similarly fast timescale to the γ decay of the excited states, has been studied extensively [Poe89]. For most medium to heavy nuclei, the density of excited states in the unbound region is so high that it is virtually impossible to identify individual states from peaks in the particle energy spectra with the available experimental resolution.

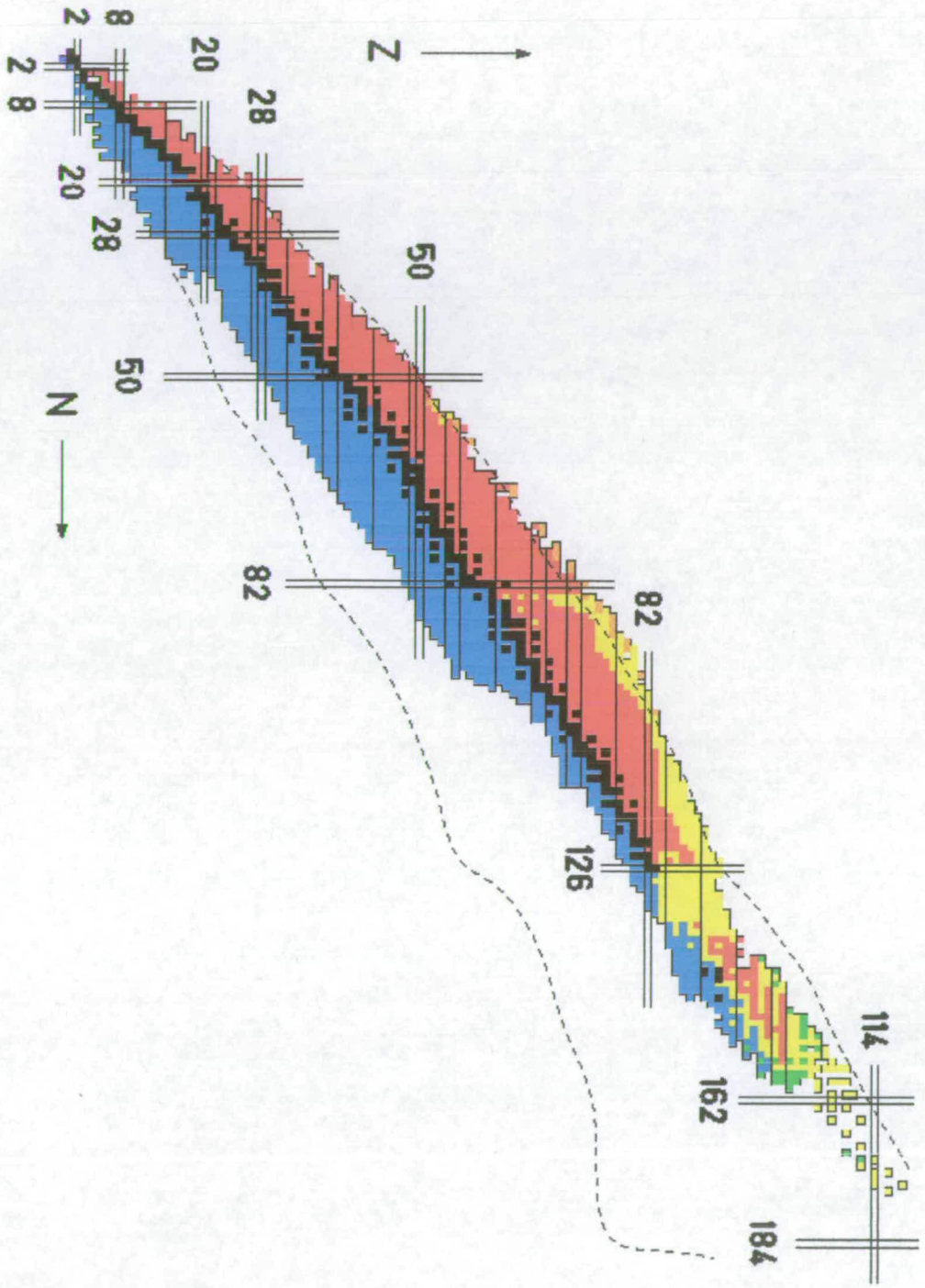

Figure 1.1: *Plot of atomic number Z against neutron number N for the known nuclides, illustrating the stable nuclides (as black squares), the proton and neutron drip-lines, and the various possible decay modes (red for β^+/electron capture, blue for β^- decay, yellow for α decay, gold for proton decay and green for spontaneous fission).*

The Coulomb energy is proportional to Z^2, while the nuclear binding energy increases approximately with the mass number A, meaning that the Coulomb repulsion becomes proportionally more important for heavier nuclei, particularly on the neutron-deficient side of stability. This repulsion can result in the spontaneous emission of a tightly-bound α particle becoming competitive (in terms of decay rate) with the β-decay process. α decay is extremely sensitive to the available decay energy, much more so than β decay, and becomes the dominant decay mode for proton-rich isotopes above the Z=82 shell closure. α decay has not been observed in the particular mass region studied in this work ($125 \leq A \leq 135$), but several heavier proton emitters have a significant α-decay branch. Similarly, spontaneous nuclear fission may be a competitive decay mode for heavy proton emitters, but is not an issue for the medium mass region investigated in this work.

It is possible for nuclei beyond the proton drip-line to decay by emission of a proton from their ground state, although this is not seen immediately beyond the drip-line for nuclei with $Z > 50$ because the available decay energy is not large enough for the mode to become competitive with β or α decay. Proton emission does not usually become the dominant decay mode until the drip-line is crossed by several isotopes, when the proton partial half-life has dropped below those of the competing modes. Proton decay is a similar process to α decay in that a particle has to tunnel through a potential barrier to escape the nucleus, but the former requires no preformation of a cluster of nucleons within the nucleus, so is easier to model theoretically. The potential barrier has a Coulomb component, which is relatively less important for protons than for alphas because of their lower charge, and a centrifugal component related to the angular momentum carried away by

the particle which is more important for protons because of their lower mass than alphas. The hindrance effect of the Coulomb barrier is sufficient for heavier nuclei (Z>50) to slow the proton decay rate to an experimentally detectable timescale ($> 1\mu s$).

The study of proton emission is in fact a very useful tool for studying the structure of these exotic drip-line nuclides. The proton decay rate is extremely sensitive to the orbital angular momentum of the unbound proton, so that an accurate measurement of the half-life can often identify the particular single-particle orbital of the odd proton by comparison with a theoretical calculation and thus shed light on the level orderings of these extremely neutron-deficient nuclei. Proton emission also turns out to be sensitive to the nuclear shape: several proton emitters have been found in regions far from the 'magic numbers' of shell closures and are predicted to have significant quadrupole deformations (prolate, like a rugby ball, or oblate like a discus). The measurement of the energy of the emitted proton also yields the one-proton separation energy of the parent, which in turn directly relates to its binding energy and mass, providing very useful data to allow comparisons with the predictions of mass models. This new data can be incorporated into these models to improve them further. In this very neutron-deficient region of nuclides, proton decay studies are often the only way of gaining this kind of information.

All the ground state proton emitters discovered so far are odd-Z nuclides; this is not surprising, given that the natural pairing of nucleons makes the emission of a single proton from an even-Z nucleus very unlikely energetically. However, examples of simultaneous emission of two protons have recently been observed experimentally and will be discussed later.

The region around the proton drip-line up to around Z=50 is also of interest in nuclear astrophysics studies, particularly the nucleosynthesis of the heavier elements in explosive stellar environments such as X-ray bursters. Many of the properties of the rapid proton, or 'rp', capture process which occurs in stars can also be investigated in nuclear physics experiments on Earth. The rates at which these reactions occur (which again relate to the tunneling of a particle through a nuclear Coulomb barrier) are intrinsically linked with the elemental abundances of the universe. It is unlikely that the rp process proceeds as far as the particular mass region investigated in this work, due to the small region of α-emitting isotopes close to the proton drip-line above Z=50.

The study of nuclei at the neutron drip-line is extremely difficult for all but the lowest-Z isotopes. The absence of Coulomb repulsion ensures that the neutron drip-line is much further from stability than the proton drip-line, and is therefore often more difficult to access in terms of experimental production of the isotopes. Also, because neutrons have no charge, they experience no Coulomb component in the potential barrier they must tunnel through, and therefore can tunnel at rates too fast for detection with current experimental techniques. Even if the decay occurs on a suitable timescale, the difficulty of detecting the uncharged neutron (compared with the ease of detecting the charged proton in convenient solid state detectors) makes it very difficult to measure meaningful physical quantities. The neutron drip-line has been mapped only as far as Z=9 thus far, compared with the virtually complete mapping of the proton drip-line for odd-Z nuclei up to Z=50. Interesting phenomena in the highly neutron-rich region include the 'halo' nucleus ^{11}Li [Tan85], where two very loosely bound valence neutrons

cause the nucleus to have an extremely wide matter radius. Similar halo effects in proton-rich nuclei are suppressed by the Coulomb barrier, but have recently been observed in nuclei such as ^{17}Ne [Kan05].

1.2 Production of Proton Drip-line Isotopes

The key issues for experimenters searching for new proton emitters are producing the desired exotic isotope in sufficient quantities and being able to detect its subsequent decay, which may occur on a very fast timescale (perhaps on the order of microseconds). These extremely neutron-deficient nuclei obviously do not occur in nature, and must be produced in experiments at accelerator facilities.

Several different types of nuclear reaction have been used to generate nuclei at or beyond the proton drip-line. Transfer reactions, such as (^{4}He,^{8}He), can be useful for producing light exotic nuclei, due to the close proximity of the proton drip-line to stability at low Z, but are of little use in the mass region of ground-state proton emitters. Proton-induced target spallation has been used at CERN-ISOLDE to study proton-rich nuclei, but the value of this method is limited by the long ion release times (hundreds of milliseconds) relative to the half-lives of drip-line nuclei (usually on the order of milliseconds or less). Projectile fragmentation reactions have been used successfully, for example at the GANIL facility, to map most of the proton drip-line up to A=100. In these experiments, a high energy (>100MeV/u) neutron-deficient beam is fragmented on a target and the resulting fragment ions can be identified by time-of-flight and energy loss techniques. Fragmentation was recently used to detect the first ever example of simultaneous

two-proton emission (see next section), and it is thought that it could be useful for accessing predicted heavy proton emitters for which spontaneous nuclear fission is a competitive decay branch.

All the presently known examples of ground-state one-proton emission, occuring in the medium-heavy mass region of 100 <A< 190, have been detected using heavy ion fusion-evaporation reactions. In this case, a neutron-deficient beam, with energy on the order of 5-10MeV/u, is projected at a thin neutron-deficient target. The beam and target nuclei fuse together to create a highly-excited compound nucleus, which reduces its energy by quickly 'evaporating' off nucleons. These recoiling fusion-evaporation residues pass out of the target and can be analysed by mass separation techniques and then implanted into a solid state detector to measure their subsequent decays. Fusion-evaporation reactions preferentially populate high spin excited states in the recoils, which has aided in the discovery of proton-emitting isomeric states as well as ground states. A significant problem for these reactions is that protons evaporate preferentially over neutrons in this region, pushing the residues further from the drip-line, so the beam energy must be carefully controlled to excite the compound nucleus with just the right energy to optimise the necessary evaporation channel for production of the desired nuclide. Even so, this nuclide is likely to be produced with a much lower cross-section than many of the other possible evaporation residues. Most of these other recoils, and many unreacted primary beam particles which have passed straight through the target, can be removed at the mass separation stage, thus reducing the potentially crippling background. The separation stage must also unambiguously identify the recoil so that its subsequently detected decay can be clearly correlated to its parent.

Table 1.1: *Reactions producing proton-emitting isotopes.*

Reaction	Production cross-section	Year discovered
^{92}Mo(^{58}Ni, p2n)^{147}Tm	$\sim 30\mu$b	1982
^{96}Ru(^{58}Ni, p2n)^{151}Lu	$\sim 50\mu$b	1982
^{96}Ru(^{58}Ni, p3n)^{150}Lu	$\sim 5\mu$b	1993
^{92}Mo(^{58}Ni, p3n)^{146}Tm	$\sim 1\mu$b	1993
^{92}Mo(^{58}Ni, p4n)^{145}Tm	~500nb	1997
^{92}Mo(^{54}Fe, p4n)^{141}Ho	~250nb	1997
^{64}Zn(^{58}Ni, p4n)^{117}La	~240nb	2001
^{96}Ru(^{40}Ca, p4n)^{131}Eu	~90nb	1997
^{92}Mo(^{54}Fe, p5n)^{140}Ho	~13nb	1999
^{58}Ni(^{78}Kr, p5n)^{130}Eu	~10nb	2001

All the known proton emitters have been discovered by T(B,pxn) reactions, where T is the target isotope, B is the beam species and 'pxn' represents one proton and a certain number of neutrons being evaporated from the compound nucleus. A table comparing the production cross-sections of various proton emitters from these reactions is shown below.

1.3 Proton Radioactivity Search Experiments

1.3.1 Early experiments

It was initially expected in the 1960s that prompt (i.e. not β-delayed) proton emission would be quite common from isomeric states of isotopes which were proton-bound in their ground state. Such nuclides would be closer to the valley of stability and therefore easier to produce, but competition from γ decay and high centrifugal barriers complicated these first search experiments. The only example of direct proton emission below A=100 was detected as a surprising result of a β-delayed proton experiment. A 1.5MeV

proton was observed from a high-spin isomer ^{53m}Co [Jac70, Cer70], which until very recently was the only example of isomeric direct proton emission from a ground state proton-bound nucleus. These early experiments were hampered by the limited species and currents of the available beams.

A decade passed before the discovery of the first ground-state proton emitters at the GSI facility. Improvements in ion source and accelerator technology meant that heavy ion beams could now be used effectively, and Hofmann *et al* [Hof82a] detected the proton decay of ^{151}Lu using the reaction ^{96}Ru(^{58}Ni,p2n) and the velocity filter SHIP [Mun79]. The in-flight separation of the recoils from the primary beam occurs on a timescale of about a microsecond, after which the recoils are implanted into an array of position-sensitive silicon detectors. Implant-decay correlations were recorded by noting decays occuring within a certain time window at the same position as a preceding implant. The sensitivity of the system to short half-lives was improved by cycling the beam (5ms on, 15ms off), and longer half-lives could be investigated by completely blocking the residues from the detectors for periods of about 300ms. A clear peak was observed in the decay energy spectrum at an energy of ~1.2MeV, too low for an alpha decay process, with a half-life on the order of 80ms. The decay was assigned to the $h_{11/2}$ orbital of ^{151}Lu on the basis of measured production cross-sections and excitation functions: there was no explicit mass identification of the recoils in this experiment, and an attempted measurement at the neighbouring on-line mass separator (using the ISOL technique) was found to be impeded by background from the α decay of ^{151}Ho.

The GSI on-line mass separator was also used to detect the second ground state proton emitter, ^{147}Tm, which was discovered by Klepper *et al*

[Kle82] using the reaction ^{92}Mo(^{58}Ni,p2n). The indirect separation method of ISOL (implantation of the residues into a catcher foil in an ion source which then releases the residues into the separator) limits this experimental set-up to searching for nuclei with half-lives on the order of 100ms or above, but it does provide unambiguous mass identification of the ions. ^{147}Tm was found to decay by proton emission with energy 1.05MeV and half-life ~0.5s.

A team at the Technical University of Munich used a fast catcher detection system initially developed for γ-ray spectroscopy with an annular gas-filled detector built for α-particle measurement to search for proton emitters produced by reactions between ^{58}Ni beams and ^{58}Ni and ^{54}Fe targets. Faestermann *et al* reported the discovery of the lightest-known ground state proton emitters ^{109}I [Fae84] and also ^{113}Cs [Gil87]. This experimental set-up, although fast enough to detect decays down to 10ns, was inefficient compared to the GSI techniques and the lack of separation created an inevitable background which hindered the search for proton emitters with lower production cross-sections.

1.3.2 Experiments at Daresbury and Argonne

The major technological breakthrough in experimental searches for proton emitters was the combination of a double-sided silicon strip detector (DSSD) with an in-flight mass separator. A DSSD and its accompanying electronics were developed by the Edinburgh group [Sel92a] and installed at the Recoil Mass Separator (RMS) at Daresbury, where the system was successfully used to study many neutron-deficient isotopes in the early 1990s. Previous experiments using a position-sensitive silicon surface barrier detector [Woo89] were

not entirely successful due to the slow overload recovery of the system after an implantation event (about 200μs). The excellent energy and position resolution of the DSSD, combined with the ability of the system to restore its sensitivity to decays a short time after recoil implantation (<10μs) made the system extremely useful for such studies. The virtual transparency of the DSSD to β decay helped to produce very clean decay energy spectra from which a great amount of useful nuclear structure information was found.

The Daresbury RMS consisted of two Wien filters, which provided velocity selection of the recoils and rejected the primary beam, followed by a magnetic dipole which dispersed the residues according to their mass-to-charge (A/Q) ratios, so that the position of the recoil when it reached the focal plane (where the DSSD was positioned) was directly indicative of its A/Q. A carbon foil detector upstream of the focal plane was used to differentiate between implantation and decay events. The first use of this DSSD system was the remeasurement of the decay of ^{109}I [Sel93], which was directly shown to be a A=109 decay (the Munich team had no explicit mass identification) and was also correlated with the α decay of its daughter nuclide ^{108}Te. Other experiments were carried out to search for proton emission from isotopes such as ^{128}Pm, ^{132}Eu, ^{138}Tb, ^{142}Ho, ^{146}Tm, ^{156}Ta, ^{160}Re and ^{112}Cs, with the latter four successfully identified [Pag92, Liv93a, Liv93b, Pag94]. In addition, a proton transition which had been previously observed at GSI with no clear mass assignment was unambiguously identified as the decay of ^{150}Lu [Sel93].

The closure of the Nuclear Structure Facility at Daresbury in 1993 brought a temporary halt to this set of experiments, but soon after the Edinburgh group started collaborating with Argonne National Laboratory on

more DSSD-based proton radioactivity searches. The experimental set-up of the Argonne Fragment Mass Analyser (FMA) combined with the DSSD will be described fully in Chapter 3. This ongoing experimental programme has been extremely successful at discovering new proton-emitting states, including the proton decay of four isotopes of Iridium [Dav97, Mah02b], the first example of proton emission above the Z=82 shell closure in ^{185m}Bi [Dav96], and the proton decay of the rare earth isotopes ^{131}Eu and ^{141}Ho. These latter two are predicted by mass models [Mol97] to have large prolate deformation, and their anomalous decay rates (which do not agree with the theory for spherical nuclei) bear out that prediction. Other evidence for their deformation includes the observation of rotational bands in their proton-decay-tagged γ-ray spectra [Sew01a, Sew01b] and the observation of fine structure [Son99]. This latter phenomenon describes the proton decay branching to the first excited state of the daughter as well as the ground state, producing two peaks in the decay energy spectrum, and is characteristic of significant deformation in the daughter nucleus. It should be noted that experimental evidence for high deformations in neutron-deficient lanthanide isotopes was first discovered as far back as 1961 [She61], in the form of anomalous excitation energies in even-even nuclei.

More recent developments at Argonne include a focus on odd-odd proton emitters, where the decay process is influenced by the residual interaction between the outgoing proton and the odd neutron. Proton emission from isotopes such as ^{130}Eu [Dav04], ^{146}Tm [Rob05b], ^{150}Lu [Rob03] and ^{170}Au [Mah02b] have been studied in detail to better understand the effect of this interaction on the proton decay rate. As mentioned previously, decay-tagged γ-ray spectroscopy [Pau95] is possible when the Gammasphere detector is

installed around the target chamber, and such experiments have been performed on several proton emitters (e.g. ^{147}Tm [Sew97]), including the rare earths already discussed.

Experiments performed at the Argonne FMA facility in 2001 and 2002 form the core of this thesis, and will be discussed later.

1.3.3 Other experiments

In recent years, other research groups have performed successful search experiments for new proton emitters, most notably at Oak Ridge National Laboratory (ORNL) who first observed the fast proton decays of ^{140}Ho and ^{145}Tm [Ryk99, Bat98]. Using a familiar mass spectrometer/DSSD combination, the ORNL team have developed digital pulse analysis techniques, originally intended for γ-ray spectroscopy, which allows them to record the shape of the overloading recoil implantation energy pulse and identify fast proton decay events lying on the tail of the pulse while the electronics are still recovering from saturation. In the last few years the ORNL team have shown evidence for fine structure in ^{145}Tm and ^{146}Tm [Kar03, Gin03].

In 1999, a team based in Legnaro again used the mass spectrometer/DSSD technique to detect proton emission from the isotope ^{117}La [Sor01], a result which was soon confirmed by an experiment at Argonne. The Legnaro team have continued to search for candidate proton emitters such as ^{126}Pm [Sor03]. A team at the gas-filled separator RITU at Jyväskylä recently reported the observation of the new proton-emitting state ^{164m}Ir [Ket01]. RITU has a very high transmission efficiency compared to facilities such as the FMA due to its high charge state acceptance, and so is particularly use-

ful for investigating nuclei with low production cross-sections (for example, in the case of heavy nuclei where the compound nucleus produced by a fusion reaction has a high probability of spontaneous fission). However, RITU suffers from inferior mass separation characteristics compared to the FMA, which can hinder the mass identification of decays at the focal plane.

One of the most exciting recent developments in the field of proton-rich nuclei was the discovery of two-proton emission from the isotope ^{45}Fe via fragmentation reactions at the GANIL and GSI facilities [Gio02, Pfu02]. It has been hypothesised that a similar experimental approach could be used to detect heavy single proton emitters beyond Bismuth with the fragmentation of a ^{238}U beam, and a preliminary experiment exploring this method has been performed [Liu04].

Before the experiments described in this work took place, at least one example of a proton emitting isotope had been detected for every odd-Z element in the region 51 $\leq$Z$\leq$ 83, with the exception of Praseodymium, Prometheum and Terbium (Z=59, 61 and 65 respectively), although there remains some doubt as to the existence of a small (<1%) proton emission branch in the decay of ^{105}Sb observed by Tighe *et al* [Tig94], because several subsequent experiments have been unable to reproduce this result (including a DSSD-based experiment at the GSI on-line mass separator [Liu05]).

Chapter 2

Theory

Proton emission is a very pure example of quantum tunneling; unlike α decay, there is no need to consider the preformation of a compound particle within the nucleus. The unbound proton tunnels through the nuclear potential barrier, with a rate determined by its energy relative to the barrier height and other factors such as its angular momentum and nuclear deformation, leaving a daughter nucleus which will decay towards stability by β^+ decay (or sometimes α decay). For proton decay to occur, a nucleus must be sufficiently proton-unbound for the decay to be competitive; this is why one must often go several isotopes beyond the proton drip-line to reach a proton emitter, as a small proton decay Q-value can give a proton tunneling rate many orders of magnitude slower than β decay. If the decay energy is too large however, then the decay may occur on a timescale too fast for experimental measurement, which is currently limited to times greater than $\sim 1\mu$s (by recoil separator flight time for fusion-evaporation reactions, and by the implantation recovery time of the detector for fragmentation reactions).

2.1 Energetics

Proton decay can occur when the emission of a proton results in the nucleus increasing its binding energy. The binding energy of a nucleus is the energy required to break it up into its constituent protons and neutrons; therefore increasing the binding energy means the nucleus is more stable. In terms of a decay Q-value, this can be expressed as:

$$Q_p = (M_{Z+1} - M_Z - m_H)c^2 > 0 \tag{2.1}$$

where M_{Z+1} and M_Z are the atomic masses of the parent and daughter nuclei and m_H is the atomic mass of hydrogen. Expressing the Q-value in terms of binding energy rather than mass gives:

$$Q_p = B_Z - B_{Z+1} > 0 \tag{2.2}$$

where the binding energy is given by $B_Z = (ZM_H + NM_n - M_{Z,N})c^2$. The principle of conservation of momentum means that the kinetic energy of the decay is not given solely to the emitted proton but must be shared with the recoiling daughter nucleus. Although the much smaller mass of the proton compared to the nucleus means that the vast majority of the decay energy is carried away by the proton, the recoil is not insignificant and must be corrected for when calculating a Q-value from a measured proton energy.

$$E_p = \frac{M_Z}{M_Z + m_p} Q_p \tag{2.3}$$

Another correction which must be considered is the energy loss of the emitted proton when passing through the cloud of electrons surrounding the

daughter nucleus. This energy, on the order of about 10keV, is equivalent to the difference in atomic binding energies of the parent and daughter atoms, and can be obtained from the work of Huang and Mark [Hua76]. Taking into account this electron screening correction E_{sc} gives the following formula for the proton decay Q-value needed for barrier penetration calculations:

$$Q_{p,nuc} = Q_p + E_{sc} = \frac{E_p(M_Z + m_p)}{M_Z} + E_{sc} \tag{2.4}$$

2.2 Spherical Proton Emitters

There have been many different approaches to the theoretical treatment of proton emission over the last two decades. At a fundamental level, proton emission can be treated in a similar way to the α-decay process, but with the inclusion of a spin-orbit term since the smaller particle has non-zero spin. The most basic theoretical explanations begin with the assumption that the proton occupies a single-particle orbit defined by the spherical shell model.

2.2.1 Spherical shell model

The nuclear shell model, based on a similar theory for atomic electron shells, was successfully used to explain the existence of apparent 'magic numbers' in nuclei. Experimental evidence such as nucleon separation energies demonstrated that nuclei with specific numbers of proton or neutrons (such as 2, 8, 20, 50 and 82) had special properties. Such apparent discontinuities in quantities related to atomic electrons had been explained by considering the particles as building up in shells filled according to the Pauli Exclusion Principle, with 'magic' numbers of particles explained by large energy

gaps between shells, and so a similar technique was applied to the nuclear problem.

In the shell model, one assumes that each nucleon moves in a spherically symmetric potential which is generated by the interactions of all the other nucleons with each other. Once defined, this average potential can then be used to find the nucleon energy levels by solving the time-independent Schrödinger equation:

$$\left(-\frac{\hbar^2}{2m}\nabla^2 + V(r)\right)\psi_i(r) = \epsilon_i\psi_i(r) \tag{2.5}$$

It is still an open problem to derive the nuclear mean field from a microscopic approach, starting from the bare interaction between nucleons, so phenomenological shapes have to be adopted. The potential can be simulated in a variety of ways: for example, the Hartree-Fock method produces an average potential by summing two-body interactions, but is very complex. A simpler but still effective technique is to use a one-body potential estimated from basic nuclear properties, such as the Woods-Saxon potential [Woo54] which imitates the mass distribution in the nucleus:

$$V_{WS}(r) = -V_0\left[1 + exp\left(\frac{r - R_0}{a}\right)\right]^{-1} \tag{2.6}$$

where R_0 is the mean nuclear radius (often given by $R_0 = R_N A^{1/3}$, with R_N a constant of roughly 1.2fm) and a determines the surface diffuseness. The Woods-Saxon potential is considered to be a good approximation to the real nuclear potential, certainly much better than other simplistic potentials such as the finite square well and harmonic oscillator. A nucleon close to the nuclear centre experiences no force, while a nucleon at the surface expe-

riences a strong attractive force, and beyond the surface the potential drops quickly to zero, which agrees with the well-known short range nature of the nuclear force.

The energy levels calculated using the Woods-Saxon potential are shown on the left-hand side of Figure 2.1. Only the first three magic numbers are successfully simulated by this simplistic method. However, the addition of a spin-orbit term to the interaction breaks the orbital angular momentum degeneracies of the states, splitting each l level into two separate levels defined by $j = l \pm 1/2$ (for $l > 0$), each with degeneracy $2j + 1$. As shown on the right-hand side of Figure 2.1, the addition of the spin-orbit term to the Woods-Saxon potential successfully reproduces the observed magic numbers and therefore shell closures [May49, Hax49]. The Fermi level for a shell model nucleus can be calculated simply by filling the single-particle states of increasing energy in accordance with the Pauli Exclusion Principle. For a nucleus with an odd number of protons and an even number of neutrons, the angular momentum of the whole nucleus is given by that of the outermost unpaired proton.

The spherical shell model is quite successful for predicting the properties of nuclei near shell closures, but nuclides far from shell closures can have significant quadrupole deformation and the spherical shell model is insufficient to describe these more exotic creatures (see section 2.3.1).

2.2.2 Semi-classical interpretation of proton decay rates

As mentioned previously, proton decay can be treated in a similar way to α decay, with a particle tunneling through a potential barrier composed of

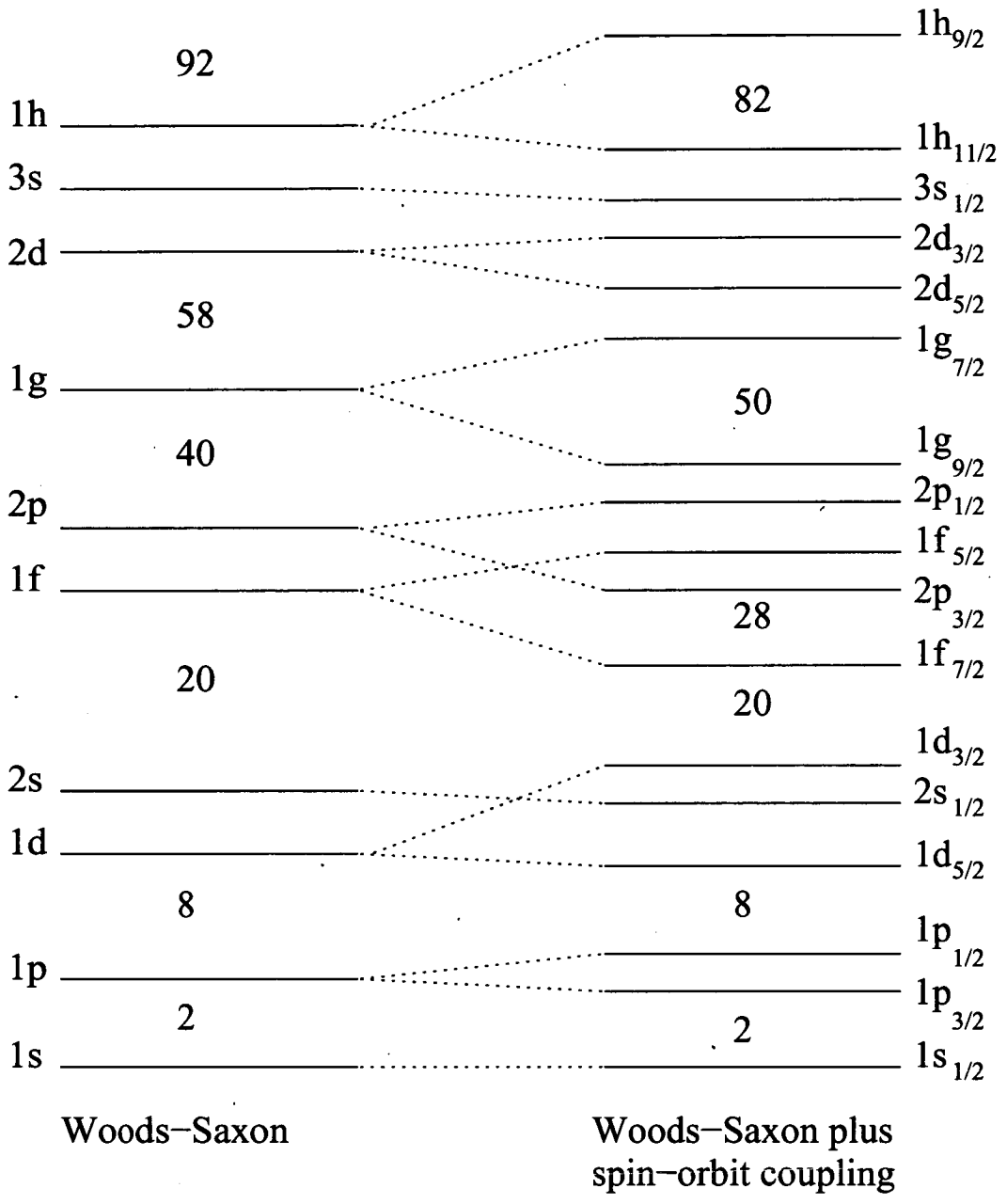

Figure 2.1: *The energy level scheme obtained by using a Woods-Saxon potential and Woods-Saxon potential with a spin-orbit term. The magic number shell closures are shown.*

the sum of a central nuclear potential V_{nuc}, a Coulomb term V_C which is proportional to the charge of the particle, and a centrifugal term V_l which is proportional to $l(l+1)/m$. Since the proton is both lighter and has a lower Z than an α particle, it experiences a larger centrifugal barrier and a smaller Coulomb barrier than the α particle. The combined Coulomb and centrifugal potentials give rise to barriers as large as ~15MeV, compared to the ~1MeV proton energy. The proton is also a fermion with a spin of 1/2, and so a spin-orbit potential term V_{SO} must also be included (this is not necessary for the α particle, which has zero spin). A commonly used approximation for V_{nuc} is the real part of the optical Becchetti-Greenlees potential [Bec69], which was constructed from proton elastic scattering data. The total potential is therefore given by:

$$V(r) = V_{nuc}(r) + V_C(r) + V_l(r) + V_{SO}(r) \tag{2.7}$$

The first attempts to describe proton decay rates used the one dimensional semi-classical WKB barrier approximation, based on the early α-decay theory of Gamow [Gam28], with a decay constant λ given by the product of a factor describing the frequency of tunneling 'attempts' and a transmission coefficient T, with λ of course equivalent to $ln2/t_{1/2}$. Hofmann [Hof89] gives the following expression for the frequency factor:

$$\nu = \frac{\sqrt{2}\pi^2\hbar^3}{\mu^{3/2}R_C^3(zZe^2/R_C - Q_{p,nuc})^{1/2}} \tag{2.8}$$

where μ is the reduced mass of the system, R_C is the Coulomb radius ($R_C = 1.21A^{1/3}$ in fm), z is the charge of the proton (i.e. 1) and Z is the charge of the daughter nucleus.

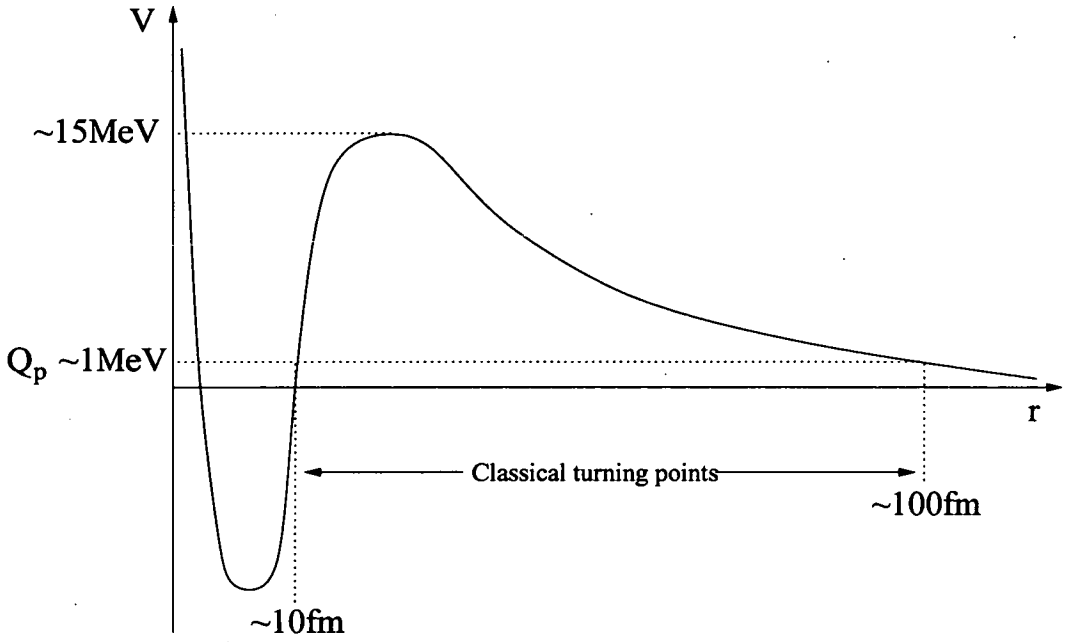

Figure 2.2: *The proton-nucleus potential.*

The WKB (Wentzel, Kramers, Brillouin) approximation, which is based on the assumption that the potential varies slowly relative to the proton wavefunction, is then used to define the transmission coefficient T as $e^{-2G_{jl}}$, where the Gamow factor G_{jl} is proportional to the integral of the potential over the classically forbidden region:

$$G = \sqrt{\frac{2\mu}{\hbar^2}} \int_{r_1}^{r_2} \sqrt{(V(r) - Q_{p,nuc})} dr \tag{2.9}$$

where r_1 and r_2 are the classical turning points as shown in Figure 2.2.

The transmission factor T therefore has an exponential dependence on the proton decay Q-value Q_p (leading to the half-life being proportional to $e^{a/\sqrt{Q_p}}$ with a a constant), meaning that the decay rate can vary over many orders of magnitude with just a very small change in Q_p. The centrifugal part

of the potential barrier varies significantly depending on the orbital angular momentum l_p carried away by the proton, and this variation also affects the transmission factor. The proton partial half-life is therefore extremely sensitive to both the decay energy Q_p and the orbital angular momentum of the proton l_p, and this angular momentum dependence can often be used to identify the spin of the proton state by comparing the experimentally measured half-life with the half-lives calculated for the various possible l orbitals the proton could occupy using the observed decay energy. The proton decay branch will compete with β decay (or even α decay), so that the experimentally measured half-life is a combination of the partial half-lives for the different branches; ideally, the branching fraction can be quantified by observing the competing decay modes, but in reality it is usually more practical to estimate the partial half-life for β^+/EC decay from calculations. The β partial half-life is usually on the order of hundreds of milliseconds, so that if the proton decay occurs on a timescale of a millisecond or less one can consider the state to decay by proton emission 100% of the time. Given the calculation of proton partial half-life as a function of Q_p, one can define a Q-value window representing the range of energies for which the proton decay has an experimentally observable half-life. Decays faster than 1μs are impossible to detect with current mass separation methods, and decays slower than about 1s are unlikely to compete effectively with β decay. This time window of 1μs-1s results in a small observable Q-value window around 1MeV.

The semi-classical method was used to analyse the results of proton decay experiments for many years, and was sufficient in most cases to make an unambiguous qualitative assignment of the proton orbital angular mo-

mentum and therefore the parent state. Indeed, for some spherical proton emitters, it has been shown [Åbe97] that the WKB approach gives half-lives within 10% of the more sophisticated methods described in the next section.

2.2.3 Modern proton decay theory

The flourishing of the experimental study of proton emission over the last two decades has led to a concerted effort to produce quantitative theoretical explanations for the process of proton decay, which can then be compared with nuclear structure models. The simple semi-classical method, utilising the WKB approximation, is not sufficient to describe the subtleties of proton emission and several new theories have been developed in recent years. All these theories consider proton emitters as extremely narrow resonances which can be thought of as quasi-stationary states. The resonance width Γ relates to the proton partial half-life by $t_{1/2,p} = \hbar/\Gamma ln2$. The theoretical description of these states is a challenging task due to the dramatically different energy scales for the resonance energy ($\sim$1MeV) and width (from $\sim 10^{-16}$ to $\sim 10^{-22}$MeV). The two main theoretical approaches are the 'direct' and 'distorted wave' methods.

In both approaches, one considers the parent nucleus as the unbound proton moving in the potential of the daughter and solves the Schrödinger equation accordingly to find the proton single-particle wave function, with the nuclear potential depth adjusted to reproduce the experimental proton decay Q-value. In reality, the process of proton emission is more complicated since the perfect separation of the nuclear many-body wave function into that of the proton and daughter cannot truly be made. However, this

approximation has proved sufficient to describe the properties of these resonances, as we shall see. In the 'direct' approach of Maglione and Ferreira [Mag98], the single particle wave function is defined to be a Coulomb wave at large distances from the nucleus, beyond the range of the nuclear force. The radial part of the wave function, $\psi_{lj}(r) = u_{lj}(r)/r$, is matched to this outgoing wave $\psi_{lj}^{out}(r)$, thus imposing the decay on the quasistationary state.

$$u_{lj}(r) = r\psi_{lj}^{out}(r) = N_{lj}^{dir}[G_l(kr) + iF_l(kr)] \tag{2.10}$$

where F_l and G_l are the regular and irregular Coulomb functions, k is the wave number $\sqrt{2\mu E}/\hbar$ and N_{lj}^{dir} is a normalisation constant, or matching amplitude. The decay width is found directly from the matching amplitudes by calculating the radial probability flux F_{lj} through a sphere.

$$F_{lj} = \int_0^{2\pi}\int_0^{2\pi} |u_{lj}(r)|^2 \nu r^2 sin\theta d\theta d\phi \tag{2.11}$$

$$\lim_{r\to\infty} |u_{lj}(r)|^2 = |N_{lj}^{dir}|^2 \tag{2.12}$$

where ν is $\hbar k/\mu$, the particle velocity (μ being the reduced mass of the system). This flux is equivalent to the inverse of the mean lifetime. The matching amplitude N can then be determined at a specific radius R inside the classical external turning point, because the wave function decreases very rapidly outside the nucleus (typically by 10 orders of magnitude). A matching radius of ~25fm is thought to be adequate for the known spherical proton emitters [Dav00a], whereas the classical external turning point is usually in the region 80-100fm. The 'direct' method decay width is therefore given by:

$$\Gamma_{lj}^{dir}(R) = \frac{\hbar^2 k}{\mu}\left(\frac{u_{lj}(R)}{G_l(R) + iF_l(R)}\right)^2 \tag{2.13}$$

which is effectively independent of R for distances beyond the range of the nuclear potential. Because the imaginary part of the resonance energy (i.e. the decay width) is so much smaller than the real part, it is usual to neglect the imaginary term in the denominator.

The 'distorted wave' approach, first formulated by Bugrov et al [Bug85], is based on the Gell-Mann-Goldberger transformation and makes use of the Coulomb wave functions determined by the pointlike Coulomb interaction. We consider the resonance width as:

$$\Gamma^{DW} = 2\pi |T_{A+1,Z+1:A,Z}|^2 \tag{2.14}$$

where the transition amplitude $T_{A+1,Z+1:A,Z}$, the overlap of the parent and daughter states, is calculated using the distorted-wave Born approximation (DWBA):

$$T_{A+1,Z+1:A,Z} = < \psi_{Ap}\Psi_{Ap}|V_{Ap}|\Psi_{A+1} > \tag{2.15}$$

where ψ_{Ap} is the outgoing spherical wave representing the relative motion of the proton with respect to the daughter, Ψ_{Ap} is the product of the intrinsic wavefunctions of the proton and daughter, Ψ_{A+1} is the metastable state of the parent nucleus (i.e. the initial state) and V_{Ap} is the interaction between proton and daughter. As before, V_{Ap} should strictly be the sum of two-body interactions between the emitted proton and each of the other nucleons in the daughter, but it can be approximated by a sum of a simple optical

nuclear potential and the Coulomb potential. The daughter nucleus is again treated as an inert core.

The Gell-Mann Goldberger transformation [Fes92] can be used to rewrite the transition amplitude term as:

$$T_{A+1,Z+1:A,Z} =< \Psi_{Ap}\psi^{C}_{Ap}|V - V^{0}_{C}|\Psi_{A+1} > \tag{2.16}$$

where ψ^{C}_{Ap} is the scattering wavefunction associated with the point charge Coulomb potential V^{0}_{C}. The key point in this formalism is the difference between the Coulomb potential from the finite charge distribution V_C and that of the point charge V^{0}_{C}, which leads to the distortion of the outgoing wave. The radial component of ψ^{C}_{Ap} is:

$$\psi_l(r) = \sqrt{\frac{2\mu}{\pi\hbar^2 k}}\frac{F_l(kr)}{r} \tag{2.17}$$

where k is the wave number and F_l is the regular Coulomb function. The initial state wave function Ψ_{A+1} can be expressed as the product of the daughter nucleus wave function and the proton wave function. The radial wavefunction $u_{lj}(r)$ of the quasibound proton can be found by matching it smoothly to an irregular Coulomb function $G_l(kr)$ that asymptotically describes the proton at large distances from the nucleus, in a similar manner to the 'direct' approach. This method ultimately provides the following expression for the resonance width:

$$\Gamma = \frac{4\mu}{\hbar^2 k}\left|\int_0^\infty F_l(kr)[V_N(r) - V^{0}_{C}(r)]u_{lj}(r)dr\right|^2 \tag{2.18}$$

The nuclear interaction V_N contains the spin-orbit term. It has been

shown [Dav00b] that the 'direct' and 'distorted wave' methods are effectively equivalent for spherical proton emitters.

2.3 Deformed Proton Emitters

Nuclei far from closed shells often have large quadrupole deformations, giving them prolate or oblate spheroidal shapes. For such nuclei a spherical potential cannot be used to calculate their properties, and different approaches must be pursued. Many measured proton emitters are predicted by mass models (see section 2.5 and [Mol95]) to have significant prolate deformations ($\beta_2 \sim 0.3$), and the failure of spherical proton emission theory to explain their decay rates is clear evidence of that deformation.

2.3.1 Nilsson model

In the early 1950s, it was observed that some nuclei far from closed shells exhibited quadrupole moments many times larger than could be accounted for by a single particle. Rainwater [Rai50] suggested that the single particle deforms the whole nucleus, and that the observed quadrupole moment results from the collective deformation of many orbits. This concept was developed mathematically by Bohr and Mottelson into the 'collective' model of the nucleus. A microscopic approach to deformed nuclei was formulated by Nilsson [Nil55], who used the shell model with a deformed harmonic oscillator potential approximating the nuclear shape (although a Woods-Saxon potential can also be used). The energy levels are given by eigenvalues of the following Hamiltonian:

$$H = -\frac{\hbar^2}{2m}\nabla^2 + \frac{1}{2}m\omega_0^2 r^2 - \frac{4}{3}\sqrt{\frac{\pi}{5}}\delta m\omega_0^2 r^2 Y_{20} + C\underline{l}.\underline{s} + Dl^2 \qquad (2.19)$$

where ω_0 is the oscillator frequency (with $\hbar\omega_0 = 41A^{-1/3}$), C and D are Clebsh-Gordan and D-matrix coefficients and Y_{20} is the spherical harmonic oscillator. δ is the deformation parameter $\Delta R/R_{rms}$, where R_{rms} is the root mean square nuclear radius and ΔR is the difference between the semi-major and semi-minor axes of the ellipsoid. This quantity relates to other deformation parameters, including the commonly-used β_2, as follows:

$\epsilon_2 = \delta + \frac{1}{6}\delta^2 + \frac{5}{18}\delta^3 + \frac{37}{216}\delta^4 + ...$

$\beta_2 = \sqrt{\frac{\pi}{5}}(\frac{4}{3}\epsilon_2 + \frac{4}{9}\epsilon_2^2 + \frac{4}{27}\epsilon_2^3 + ...) \sim 1.057\delta$

The deformed potential breaks the $2j + 1$ degeneracy of the spherical shell model orbitals, creating $j + 1/2$ sub-shells with a degeneracy of two. For these states, l and j cease to be good quantum numbers, and they can instead be defined by Ω, the projection of j on the ellipsoid symmetry axis, and of course the parity. With the approximation of an infinite deformation, the nucleon wavefunction can also be identified by three asymptotic quantum numbers: the total oscillator shell number N, the number of nodes in the z direction n_z and the projection of l on the symmetry axis Λ. A Nilsson level is therefore usually described in the form $\Omega^\pi[Nn_z\Lambda]$. The Nilsson shell model (see figure 2.3) fills up in the same manner as its spherical counterpart, starting from the lowest energy and building up to find the likely states of the Fermi level nucleons, and the ground state nuclear deformation can be found by minimising the sum of the single particle energies with respect to the deformation. The energy levels can be thought of as depending on

the spatial orientation of the single particle orbital relative to the deformed core i.e. the component of j along the symmetry axis. For nuclei with prolate deformation, orbits with smaller Ω interact more strongly with the core, are more tightly bound and therefore lower in energy than orbits with relatively higher Ω, and vice versa for nuclei with oblate deformation (where orbits with large Ω involve motion localised near the equatorial plane). The Nilsson wavefunctions do not possess a fixed angular momentum J - rather, it can be projected onto rotational states of many different angular momenta R. Therefore a particle with j in a Nilsson orbit gives rise to a rotational band rather than a single state, with $J = j + R$ (j precessing around the symmetry axis).

2.3.2 Proton emission from deformed nuclei

Deformed proton emitters, as in the case of their spherical equivalents, can be treated as narrow resonances of the odd proton moving in a single-particle Nilsson level of a deformed potential, with 'direct' and 'distorted wave' treatments to calculate the resonance widths and thus the decay rates.

The single-particle Nilsson wave function of the unbound proton can be expanded into spherical components, where the coefficients of this expansion can be understood as the amounts of the various spherical single-particle states present in the wave function. It is assumed that the daughter deformation is identical to that of the parent nucleus. For the decay to the ground state of an even-even daughter, angular momentum conservation implies that the outgoing proton has $j_p = J_i = K_i$, the projection of the quasibound proton's angular momentum on the core symmetry axis.

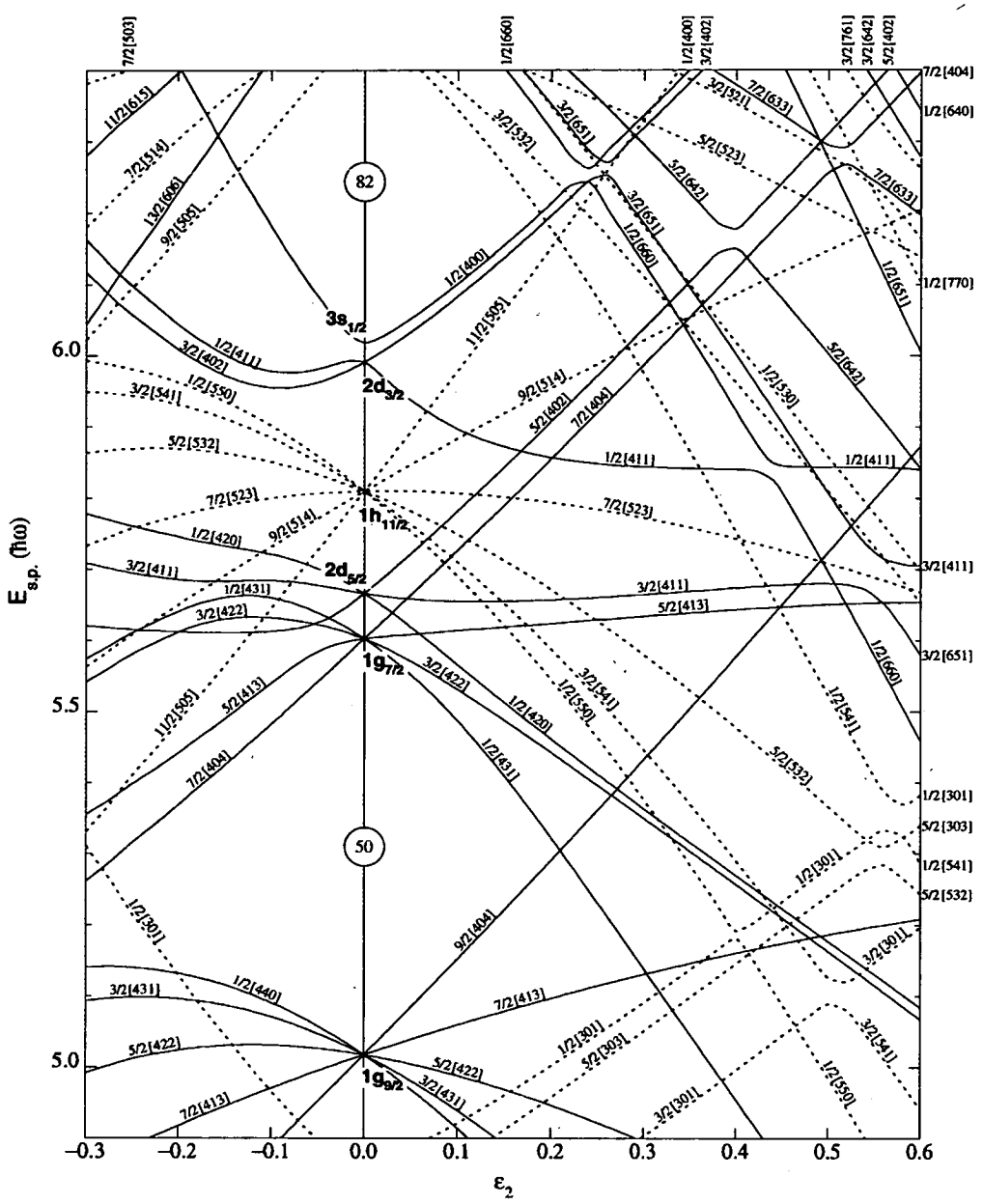

Figure 2.3: *Nilsson level diagram for protons (50<Z<82) as a function of deformation parameter ϵ_2, with $\epsilon_4 = \epsilon_2^2/6$, calculated as described by Bengtsson and Ragnarsson [Ben85].*

The range of the Coulomb quadrupole interaction is large, which complicates the direct method, which relies on the Coulomb potential being spherically symmetric. It has been shown [Dav00a] that the half-life results of the direct and distorted wave methods for deformed proton emitters in the adiabatic limit only agree to within 20%, whereas they gave identical results for spherical emitters. These methods which had been successful for spherical proton emitters proved somewhat innacurate in deformed cases, so more advanced models were developed. The coupled channels Green's function method was used to calculate proton decay rates in this work.

In the coupled channels approach [Esb00], we consider an unbound proton interacting with the axially symmetric, quadrupole deformed core (the daughter nucleus) which may have non-zero excitation energy (the so-called 'particle-rotor' model). The coupled equations are solved for real energies using the Green's function method [Bug89], and it has been shown [Esb00] that the decay rate results produced by this method compare favourably with those obtained by the 'direct' method [Mag98].

In the laboratory frame, for a total spin I of the decaying state, the decay channels are labelled by the quantum numbers (ljR) where l and j specify the single particle orbits and R is the angular momentum of the rotating core. We consider only the ground state rotational band of the rotor, with energy $E_R = (\hbar^2/2J_0)R(R+1)$ where J_0 is the moment of inertia and $R = 0, 2, 4..$ etc.

The total wavefunction is:

$$\Psi_{IM}(\underline{\mathbf{r}}, \omega) = \sum_{ljR} \frac{\psi^I_{ljR}}{r} |l(jR)IM\rangle \tag{2.20}$$

where

$$|l(jR)IM\rangle = \sum_{mM_R} \langle jmRM_R|IM\rangle |RM_R\rangle |ljm\rangle \tag{2.21}$$

is the channel-spin wavefunction, obtained by coupling the single particle wavefunction $|ljm\rangle$ to that of the rotor $|RM_R\rangle$, where M is the projection of the total spin I on the laboratory axis.

The Hamiltonian of the proton-core system is:

$$H = T + V(\underline{\mathbf{r}}, \omega) + V_{ls}(r) + H_R \tag{2.22}$$

where T is the kinetic energy of the proton relative to the core, $V(\underline{\mathbf{r}}, \omega)$ is the Coulomb plus nuclear interaction (a function of proton position $\underline{\mathbf{r}}$ and the rotor orientation ω), $V_{ls}(r)$ is the spin-orbit interaction and H_R is the Hamiltonian of the rotor.

The Coulomb plus nuclear interaction is expanded in multipoles:

$$V(r, \omega) = \sum_{\lambda} V_\lambda(r) P_\lambda[cos(\theta')] \tag{2.23}$$

where θ' is the orientation of the proton with respect to the symmetry axis of the rotor. Using the wavefunction from equation 2.20 in the Schrödinger equation results in the set of coupled differential equations for the radial wavefunctions:

$$\begin{aligned}(h_{lj} + E_R - E)\psi^I_{ljR}(r) = &- \sum_{l'j'R'} \sum_{\lambda \neq 0} \langle l(jR)IM|P_\lambda[cos(\theta')]| \\ &\times |l'(j'R')IM\rangle V_\lambda(r)\psi^I_{l'j'R'}(r)\end{aligned} \tag{2.24}$$

where h_{lj} includes the monopole terms of the interaction:

$$h_{lj} = \frac{\hbar^2}{2\mu}\left(-\frac{d^2}{dr^2} + \frac{l(l+1)}{r^2}\right) + V_0(r) + V_{ls}(r) \tag{2.25}$$

The deformed spin-orbit interaction can be written as [She69]:

$$V_{ls}(r,\theta) = 4V_{SO}([\nabla f(r,\theta)] \times \underline{\mathbf{p}}).\underline{\mathbf{s}} \tag{2.26}$$

where θ is the angle between $\underline{\mathbf{r}}$ and the symmetry axis of the rotor, $\underline{\mathbf{p}}$ is the momentum and $f(r,\theta)$ is the Fermi function. Using the multipole expansion $f(r,\theta) = \Sigma_\lambda f_\lambda(r) P_\lambda[cos(\theta)]$, we can derive the expression:

$$\begin{aligned} V_{ls}(r,\theta) =& 4V_{SO}\sum_\lambda \left(\frac{1}{r}\frac{df_\lambda}{dr}P_\lambda \underline{\mathbf{l}}.\underline{\mathbf{s}} - \frac{f_\lambda}{r}[\underline{\mathbf{l}}.\underline{\mathbf{s}}, P_\lambda]\frac{d}{dr}\right. \\ & \left. - \frac{f_\lambda}{r^2}\frac{dP_\lambda}{d\,cos(\theta)}\frac{\underline{\mathbf{r}}.\underline{\mathbf{s}}}{r} l_z\right) \end{aligned} \tag{2.27}$$

Further details on these potentials can be found in [Esb00].

Using the solutions to the coupled equations, the decay width can then be calculated using the 'direct' and distorted wave methods described previously. In this work, the solutions are matched to Coulomb waves at a relatively small distance (roughly 15-20fm) which is outside the range of nuclear couplings, and real energies (i.e. stationary states) are used. The decay properties of the standing wave are extracted by applying the outgoing distorted wave Green's function method (see [Esb00] for full details), which includes the effect of long-range Coulomb couplings (out to a radius of about 100fm, near the outer classical turning point) in the calculation.

The calculations in this work were performed in the adiabatic limit (i.e. assuming the rotor has infinite moment of inertia and therefore collapsing the rotational band to zero energy, making the reference frame of the rotor equivalent to the laboratory frame) and used the K representation rather than the R representation described above. We consider the system in the body-fixed frame of the rotor rather than the laboratory frame, with the available decay channels labelled (ljK) where K is the projection of the total spin I on the symmetry axis. Transformation can be made between the R and K bases as follows [Esb00]:

$$\psi_{lj}^{IK}(r) = \sum_{R} A_{jR}^{IK} \psi_{ljR}^{I}(r) \quad \textbf{and} \quad \psi_{ljR}^{I}(r) = \sum_{K>0} A_{jR}^{IK} \psi_{lj}^{IK}(r) \tag{2.28}$$

where

$$A_{jR}^{IK} = \sqrt{\frac{2R+1}{2I+1}} \langle jKR0|IK\rangle \sqrt{1+(-1)^R} \tag{2.29}$$

assuming even R, which is valid for the ground state rotational band. The coupled equations (c.f. equation 2.24) are obtained in the K representation by using the above relations and summing over R:

$$\begin{aligned} &(h_{lj} - E)\psi_{lj}^{IK}(r) + \sum_{K'>0} W_{KK'}^{jI} \psi_{lj}^{IK'}(r) = \\ &- \sum_{l'j'} \sum_{\lambda>0} \langle ljK|P_\lambda|l'j'K\rangle_0 V_\lambda(r) \psi_{l'j'}^{IK}(r) \end{aligned} \tag{2.30}$$

where

$$W^{jI}_{KK'} = \sum_R A^{IK}_{jR} E_R A^{IK'}_{jR} \tag{2.31}$$

This coupling matrix contains off-diagonal terms due to Coriolis mixing between neighbouring K values (i.e. $K' = K + 1$). The adiabatic limit in the K representation eliminates these off-diagonal terms and therefore simplifies the calculation by reducing the number of coupled channels (the number being equal to the number of single particle orbits that one includes, with the restriction $j \geq K$). The adiabatic limit is equivalent to assuming that the Coriolis and centrifugal perturbations to the structure are negligible.

Calculations using the distorted wave Green's function method in the adiabatic limit are expected to give a more realistic estimate of the decay width than the full coupled channel approach for states with relatively high spin (such as the $7/2^-$ ground state of ^{141}Ho) due to the greater Coriolis mixing effects involved (compared to lower spin states).

2.3.3 Fine structure in proton decay

A predicted consequence of large prolate deformation in an even-even nucleus is the lowering of the energy of the first excited 2^+ rotational state. In terms of proton emission, this can result in a significant branching of the proton decay of an odd-even nucleus to the first excited state of the daughter by increasing the decay energy available to this branch. This effect is known as fine structure, and has been observed in the proton decay of the deformed odd-even nuclides ^{131}Eu [Son99] and ^{145}Tm [Kar03]. Other predicted lanthanide proton emitters such as ^{135}Tb and ^{125}Pm were also considered likely

to exhibit this phenomenon. Fine structure has also been observed in the proton decay of odd-odd ^{146}Tm [Gin03], although this example is complicated by the even-odd nature of the daughter which leads to a complex decay scheme with at least five separate transitions. After the proton decay to the excited state of the daughter, this state quickly decays to the ground state by γ decay or internal conversion. The internal conversion coefficient (the probability of electron emission relative to γ emission) is roughly independent of nuclear structure details, and is found to increase as Z^3, decrease rapidly with transition energy E, increase rapidly with multipole order L, and decrease as $1/n^3$ where n is the atomic electron shell number, which causes the internal conversion process to be dominated by K-shell emission. The electrons in the K shell are much more tightly bound than their counterparts in the higher shells, which means that their measured energy will be reduced significantly from the energy of the daughter excited state by an amount equal to the K-shell binding energy. Detailed computations of internal conversion coefficients, using the proper atomic wave functions, are tabulated in various works (for example, in the Table of Isotopes [Fir95]).

In deformed nuclei, the wave function of the decaying state is a mixture of several spherical j_p components. In the adiabatic limit, only the angular momentum projection on the symmetry axis is a good quantum number (along with parity). Only the spherical single particle component with the lowest angular momentum (bearing in mind conservation of angular momentum and parity) effectively contributes to the decay, and it is usually a relatively small component of the total wavefunction. The decay width is proportional to the square of the amplitude of this component in the initial wavefunction.

The Coriolis coupling can admix states with smaller l values, and therefore lower centrifugal barriers, into the proton wave function. Low-l components, however small, can substantially affect the lifetime. Coupling to the 2^+ state allows proton single-particle states with lower j_p to contribute to the decay, which compensates for the lower decay energy by lowering the effective centrifugal barrier.

The energy of the excited state of the daughter is included directly in the adiabatic limit by the distorted wave Green's function method described previously, by using the correct 'asymptotic momentum' $\hbar k_R$ in the distorted Coulomb wavefunctions and matching amplitude, where $k_R = \sqrt{2\mu(E_{res} - E_R)}$ (E_{res} being the proton resonance energy and E_R the rotational energy of the excited core).

2.4 Spectroscopic Factors

The simplistic view of the proton emitter as an inert core coupled to a proton in a well-defined single-particle orbital with a particular angular momentum is not satisfactory for a complete description of the proton decay process. This model may be sufficient for an order-of-magnitude calculation, which may be enough to determine the proton orbital, but for a more accurate and sophisticated picture, nuclear structure effects must be taken into account. The proton decay can be significantly hindered, and therefore the half-life increased, by the incomplete overlap of the parent and daughter nuclear wavefunctions; for example if a hole in an orbital in the parent nucleus is filled in the daughter. This overlap hindrance effect is described by the spectroscopic factor S_j.

The experimental spectroscopic factor is defined as the ratio of the theoretically estimated half-life to the actual measured half-life:

$$S_j^{exp} = \frac{t_{1/2}^{th}}{t_{1/2}^{exp}} \tag{2.32}$$

Incomplete wavefunction overlap will lead to the experimental half-life being longer than the theoretical prediction, and therefore the spectroscopic factor will be less than one.

The theoretical spectroscopic factor is a measure of the likelihood that one nucleon (or hole) position will differ from the initial (parent) to the final (daughter) nuclear state:

$$S_j^{th} = \left| < \psi_{J_i}(Z+1, A+1) || a_{nlj}^{+} || \psi_{J_f}(Z, A) > \right|^2 \tag{2.33}$$

where ψ_{J_i} and ψ_{J_f} are the initial and final states and a_{nlj}^{+} is the creation operator relating to the single particle orbital (nlj), defining the angular momentum carried away by the proton. This is analogous to the calculation used to describe the hindrance in proton pick-up reactions [Boh69].

The theoretical spectroscopic factor can be calculated in several different ways. Davids *et al* [Dav97] estimated the spectroscopic factors of the proton emitters in the region $65 \leq Z \leq 82$ using a low-seniority shell model calculation, which characterises the configurations of n particles in i orbitals by the number of particles combined in 0^+ pairs. The seniority quantum number denotes the number of unpaired particles in the model space. This model considered 18 particles in the $s_{1/2}$, $d_{3/2}$ and $h_{11/2}$ spherical proton orbitals above the Z=64 sub-shell closure, with neutrons assumed to be spectators (so that their configuration is not altered by the proton de-

cay process). A proton pairing interaction was used, and the three orbitals were assumed to have the same energy. The final result, after considering the overlap between parent and daughter wavefunctions and evaluating the reduced matrix element for the case of a full set of particles, was shown to be:

$$S^{th}(p) = \frac{p}{9} \tag{2.34}$$

where p is the number of proton hole pairs counting down from Z=82 in the daughter nucleus. This simple expression was found to model the decreasing spectroscopic factors of the string of known proton emitters from Z=69 to Z=81 with reasonable accuracy, apart from the cases of proton decay from the $d_{3/2}$ orbital.

A more intricate approach, using the independent quasi-particle approximation of BCS theory, is described by Åberg, Semmes and Nazarewicz [Åbe97]. This method considers the proton emitter as an inert core with an odd proton represented by a single quasi-particle state, with the spectroscopic factor given by:

$$S_p^{th} = u_j^2 \tag{2.35}$$

where u_j^2 is the probability that the spherical orbital represented by j is empty in the daughter nucleus (where 1 means completely empty on average and 0 means completely full on average). This quantity is equal to $1 - v_j^2$ where v_j is the occupation probability:

$$v_j^2 = \frac{1}{2}(1 - \frac{\epsilon_j - \lambda}{[(\epsilon_j - \lambda)^2 + \Delta^2]^{1/2}}) \tag{2.36}$$

where λ is the Fermi level energy, Δ is the proton pairing gap energy, ϵ_j is the relevant single-particle level energy (calculated by solving Schrödinger's equation with a suitable potential), and G_p is the proton pairing strength, which is given by:

$$G_p = \frac{1}{A}[19.9 + 0.176(N - Z)] \tag{2.37}$$

Only a few levels below and above the Fermi energy (within a range of Δ) contribute to the configuration mixing caused by pairing correlations.

This method can be used for deformed as well as spherical proton emitters, as long as the single-particle level energies are known accurately, particularly those near the Fermi surface.

2.5 Mass Models

As shown in section 2.2, the decay rate of a proton-emitting nucleus is extremely sensitive to the proton decay Q-value, so in order to tell whether a search experiment for a particular proton decay candidate is feasible it is advantageous to have a rough approximation of these values. One can estimate the one-proton separation energies of extremely neutron-deficient nuclei, and therefore their proton decay Q-values, by utilising the various nuclear mass models which have been formulated over the last few decades. These models, although differing in their approaches, all use sets of adjustable parameters which are modified by fitting to experimental data to explain nuclear structure effects which cannot be interpreted satisfactorily by the simple shell model theory. It is often found that more complex models with a larger number of parameters provide a better fit to data than models

with a smaller parameter set, although this higher level of complexity may not necessarily reflect the accuracy of the model's predictions beyond the known data set. Indeed, models with fewer parameters are thought to give better predictions beyond their known data sets. As well as predicting mass-related properties like the one-proton and one-neutron separation energies, such models also can provide estimates for properties such as deformation and the position of the Fermi level.

2.5.1 Möller-Nix mass model

The macroscopic-microscopic model of Möller et al [Mol95, Mol97] is commonly used to estimate and compare the properties of proton emitters. In this model, the nuclear binding energy and therefore the mass is found by considering the combination of a macroscopic semi-empirical term (which covers familiar mass concepts such as volume and surface energy, Coulomb repulsion of the protons and pairing energy) and a microscopic term which deals with single-particle shell model corrections and pairing energy.

$$E(Z, N, \epsilon) = E_{macro}(Z, N, \epsilon) + E_{micro}(Z, N, \epsilon) \tag{2.38}$$

where ϵ is a deformation parameter, showing the shape-dependence of the model. The macroscopic term is based on the finite range droplet model, a development of the droplet model described by Myers [Mye77], with an extra term to account for the short range of the nuclear force. The microscopic term is found by comparing the single-particle levels of the Nilsson model with those calculated by Strutinsky's method [Str67, Str68] to find the shell correction, and then evaluating the pairing term using the

Lipkin-Nogami version of BCS theory [Pra73].

The ground state nuclear masses are evaluated by minimising the total energy with respect to the deformation parameter, and one-proton separation energies can then be calculated from these values. The model also provides predictions for ground state nuclear deformations, as shown in Figure 2.4 for the region around the proton drip-line from Z=50 to Z=85. These predictions show the expected pattern of significant quadrupole deformation away from shell closures, and this model's estimates of the deformations of proton emitters have been shown to agree well with experimental data. The Möller-Nix model also provides estimates of the spin and parity of odd nucleons, which can be useful in identifying the likely state of the unbound proton in a proton-emitting nucleus, and other useful quantities such as the partial half-life for β decay.

The Möller-Nix model uses 38 parameters, only 16 of which are evaluated by least-squares fitting to measured mass data of 1654 nuclides. The RMS error for the model's mass predictions is estimated to be around 700keV.

2.5.2 Liran-Zeldes mass model

The mass model of Liran and Zeldes [Lir76] has also proven to be quite useful for proton decay studies. This model uses a shell model method with a strong pairing interaction which is complicated by one- and two-nucleon excitations within sub-shells and shells connected to nuclear deformation and core excitation. The nuclear ground state energy can be expressed as:

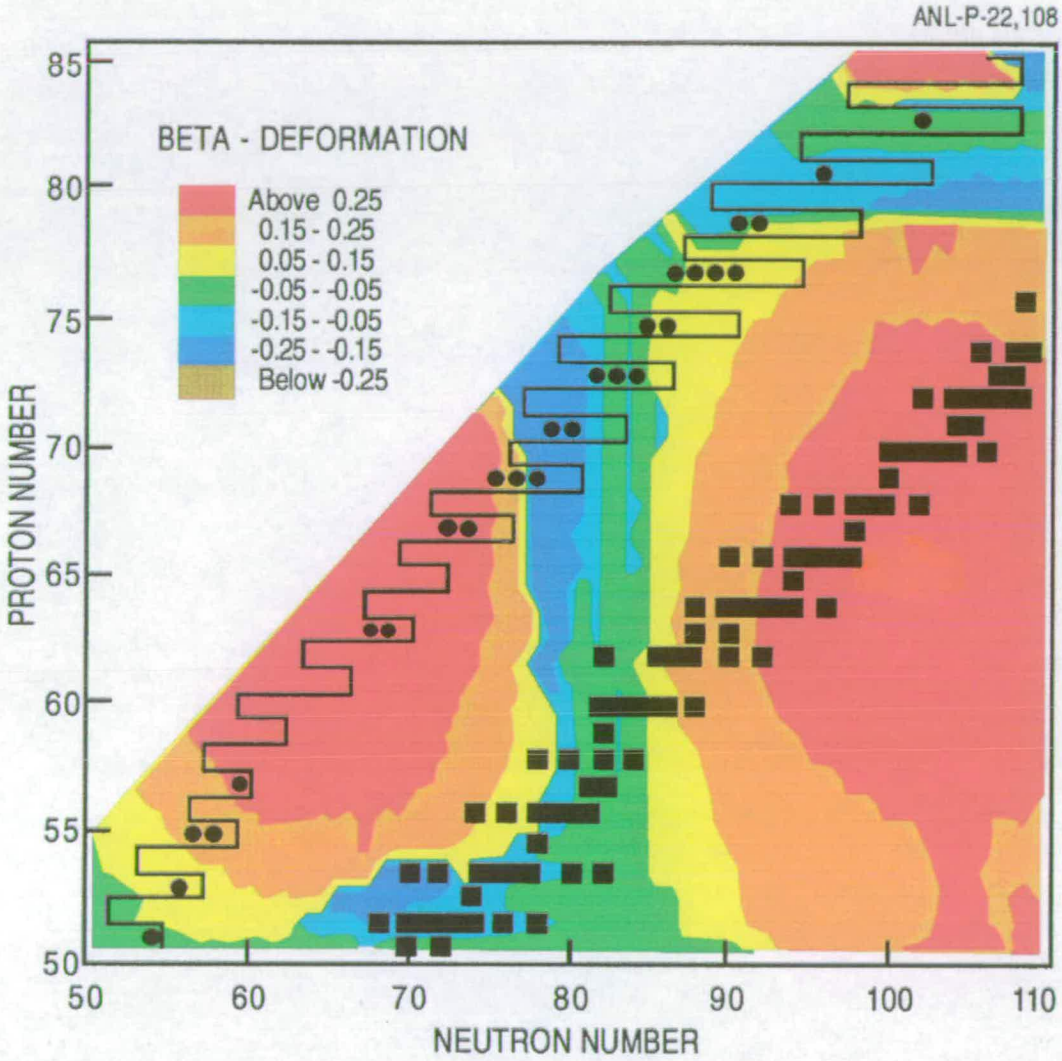

Figure 2.4: *Möller-Nix mass model deformation predictions (squares are stable nuclei, circles are known proton emitters beyond the predicted proton drip line).*

$$E(Z,N) = E_{pair}(Z,N) + E_{def}(Z,N) + E_{coul}(Z,N) \qquad (2.39)$$

where E_{pair} is the pairing energy, E_{def} is the deformation energy associated with configuraton mixing and E_{coul} is the Coulomb energy. The E_{pair} and E_{def} terms are treated differently for regions where the valence nucleons occupy the same major shell and regions where they occupy different shells. The Liran-Zeldes model has 178 independent parameters which are determined by least-squares fitting from the data of 1818 known nuclides, with the requirement that the mass surface must be continuous at the boundaries between the different shell regions. The RMS error in the mass predictions for this model is estimated to be around 500keV.

Chapter 3

Experimental Method

3.1 Introduction

There are many difficulties involved in experiments searching for proton radioactivity; the production of exotic drip-line nuclei in sufficient quantities, the detection of the emitted proton (if the decay mode exists) and the unambiguous identification of the parent nucleus. The first proton-emitting isotopes were identified in the early 1980s using methods as diverse as a velocity filter [Hof82a], on-line mass separation [Kle82] and a catcher foil combined with an ionisation chamber [Fae84]. However, the most productive technique has proved to be the use of a recoil mass spectrometer combined with a double-sided silicon strip detector (DSSD) [Sel92a]. This chapter will describe the apparatus and procedures used to search for new proton-emitting nuclides at Argonne National Laboratory, including the installation of a new DSSD system.

The Argonne Tandem Linear Accelerator System (ATLAS) supplies

a heavy ion beam which impinges on a thin target, producing exotic nuclei by fusion-evaporation reactions, which are then dispersed according to their mass-to-charge (A/Q) ratio by the Fragment Mass Analyser (FMA). At the focal plane of the FMA, a multi-wire proportional counter provides position data, enabling the masses of the recoils to be identified, and energy loss data which allows the recoils to be differentiated from scattered beam particles. The recoils then defocus and implant into a DSSD, illuminating it approximately uniformly. The DSSD described in this thesis is an entirely new design, consisting of 80 orthogonal strips on each side, giving 6400 'quasi-pixels' over an area of 1024mm^2. This area is large enough to cover the full FMA image, as did a previous detector with only 40 strips per face and thus a factor of six fewer quasi-pixels per unit area. The new DSSD retains the fine granularity necessary for accurate correlations possessed by another previous detector, which had 48 strips per face and an area four times smaller.

3.2 Selection of Heavy Ion Beam and Target

The Argonne Tandem Linear Accelerator System [Aro86] was the world's first superconducting linear accelerator for ions when brought on-line in 1985. As the name implies, it initially used a 9MV tandem Van de Graaff ion source to inject the beam into two 20MV linacs, but the facility was upgraded in 1987 to allow the use of an electron cyclotron resonance (ECR) ion source, linked to a 12MV injector linac (the Positive Ion Injector, or PII) [Bol93]. The ions from the ECR+PII system are then injected into the main 20MV linac system, which can accelerate the particles to energies of up to

17MeV/u. The ECR source, which produces positive ions by heating the electrons of a plasma in a magnetic field with a specific microwave frequency, is superior to the electrostatic tandem because it allows a wider variety of beam species (up to uranium, and including noble gases which cannot be produced efficiently as negative ions for a tandem accelerator) and a higher beam current (up to 100 particle-nanoamperes, or pnA, for a ^{58}Ni beam). A second ECR source was completed in 1997, and the original source was upgraded in 2000, which increased the available beam intensity by an order of magnitude. In 2001-2002, the ECR source system underwent another upgrade [Moe02] which increased the available beam intensity by a further factor of two.

All the observed direct proton-emitting nuclides have been produced using fusion-evaporation reactions (with beam energies on the order of 5MeV/u). If proton-rich (but necessarily stable) isotopes are used for the beam and target, then it becomes possible to access the proton drip-line region. The residues from such reactions, where the beam and target nuclei fuse to create a highly-excited compound nucleus which then 'evaporates' off particles to reduce its energy, tend to be less proton-rich than the compound nucleus due to the preferential evaporation of protons caused by the high density of states for protons in this region and high neutron separation energy. This preference towards the compound nucleus moving away from the proton drip-line and towards stability means that a search for proton radioactivity involves probing relatively low cross-section reactions where more neutrons than protons are evaporated. The final choices of the beam and target isotopes are dependent on several factors apart from the desired reaction product, such as the isotopic abundances of the materials and their physical properties.

For example, the nuclide ^{96}Ru is extremely proton-rich but makes up only ~5% of the isotopic abundance of Ruthenium; this may make it desirable to use a specially isotopically-enriched sample rather than a sample with the natural isotopic abundances, although this can often prove very costly. The physical properties of materials come into play with target selection; for example, a ^{40}Ca target must be handled with care as it oxidises easily and may not be able to withstand the heat deposited by an intense incident beam, unlike a ^{92}Mo target which has a much higher melting point. One must also consider the use of inverse kinematics (i.e. where the beam species is heavier than the target), which increases the proportion of residues ejected from the target in the forward direction, and thus increasing the transmission through the FMA, at the cost of increasing the amount of scattered beam particles passing through the FMA.

Once the beam and target nuclides are selected, the beam energy (and intensity) and the target thickness must be decided. These are, of course, correlated parameters; the beam energy is chosen to maximise the desired evaporation channel by selecting a particular compound nucleus excitation energy for nuclei in the centre of the target; the thicker the target, the greater the energy loss of the ion beam up to the centre of target. The optimum excitation energy of the compound nucleus can be estimated with reasonable accuracy using the HIVAP computer programme [Rei85] developed at GSI, a statistical calculation code which models the fusion-evaporation process for an excited compound nucleus. If this optimum energy is achieved at the centre of the target then a range of energies (~5MeV) at either side will also be included. The target thickness is chosen by balancing the demand for a high yield of reaction products (which requires a relatively thick target) with

the need to ensure that the energy spreading of the recoils due to multiple scattering is not greater than the acceptance of the FMA (which limits the useful target thickness if the separation process is to remain efficient). In practice, the target thickness is nearly always on the order of 0.5-1 mg/cm^2.

A selection of targets were mounted on a 'ladder', which could be easily raised or lowered to change target type. In order to disperse the heat deposited by the beam over a large area of the target rather than one small spot (which can easily destroy the target when high beam currents are used), the target can be rotated and the beam 'wobbled' (oscillated vertically). Both of these methods were employed in the experiments described in Chapter 4.

A 20μg/cm^2 carbon reset foil is placed a few centimetres downstream of the target to equilibrate the charge state of recoils before they enter the FMA.

3.3 The Fragment Mass Analyser

The FMA [Dav89, Dav92] is an 8m long recoil mass spectrometer used for separating nuclear reaction products (see figures 3.1 and 3.2). Its main components are two electric dipoles (with maximum fields of 50kV/cm) symmetrically placed before and after a 40° magnetic dipole (with maximum field 1.1T). The FMA separates the reaction products from the primary beam and then disperses them achromatically according to their mass-to-charge ratio (A/Q) at the focal plane. This design results in a high acceptance in energy (±20%), A/Q (±7%) and solid angle (∼ 8msr), with a consequent transmission efficiency of typically 10-20% , depending on the particular reaction. In the original FMA design, the unreacted primary beam normally

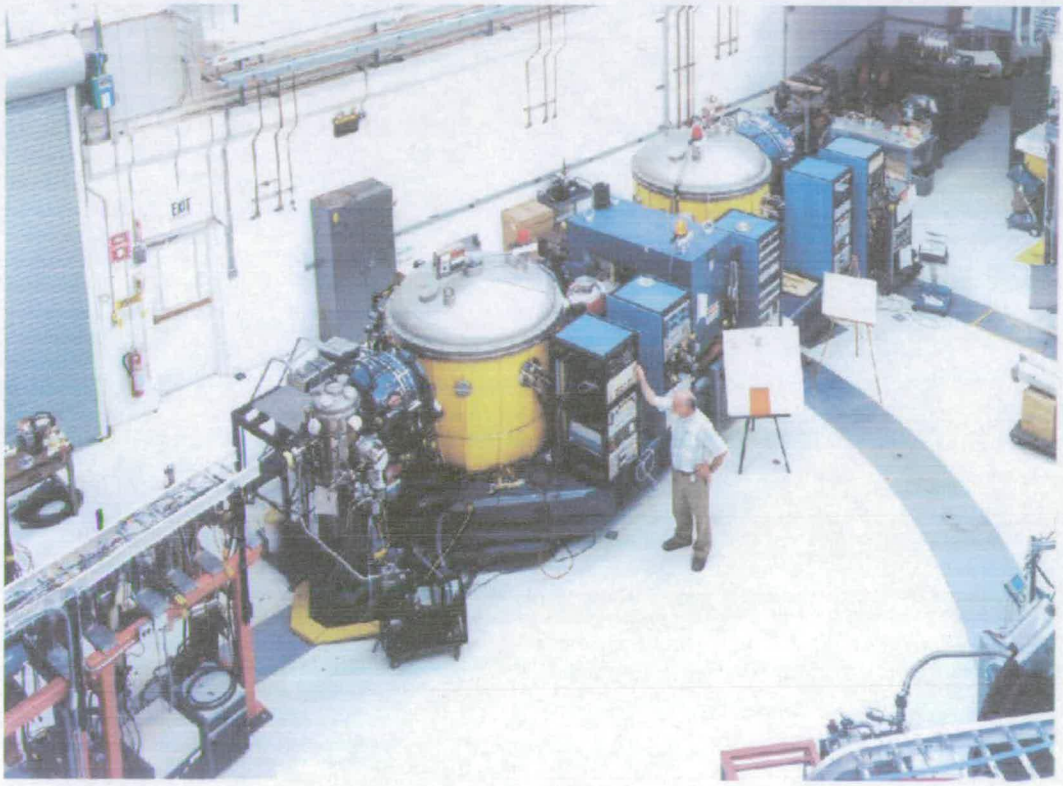

Figure 3.1: *The Argonne Fragment Mass Analyser.*

stopped on the anode of the first electric dipole, although multiple scattering resulted in a small fraction of beam passing through the separator and reaching the focal plane (beam rejection $\sim 10^{-12}$), which was sufficient to approach the maximum rates at which the focal plane detectors could be run (particularly when utilising inverse kinematics). Between the ^{135}Tb experiment and the ^{125,126}Pm search, the anode of the first dipole was replaced with a 'split' anode, which allows the primary beam to pass through a small slit and be stopped on a tantalum plate inside the anode. This upgrade further reduced the scattered beam problem by a factor of eight (as measured using the reaction ^{58}Ni + ^{92}Mo to produce the proton emitter ^{147}Tm via the (p2n) evaporation channel [Dav02]). Quadrupole doublets at either end of the FMA assist in geometric focusing and solid-angle enhancement; the aperture diameter of the exit quadrupole is larger than that for the entrance in order to accommodate the dispersed masses. The FMA can be rotated about the target position, in reaction mechanism studies for example, but in this experiment was used in the 0° orientation. The resolution achieved by the FMA is on the order of d(A/Q)/(A/Q) $\sim$ 1/350. The (A/Q) dispersion at the focal plane is typically 10mm per percentage mass difference, e.g. 10mm between adjacent masses at A=100, which can be easily resolved by position-sensitive detectors.

All the power supplies for the ion-optical elements of the FMA are controlled and monitored by a custom application programme [Dav94] running on a dedicated computer, a Macintosh IIcx. In addition, the programme monitors vacuum conditions, conditions the electric dipoles and controls the magnetic fields in a feedback loop with field sensors. The FMA is prepared for the transmission of a particular recoil by entering the energy, mass and

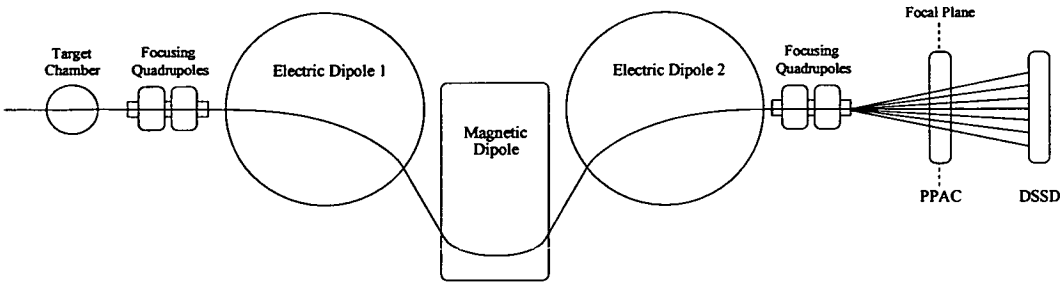

Figure 3.2: *Schematic of the Argonne Fragment Mass Analyser.*

charge state of the particle into the programme, which then calculates and implements the required fields. A web-based code [Blu96] can be used to calculate the energy and optimum charge state of the desired recoil, given the beam and target parameters. In fact, the FMA can transmit up to three charge states of the central mass, although the yield of the non-central states can be significantly reduced. During experiments, it is often profitable to change the FMA charge state setting (to a half-integer charge state, for example), or indeed the mass setting, in order to improve the yield by having two near-central charge states of the desired mass (rather than one central and two reduced 'edge' states). Alteration of the A/Q setting can also be useful in reducing scattered beam flux at the focal plane, which can occur if a particular beam charge state gives a very similar A/Q ratio to that of the desired recoil.

3.4 Detection System

The arrangement of the detection system at and beyond the focal plane of the FMA is shown in figure 3.3. The PPAC is situated at the focal plane,

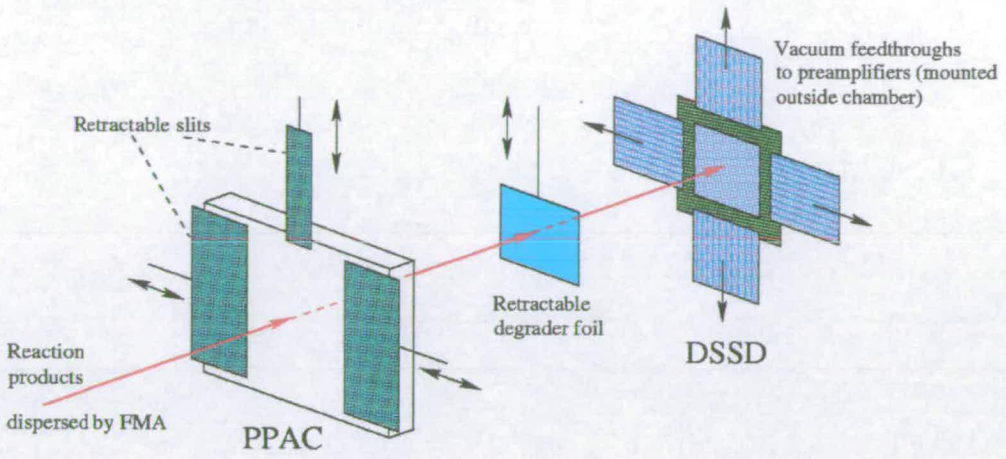

Figure 3.3: *Schematic of the detection system chamber from the focal plane onward.*

and measures the position (i.e. A/Q, as shown in figure 3.4) and energy loss of the recoils moving through it. The recoils then pass through a degrader foil, which reduces their energy (see later), and are finally implanted into the DSSD. The time taken for the particles to traverse the 40cm distance between PPAC and DSSD is recorded by a time-to-digital convertor (usually a few tens of nanoseconds). Each event in the DSSD, either the implantation or the subsequent decay of a recoil, is recorded and time-stamped by a 100ns clock. Implantation events are identified by a PPAC-DSSD coincidence, and decay events by PPAC-DSSD anti-coincidences. The energy with which a recoil enters the DSSD is crucial; if the energy is too high, the system will be 'blind' to decays for a period of up to $\sim 7\mu$s due to amplifier overload (see section 3.5), whereas if the energy is too low the recoils will implant too close to the surface, so that a large fraction of any subsequently emitted particles will escape out of the upstream (front) side of the detector without depositing their full energy. Degrader foils, usually ~ 1mg/cm^2 of aluminium, are used

to reduce the recoil energy to a suitable level (which can be found with a simple energy loss calculation given the usual desired implantation depth of 10-12μm).

Implant-decay correlations within individual 'pixels' on the DSSD are then used to identify known proton or alpha decays and to assign accurate masses to new decays. In the past, decay-decay correlations have also been used to clearly identify daughter and even grand-daughter decays [Dav97]. The rate of implantation of recoils into the DSSD, and therefore fundamentally the beam current, is limited in practice since implant-decay correlations become extremely uncertain when the time between implantation events in a pixel is comparable to the half-life of the implanted nucleus. Assuming the recoils are defocused to uniformly illuminate a 6400-pixel DSSD, a $\sim$ 6kHz implantation rate will give an average time of $\sim$ 1s between implantations in a single pixel, which is usually satisfactory since a typical proton decay half-life is $\sim$ 10ms. However, the condition of the PPAC and the dead-time of the data acquisition system can also act as a limit at rates of $\sim$ 5kHz. The implantation rate can be reduced, while still transmitting the mass of interest, by blocking unwanted masses at the focal plane using mobile 'slits' positioned just before the PPAC. This is usually done by altering the FMA A/Q setting to produce two near-central charge states of the desired mass, then lowering an obstruction between these points to cut out unwanted recoils and finally moving obstructions in from both sides to block everything except the two A/Q states of interest.

There is also a standard triple alpha source in the detection system chamber which can be positioned in front of the DSSD for calibration and gain-matching purposes, and can be used to check for strips which have

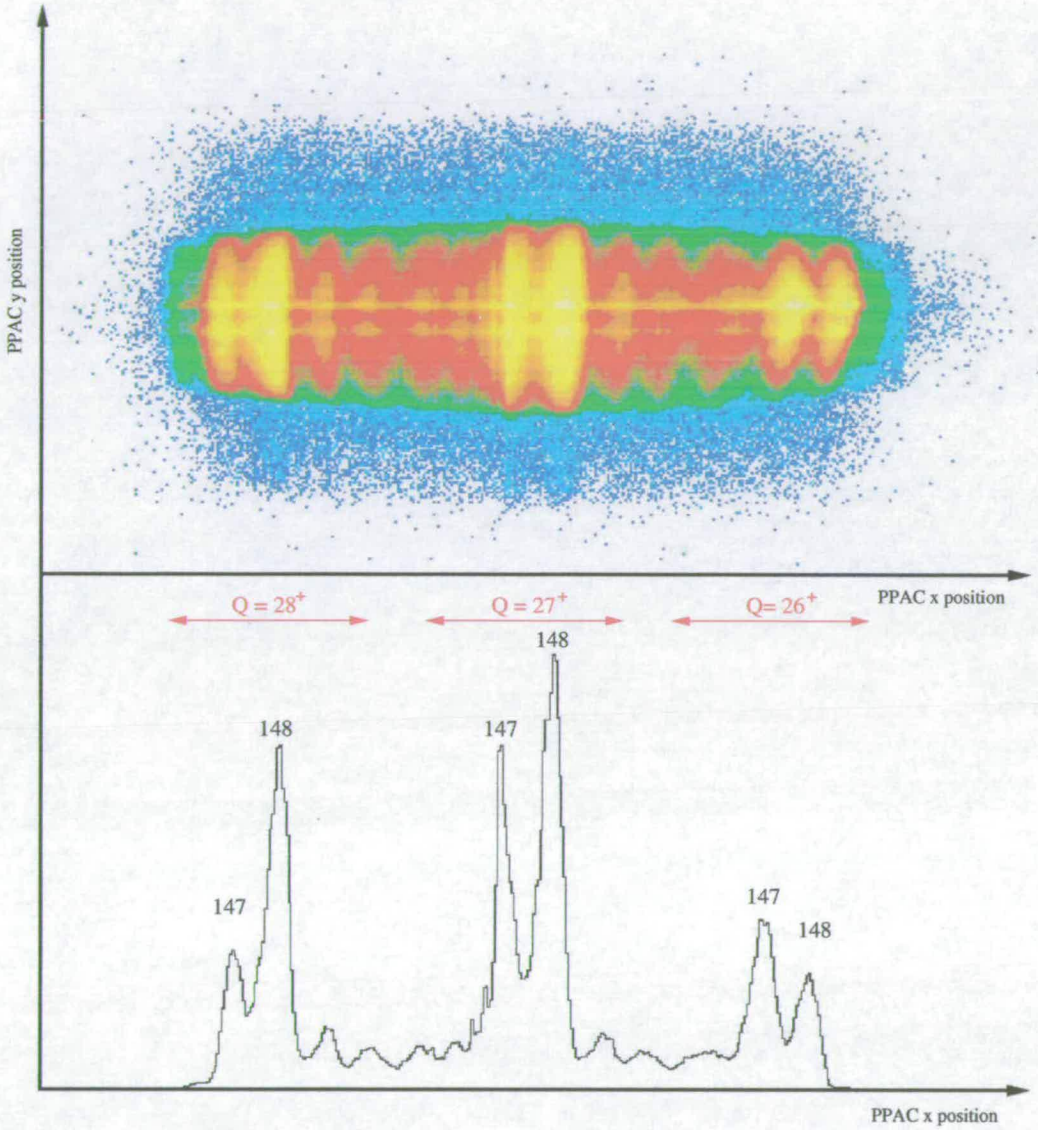

Figure 3.4: *a) Two-dimensional PPAC hit pattern and b) projection onto the x-axis for the reaction $^{92}Mo(^{58}Ni,p2n)^{147}Tm$, with the FMA set to transmit A=147, Q=27+ recoils.*

shifted in gain during the course of the experiment.

3.4.1 PPAC

The PPAC (parallel plane avalanche counter) is a multi-wire proportional counter situated at the focal plane of the FMA. In its original design, it consists of a series of parallel plane wire grids (cathode, x-position, anode, y-position) between thin ($< 1\mu$m) mylar entrance and exit windows, and is filled with isobutane at a pressure of 3 torr. The voltages typically used are -200V for the cathode and 350-400V for the anode. Data on the position of a recoil passing through the PPAC is produced by delay-line readouts from both ends of the two orthogonal position grids. Energy loss information is taken from the cathode, and the anode signal is used to start the time-to-digital convertor (TDC) which records the PPAC-DSSD time-of-flight. This time-of-flight is useful later in differentiating between true recoils and scattered beam.

This PPAC design has a maximum event rate of $\sim$ 5kHz, which can often be the limiting factor in the overall experimental event rate. This limit led to the installation of a new PPAC after the ^{135}Tb experiment but before the ^{125,126}Pm attempt. The new PPAC [Pen01] has cathode and anode planes consisting of mylar foils metallised with gold on each side (instead of wire planes), and has a second cathode between the y-position grid and the exit window. This new design has been shown to run at event rates of up to 20kHz, thus potentially allowing the use of larger beam currents than previously feasible.

3.4.2 DSSD

The key piece of equipment in the whole detection system is the double-sided silicon strip detector (DSSD), which lies 40cm beyond the focal plane of the Fragment Mass Analyser. Until the ^{135}Tb experiment, the experimentalist had a choice of two DSSDs to utilise; one consisting of 40 orthogonal strips on each side, with a strip pitch of 1mm, and the other with 48 strips on each side and a strip pitch of 335μm. The former detector can capture more recoils than the latter due to its larger area, but its inferior 'granularity' (number of strips/pixels per unit area) limits the useful implantation rate for which recoil-decay correlations can be reliably established. Clearly, a new DSSD which could combine the large area of the 40×40 design and the excellent granularity of the 48×48 version would be ideal for improving the system to detect proton emitters with very low production cross-sections. However, there is always a compromise between the reduction of the strip width (and so pixel size) and the corresponding increase in both the dead area on the detector (due to inter-strip separation) and the required instrumentation (amplifiers and ADC channels). A new DSSD with 80 orthogonal strips on each side, with a strip pitch of 400μm (giving only a slightly inferior granularity to the 48×48, and an area large enough to accept the full FMA image) was designed by the Edinburgh group, manufactured by Micron Semiconductors Ltd. and installed at the FMA immediately before the ^{135}Tb experiment.

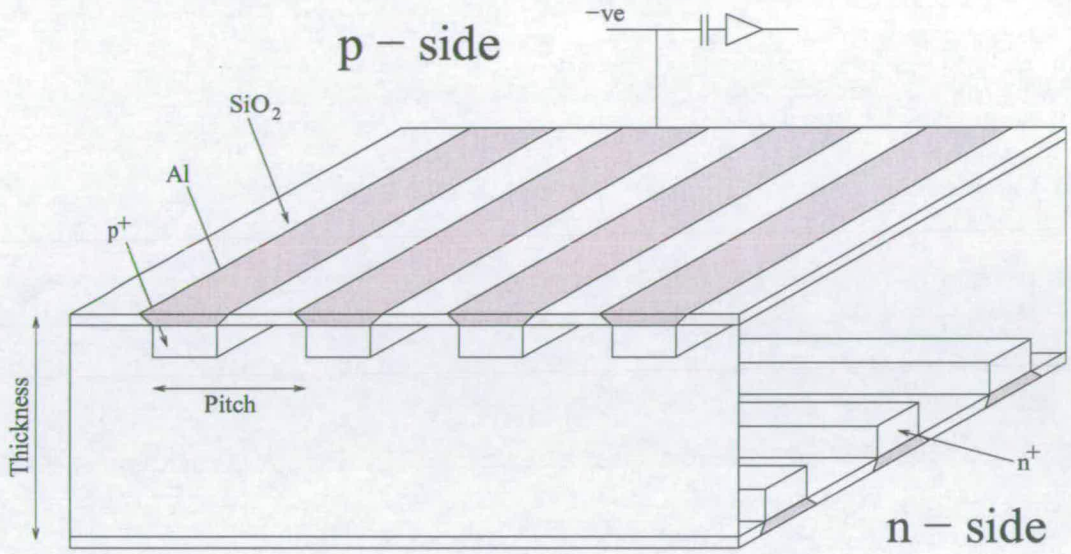

Figure 3.5: *Schematic of the DSSD.*

3.4.3 Design

The detector consists of a slightly n-type substrate with 80 p^+ implanted strips on the front face crossed with 80 n^+ implanted strips on the rear face (see figure 3.5). Each strip has a length of 32mm and an active width of 350μm, which, combined with an inter-strip region of 50μm, gives a total strip pitch of 400μm. The orthogonal strips effectively produce 6400 individual pixels, each identified by the x and y coordinates given by a certain front and back strip number. Signals from adjacent strips are read out from alternate sides of the detector (see figure 3.6). The DSSD has a surface area of 1024mm^2 and a thickness of 70μm. The detector operates as a reverse-biased p-n junction diode, with a negative bias of about -50V applied to the p^+ side through the preamplifiers. The depletion voltage for a detector of this thickness is only about -20V; the DSSD is overbiased to reduce the effect of leakage current fluctuations and to maximise charge collection (a larger

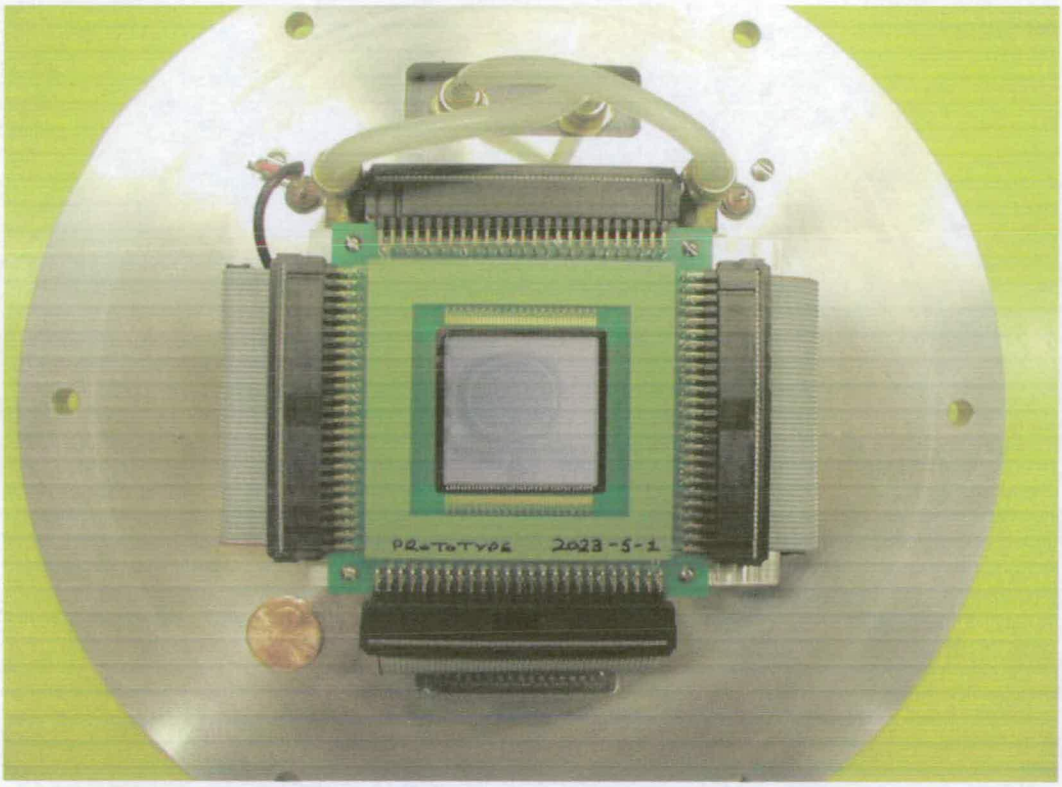

Figure 3.6: *The DSSD mounted on the vacuum chamber flange, showing the cable feedthroughs on each side, coolant tubes (top) and a penny for size comparison (bottom left).*

field will sweep the charge carriers out of the depletion region more quickly and reduce the possibility of recombination). Each strip has an aluminium contact layer to act as an electrode, which is connected to the surrounding wafer by an ultrasonically-bonded fine wire. Each implanting particle must pass through a dead layer of $\sim 0.8\mu$m (comprising the Al contact and the p^+ layer) before reaching the active volume of the DSSD. The detector surface is passivated by an oxide layer to reduce surface-related leakage currents.

The DSSD is specifically designed to be sensitive to proton and alpha decays but virtually transparent to beta decay. A 1MeV proton has a

range of $\sim$15μm in silicon, and a typical 5MeV alpha particle has a range of $\sim$25μm. Such decays would almost certainly be localised within one pixel, whereas a 1MeV β particle with a range of $\sim$1mm would pass through many pixels or more likely escape the detector very quickly and deposit very little energy, probably far below the DSSD amplifier threshold of 300-450keV. This effective β transparency greatly reduces the background seen in this type of experiment compared to the use of a single-segment silicon detector; each pixel effectively operates as an individual, independent detector.

The DSSD is cooled to -25°C during experiments in order to minimise the thermal generation of charge carriers and so optimise the energy resolution, which was expected to be about 20-25keV for alpha particles and about 15keV for protons given the performance of previous detectors (although the resolution inevitably deteriorates as the detector suffers radiation damage from implanted ions over the course of several experiments, as described in Chapter 4).

3.4.4 Other detectors

A thick (300μm), large area silicon detector was positioned immediately behind the DSSD. Its purpose is to detect positrons and β-delayed protons produced by decays within the DSSD, and therefore coincidences between back detector signals and DSSD signals are used to veto DSSD events. This helps to reduce the background around the expected energy range for direct proton emission ($\sim$ 1MeV). As well as this method for vetoing particles escaping from the DSSD in the forward direction, a similar technique has previously been used to detect particles escaping in the backwards direction

(i.e. through the front face of the DSSD). The so-called 'Box' detector, not used in these experiments, consists of four silicon strip detectors forming the four sides of an open-ended box upstream of the DSSD and covers ~75% of the solid angle in this direction. For the ^{125,126}Pm experiment, a Germanium detector was placed outside the vacuum chamber, immediately behind the flange, in order to identify gamma decays taking place within the DSSD and hopefully confirm the PPAC mass assignments (as described in Chapter 4).

3.5 Electronics

Over the years, the Edinburgh group has designed a dedicated suite of electronics to instrument double-sided strip detectors. The signals from the DSSD pass out of the vacuum chamber through cable feedthroughs and into the charge-sensitive preamplifiers mounted on the rear plate of the chamber. It is necessary to locate the preamps as close as possible to the detector to minimise the capacitance (and therefore the noise) related to the length of the cables from the detector. Each strip is instrumented individually, and each side of the DSSD requires a different form of preamp because the signals are of opposite polarity. The preamplifiers have a sensitivity of 20mV/MeV and a dynamic range of 0-200MeV.

The signals are then fed via ribbon cables into the shaping amplifier stage. This section consists of two sets of 160 Edinburgh/RAL shaping amplifiers, one with a dynamic range of 0-200MeV (over an output range of 0-10V, gain=5), to measure the high energy implantation events in both sides of the DSSD, and another set with higher gain (=50, giving 0-20MeV dynamic range) to measure the decays. These shaping amplifiers are mounted

in sets of eight on Eurocard motherboards and produce output signals suitable for analogue-to-digital convertors (ADCs), with a rise time of roughly 1μs and a tail lasting for 4-5μs. Each amplifier also has a leading-edge discriminator which produces logic pulses (ECL) for triggering. DC offset and pole-zero can be adjusted with potentiometers on each amplifier, but there is only one potentiometer for each motherboard to set a common discriminator threshold level for all eight amps (which is usually set as low as electronic noise allows). The amplifiers are designed to have a reasonably quick overload recovery, because the high-gain decay amps are also exposed to the high energy implantation signals which have the effect of saturating them. If the implantation has an energy of more than four times the full decay amplifier range (i.e. $\sim$ 80MeV), this produces a DC pedestal effect which can leave the amp insensitive to decays for hundreds of microseconds. This is the reasoning for introducing a degrader foil in front of the DSSD to limit the implantation energy of recoils from the FMA. In order to instrument the 80×80 DSSD, a new set of 64 preamps, recoil amps and decay amps had to be tested and installed, necessitating a total reorganisation of the electronics arrangement.

Overload recovery of the shaping amplifiers is a key issue for detecting short-lived proton radioactivities. There are several proton emitters (for example ^{113}Cs and ^{171}Au) with half-lives on the order of a few microseconds, whose detection is impaired when using the shaping amplifiers described above. For example, even if the decay amp is no longer overloaded after an implantation, a decay signal 10-15μs later may be riding on the tail of the recoil pulse and so may appear to have a significantly higher energy than in reality i.e. the measured energy is time-dependent for very fast times.

To increase the sensitivity of the detection system to fast proton emitters, a new set of delay-line shaping amplifiers was designed and built at Argonne between the ^{135}Tb experiment and the ^{125,126}Pm search which could recover to baseline within $\sim 1\mu$s after an implantation. This time is very close to the actual flight time of a recoil from target to DSSD, which imposes the physical lower limit on decay time observability. This new delay-line system runs in parallel with the Edinburgh/RAL electronics, and was used successfully in the ^{125,126}Pm attempt and other experiments [Rob03].

The analogue signals from the decay amps are fed into a bank of ten Philips peak-sensing ADCs in a CAMAC crate, and the signals from the recoil amps are digitised using the more cost-effective method of pulse-to-charge (PTQs) followed by charge-to-digital convertors (QDCs) in another CAMAC crate. The latter method offers inferior resolution to a single stage ADC, but the energy resolution of the recoils has to be known only approximately (for the purposes of vetoing scattered beam) and this latter method is satisfactory.

Logic signals for decay triggering were taken first from the Edinburgh/RAL shaping amplifier discriminators and then later from the Argonne delay-line amplifiers (when they became available). Logic signals for recoil triggering come from the PPAC rather than the DSSD system. The ECL signals from the decay amps are fed into modules which produce an OR of input signals 1-16, 17-32, 33-48, 49-64 and 65-80 for both the front and back sides of the detector, and these outputs produce an ADC hit pattern. Total OR signals for each side of the detector are also produced, DF and DB, and a coincidence between these two produces a valid DSSD event (i.e. at least one front and one back strip fires). The PPAC anode signal is

used to generate coincidences and anti-coincidences between the PPAC and DSSD; the former signifying a recoil event (event type 1), the latter a decay (event type 2). These signals are used to set the relevant bit in the event type word, gate the ADCs, strobe the ADC hit pattern register, latch the clock and trigger the acquisition system. When the event has been read out, a signal is produced to clear the ADCs and QDCs, and the system is ready for a new event. Figure 3.7 illustrates the logic system.

The data acquisition system used was the MSU/NSCL system. The front end is a VME-based system in which a master programme packs the events into buffers and send them across an ethernet link to the back-end Alpha computer which routes the data to tape, on-line analysis or scaler as necessary. When a trigger is accepted, a slave programme on the VME system reads the data from the required ADCs or QDCs in the CAMAC crates, and also reads the clock to time-stamp the event. The slave programme is written in C, and was relatively simple to modify to cope with the new DSSD and associated electronics. The readout time is typically a few hundred microseconds, which means that decays with an implant-decay correlation time shorter than this cannot be treated as an individual event. Instead, the decay busy signal is vetoed (to allow new decay data to be read) after the electronics common to both implantations and decays is read out, then the implant-only electronics is read out, and then the slave checks to see if a new decay has occured during this period. If there is a new decay, a '1' bit is placed in the event stream to indicate a 'fast decay' and the decay data is added to the end of the implantation event. This method reduces the effective implant-decay dead time to less than 10μs, compared to the implant-implant dead time of up to $\sim 500\mu$s, which is just about acceptable

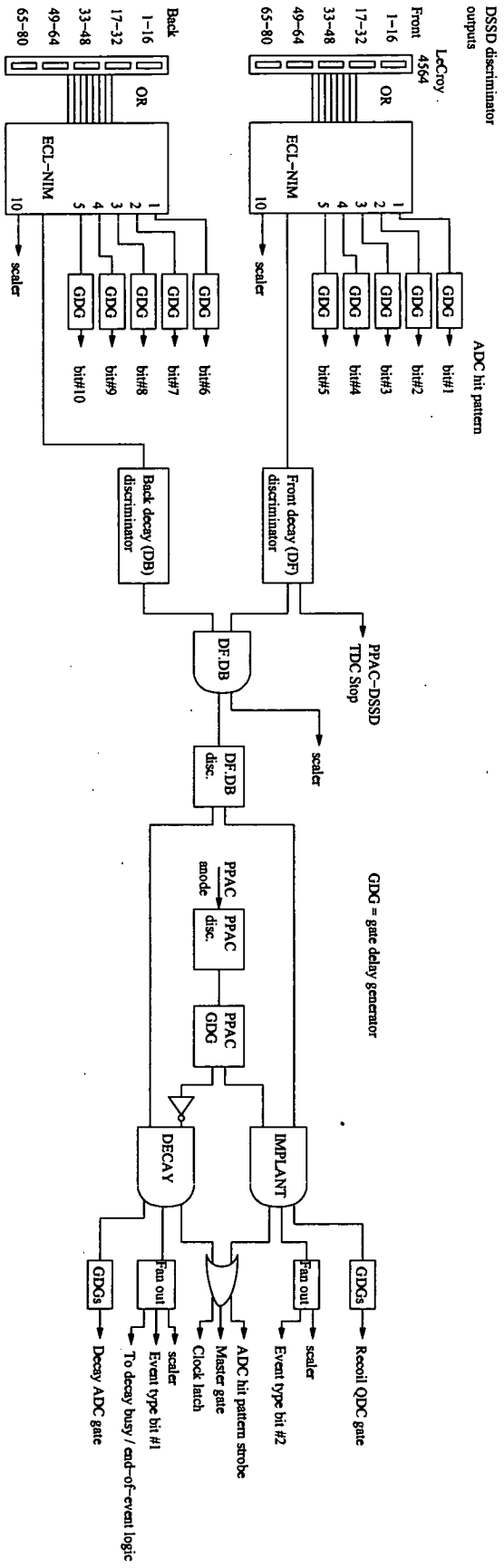

Figure 3.7: *Schematic of the trigger logic for the DSSD system.*

given a typical DSSD implant rate of 2-5kHz.

3.6 Setup and calibration of detector system

As mentioned earlier, a web-based setup code [Blu96] is used to calculate values for the energy and charge state of a desired recoil given input variables such as beam energy and species, target material and thickness, and the mass and Z of the recoil. The resulting values are then fed into the FMA control computer which sets the electric and magnetic dipole fields accordingly. The thickness of the degrader foil upstream of the DSSD can also be selected with the setup code to limit the implantation energy of recoils and prevent amplifier overload.

The beam is initially set to a much lower current than its full experimental state, in order to ensure that the FMA is functioning properly and that no detectors can be damaged by a high flux of beam particles or recoils. For example, it is possible that the beam could be impinging on the target frame rather than the target itself, scattering a large proportion of beam particles. The DSSD is usually masked when beginning setup by closing a valve immediately downstream of the PPAC. The on-line spectra produced by the PPAC are used to check whether the FMA has the optimum settings for detecting the recoil of interest. For example, the FMA usually transmits three different charge states of a particular mass, but the transmission of the two states towards the edges may be significantly weakened. It is therefore common to alter the FMA settings to transmit two near-central charge states instead, and in this way the slits immediately upstream of the PPAC (as shown in figure 3.3) can be used to cut out all other A/Q states. There

can be problems if the mass-to-charge ratio of scattered beam particles is close to that of the recoil of interest, so it may be necessary to move to a neighbouring recoil charge state to avoid swamping the detectors with scattered beam. Scattered beam is an issue in terms of radiation damage of the DSSD, false implant-decay correlations and also the rate limit of the PPAC (although this latter problem has been alleviated by the installation of the new high-rate PPAC). The scattered beam problem is exacerbated when using inverse reaction kinematics, but this was not the case in the experiments discussed here.

After the experimentalist is satisfied with the FMA settings, the DSSD can be exposed to recoils and the system checked to make sure it is operating within acceptable parameters. In particular, the pole-zero settings of the decay amplifiers must be checked to ensure that there is no significant long-lived baseline undershoot after the implantation signals which would effectively reduce the amplitude of subsequent decay signals and ruin the energy resolution. The overload recovery response must also be checked for the pedestal effect mentioned previously, and a thicker degrader foil can be inserted at this point if necessary. The 160 strips of the DSSD can be roughly gain-matched (i.e. each strip calibrated with its own gain and offset value) using a triple alpha source (^{241}Am, ^{240}Pu, ^{244}Ca) which can be positioned in front of the detector in the vacuum chamber. This calibration must take into account variable dead layer effects; the source is positioned close to the centre of the DSSD, so that alphas implanting into strips near the detector edges must pass through a thicker dead layer and thus lose more energy than alphas implanting into the centre.

Event rates in the detectors (for example PPAC, DF, DB, DF AND

DB, all typically around 3k-5k per second in this work) are displayed as scalers, indicating the onset of any problems such as the failure of the target (sudden increase in implantation rate) or electronic noise problems on one side of the DSSD (a sudden increase in DF without a concomitant increase in DB, for example).

3.7 Data Analysis

The analysis utilises correlations in position (i.e. in a single DSSD quasi-pixel) and time between implantation events and subsequent decay events to provide a parent nucleus mass assignment for peaks in the decay energy spectrum. Implantation and decay events are treated entirely separately in the sorting code, in terms of having different vetos and conditions placed on them. 'Fast decay' events, where decay data is appended on to an implantation event, are processed by both the implant and decay sections of the sorting code. The only hardware condition applied to DSSD events is that the events should have multiplicity ≥ 1 on each side i.e. at least one strip on each side of the detector should fire for a valid event. However, some multiplicity = zero events, false triggers caused by electronic noise, are inadvertently recorded.

3.7.1 Implantation Events

The implantation strips were not gain-matched because the energy resolution for implantation events does not need to be particularly accurate for the purposes of this analysis. For each event, the multiplicity condition is checked (≥ 1 on each side) and the strip with the highest energy signal on

each side is used to reference a particular pixel. Data from the PPAC (two-dimensional position of the transmitted particle, energy loss of the particle) is recorded in the event, along with the PPAC-to-DSSD time-of-flight, and this data is analysed and used to investigate whether the particle in question is a true fusion-evaporation recoil or a scattered beam ion. This is usually achieved by one of two methods. In the first, a two-dimensional spectrum of DSSD implantation energy against PPAC-DSSD time-of-flight is plotted, and two distinct groups can be discerned due to the significant difference in masses between beam and recoils (the energy is roughly proportional to the particle mass and inversely proportional to the square of the time-of-flight). The second method is to produce a two-dimensional plot of PPAC horizontal position against PPAC energy loss, which shows the familiar A/Q groups over a background with lower energy loss (the beam particles). This agrees with the expectation that a scattered beam particle will lose significantly less energy than a recoil in the PPAC due to the former's higher speed and likely lower charge state. When the sort code identifies a valid recoil event, it stores the PPAC horizontal position and implantation time in an array, referenced by its associated front and back strip numbers. This information can then be correlated with the next decay event to occur in the same pixel.

3.7.2 Decay Events

The sorting code first double-checks that the decay event is definitely not an implantation event, by checking for a PPAC cathode (energy loss) signal. Although the hardware should differentiate between implantations and decays using PPAC-DSSD coincidence and anti-coincidence respectively, oc-

casionally the PPAC anode may not fire and a recoil may be recorded as a decay event. The PPAC cathode data is included in the decay event as a final check, although this stage is rarely needed in practice since a stow-away implantation event is unlikely to have an energy as low as the typical 0-6MeV range of decay processes. As with the implantation events, the sorting code applies a multiplicity check to the decay events. Only events with multiplicity one on each side are wanted; a larger multiplicity on one or both sides of the detector implies that the charge produced by the event has been shared between multiple adjacent strips, and thus no accurate energy measurement can be made. The single multiplicity condition is also important for vetoing β-decay events. Given the performance of past detector systems, it was expected that $\sim$ 90 % of decay events would pass the single multiplicity condition. The decay ADC output is then calibrated using that strip's unique gain-match parameters (gain and offset) determined by a calibration reaction run immediately before the main experiment. In the case of these experiments, the calibration reaction used was ^{58}Ni + ^{92}Mo $\rightarrow$ ^{150}Yb* $\rightarrow$ ^{147}Tm + p2n, producing the proton emitter with the highest production cross-section. To have an accurate calibration it is important to have as many statistics as possible in all the strips (particularly the edge strips which receive less of the FMA image than the central strips), and because the time to run the calibration reaction is strictly limited, it is best to use the most readily-produced proton emitter. ^{147}Tm is also advantageous because it has two proton-emitting states, the ground state and an isomer, although the isomer is usually not produced in sufficient quantities to use as a calibration point for individual strips (but can still be used as an overall gain-matching check). It is important to use a proton for calibration

rather than rely only on alpha decays because it is vital to have at least one data point in the likely proton energy region (~1MeV) to ensure the reliability of the calibration. Two alpha decays are also used in the calibration; these are among the well known alpha lines which appear in the calibration from recoils produced by reactions with isotopic target contaminants (such as ^{94}Mo). Care must be taken when combining proton and alpha lines in a calibration, because the two particles have a slightly different pulse height response in a silicon detector. The cause of this effect is not entirely clear, but the difference in response has been accurately quantified with the ratio $E_p/E_\alpha = 0.986(2)$ ([Len86]), i.e. a proton with energy 1MeV produces a pulse height ~1.4% lower than an alpha particle with energy 1MeV. The recoil energy of the daughter nucleus of these decays is also partially detected by the DSSD and must be accounted for; most of its energy is lost in elastic non-ionising collisions with the atomic lattice ([Hof82b]). As opposed to the on-line calibration with the external triple alpha source, these decays occur inside the detector and thus no surface dead layer effects have to be considered. Several other conditions are applied to decay events, including an 'equal energy' condition where events are rejected unless the energy values measured on both sides of the DSSD are within 20keV. As mentioned previously, events are vetoed if they are coincident with an event in the back Si detector, indicating that a particle has escaped from the DSSD into the other detector and therefore the energy measured in the DSSD is not the total energy.

3.7.3 Mass Assignment of Decays

In order to reliably correlate decays with their preceding implantation events, the average rate of implantations in a pixel has to be significantly longer than the expected decay half-life. This condition is satisfied by ensuring that the total DSSD implantation rate is on the order of 5kHz, giving roughly 1 implantation per pixel per second (assuming uniform irradiation over the 6400 pixels), compared to typical alpha and proton decay half-lives on the order of 10-100ms. The sort programme accesses the implantation array and retrieves the PPAC horizontal position and time of the last valid recoil event occuring in the same pixel as the decay event being analysed. The mass of the decaying nucleus can then be derived from the PPAC x data, for example in a two-dimensional plot of DSSD decay energy against PPAC x position. A short piece of code at Argonne calculates the expected PPAC x position of the various possible A/Q states in the reaction, once the 'centre' of the PPAC has been defined in the calibration reaction, allowing an unambiguous mass identification of the peaks in PPAC x spectra. The time of the last implant event in the pixel can then be subtracted from the decay event time to give the implant-decay correlation time, which can then be used to apply time gates to the decay data. For example, one can look at fast or slow events to preferentially search for short-lived or long-lived decays respectively. Once a decay line is located, the correlation time data is finally used to calculate the decay half-life. With heavier nuclei, decay-decay correlations are often possible too i.e. when the proton or alpha decay daughter also has an identifiable alpha decay branch. However, there are no alpha emitters in the mass region under investigation in these experiments and so

this technique could not be used.

Chapter 4

Results and Discussion

The results presented in this thesis are taken from experiments carried out in 2001 and 2002 at Argonne National Laboratory, and the analysis was performed by myself. The discovery of a proton-emitting state in ^{135}Tb was first reported in [Sew03], and is published in full in [Woo04]. The unsuccessful searches for proton emission from ^{125}Pm and ^{126}Pm are presented here for the first time.

4.1 Commissioning of new DSSD

The first experiment using the new 80x80 double-sided silicon strip detector, the search for proton radioactivity from ^{135}Tb, was carried out in July 2001 at the Argonne Fragment Mass Analyser. Immediately before this experiment, a brief commissioning and calibration run was performed using a 270MeV ^{58}Ni beam on a 0.775mg/cm^2 ^{92}Mo target to produce the well-known proton emitter ^{147}Tm [Kle82] via the (p2n) evaporation channel, which has a relatively large cross-section of $\sim 30\mu$b.

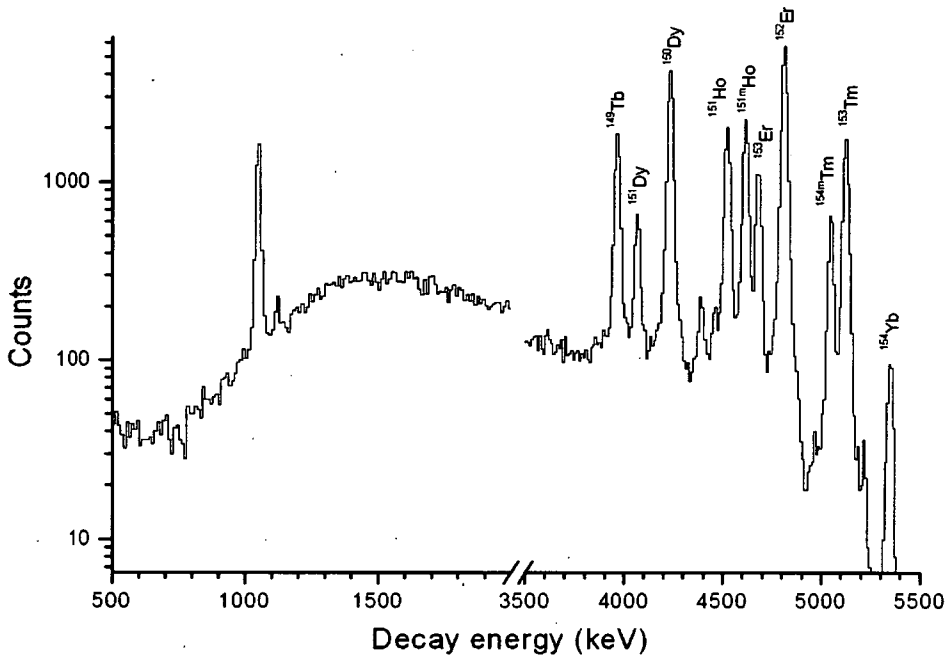

Figure 4.1: *Decay energy spectrum from* ^{147}Tm *commissioning run.*

In this reaction, a number of alpha emitters are produced in addition to the proton emitter ^{147}Tm due to the presence of isotopic target contaminants (i.e. the presence of less neutron-deficient molybdenum isotopes in the target, despite efforts to make it isotopically pure). These are shown in Figure 4.1, along with the 1.051MeV ^{147}Tm proton line from the ground state decay and the smaller 1.119MeV from proton decay of the ^{147}Tm isomer. Note that these events are sitting on the tail of a distribution produced by escaping alpha particles. It was found that the energy resolution of the proton peaks was around 15keV FWHM, and around 20-25keV FWHM for the alpha peaks - this is consistent with the performance of DSSDs previously used by the Edinburgh group [Sel92a]. It was found that the front face of the DSSD had marginally better energy resolution than the rear side, which agrees with the generally superior properties of the front face (as explained below).

Usually a single strip multiplicity condition is required for each face of the DSSD when running experiments, so that any event which triggers more than one strip on either side is discarded. Proton radioactivity typically involves energies of $\sim$1MeV, which means the protons have a range of $\sim 15\mu$m in silicon. Given a strip pitch of 400μm, the vast majority of proton events should be single multiplicity as the particle does not usually have sufficient energy to reach an adjacent strip. Figure 4.2 shows a plot of front side decay energy against rear side decay energy with single multiplicity conditions on each side, with the ^{147}Tm proton line and alpha lines indicated. As expected, the vast majority of events are concentrated on the 'equal energy' diagonal. However, events can be seen in horizontal strips to the left of the peaks (highlighted in red boxes for the proton line and the four main alpha

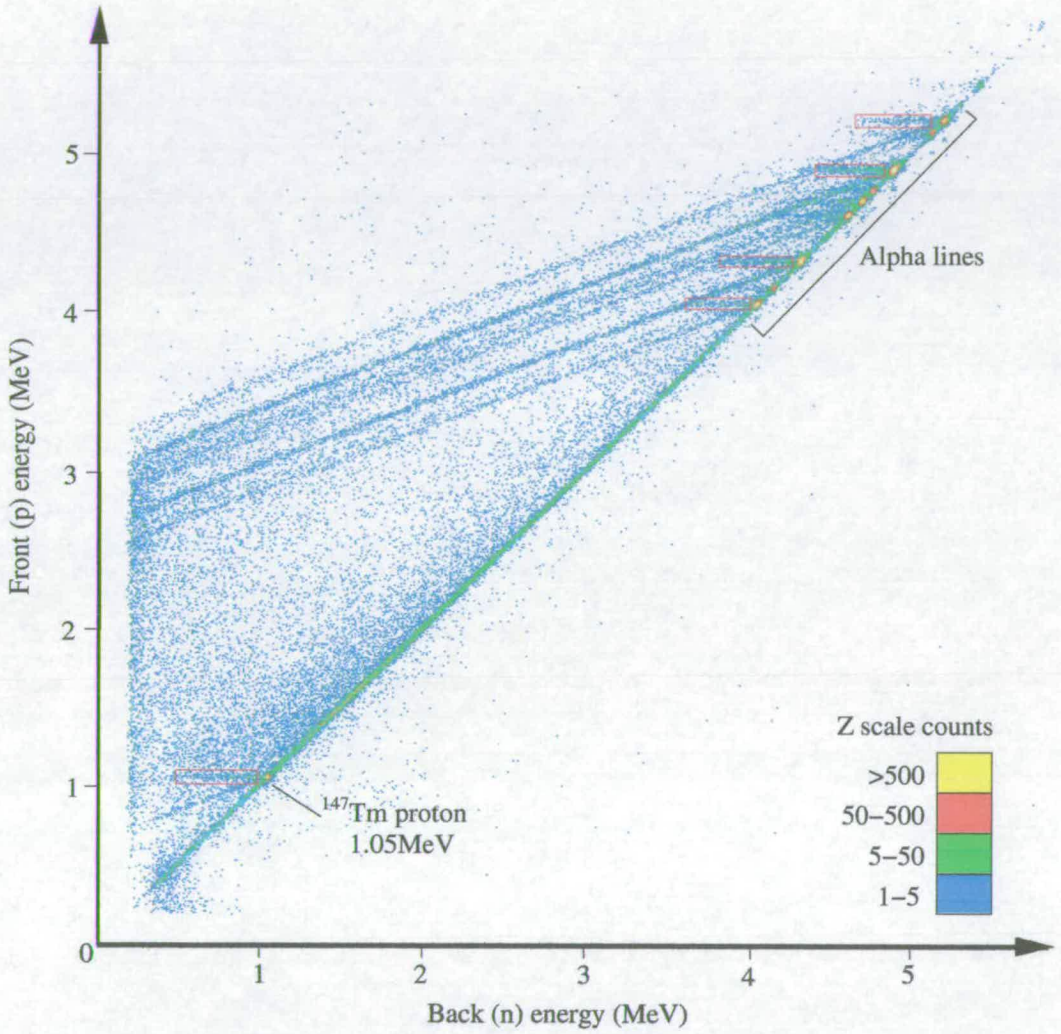

Figure 4.2: *Front decay energy vs. rear decay energy in the DSSD with single multiplicity conditions. The red boxes indicate events where a portion of the charge on the rear face strip has been shared with an adjacent strip.*

lines) which indicate that some charge sharing occurs on the rear face of the DSSD. This is demonstrated by the fact that although $\sim$ 98% of the events have single multiplicity on the front face, only $\sim$ 90% of the events have single multiplicity on the rear face, with $\sim$ 9% having a multiplicity of two, indicating the sharing of charge between two adjacent rear strips. Figure 4.3 is a similar plot to the previous figure, but with the conditions of single front face multiplicity and double rear face multiplicity (with the rear energy plotted being the higher of the two). One can see in this plot the continuation of the horizontal strips of events from the previous plot; the strips of charge-sharing events are split between the two plots due to the $\sim$400keV energy threshold of the detector system, which means that at least this amount of energy must be deposited in a strip for an event to be triggered. Thus the charge-sharing events in the first figure extend to $\sim$400keV below the peaks, with events where >400keV is shared appearing in the second figure. Note also that the charge-sharing events halt at the point where front energy equals twice the rear energy (the red dashed line in the figure) - this is due to the fact that only the higher of the two rear energies is plotted.

A noticeable feature of Figure 4.2 is the presence of the diagonal lines dropping down from the main peaks, at an angle of $\sim$ 25° to the main diagonal. These lines represent events with a reduced energy in both the rear and front face signals, which are rejected by the equal energy condition in the software. Yorkston *et al* [Yor87] propose a charge trapping mechanism which causes reduced charge collection for those particles depositing energy close to the surface inter-strip region. These events could be explained if the resulting deficit in the charge collected at the front face is half of that

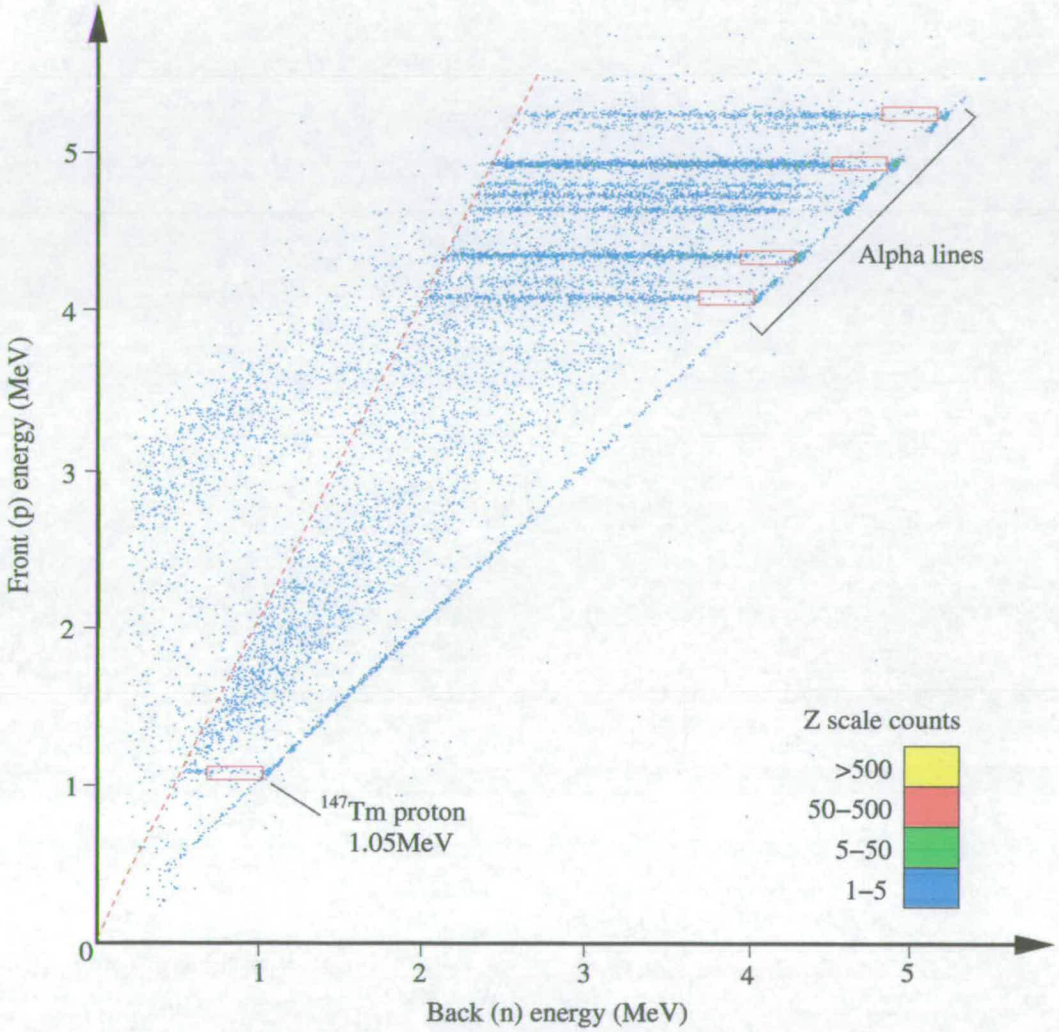

Figure 4.3: *Front decay energy vs. rear decay energy in the DSSD with single front multiplicity and double rear multiplicity. The red boxes indicate the lack of double rear multiplicity charge sharing events where the amount of charge shared is less than the detector threshold.*

in the charge collected at the rear face. This undesirable property has been observed previously in DSSDs [Sel92b]. This effect is due to the construction of the detector - the rear strips are created by implanting n^+ strips onto the n-type substrate with thin p^+ isolating lines between them to provide interstrip resistance to disconnect the n^+ strips. There does not seem to be any correlation between the charge-sharing and signal loss events and any particular strips on the detector (e.g. the edge strips, which often display increased electronic noise) - the effects occur uniformly over all rear strips.

As seen in previous DSSD systems, the recoil multiplicity characteristics of the detector were noticeably inferior to the decay branch, with, in this case, ~80% of implantation events having single front multiplicity and only ~60% having single rear face multiplicity. The recoil signals are handled by different shaping amplifiers to the decay signals, and this effect has previously been attributed to pick-up in this recoil branch aided by the much larger pulses (a typical implantation event has energy of 30-50MeV, compared to the typical 1-5MeV range of decay events).

There was no noticeable degradation in the energy resolution of the detector due to radiation damage during the course of the ^{135}Tb experiment. However, prior to the experiments searching for proton emission from ^{125,126}Pm it was noted that the resolution had degraded significantly (from ~15keV to ~50keV FWHM). It was estimated that the level of degradation and the amount of implantations the detector had been exposed to in the intervening period was roughly consistent with the effects observed by Livingston *et al* [Liv96] in a previous study of heavy ion radiation damage in DSSDs. In that work it was estimated that a dose of $\sim 6 \times 10^6$ fragments mm^{-2} for illumination on the p^+ detector face would produce a similar en-

ergy resolution degradation to that observed in the current DSSD, which was estimated to have suffered a dose of $\sim 2 \times 10^7$ fragments mm^{-2} (assuming near-uniform illumination). The two dosage figures perhaps should not be directly compared since the detector tested in the previous work had failed to meet the quality assurance criteria for commercial use. A new DSSD, identical in design and with very similar performance characteristics, was installed at the FMA prior to the ^{125,126}Pm searches to ensure that the experimental energy resolution was optimal. The radiation-damaged DSSD could still be used in experiments where the energy resolution was not critical, for example the investigation of ^{150}Lu [Rob03] where the key issue was the measurement of the half-lives of the two known proton-decaying states.

4.2 Proton radioactivity of ^{135}Tb

4.2.1 Previous search experiments for proton emission from Tb isotopes

Soon after the discovery of ground state proton radioactivity from the lanthanide nuclides $^{147}_{69}$Tm and $^{151}_{71}$Lu at SHIP and the on-line mass separator at GSI in 1982, a series of experiments were carried out at that laboratory searching for further examples of proton decay from isotopes of the odd-Z lanthanide elements Prometheum, Europium, Terbium and Holmium (Z=61, 63, 65 and 67 respectively) [Lar83]. The experiments searching for proton emission from ^{136,137,138}Tb used 200-240MeV beams of ^{40}Ca from the UNILAC accelerator impinging on a 1.07mg/cm^2 ^{102}Pd target to produce the desired nuclides by heavy ion fusion-evaporation (pxn) reactions. The

specific evaporation channels from the compound nucleus ^{142}Dy* are x=3, 4 and 5 for ^{138}Tb, ^{137}Tb and ^{136}Tb respectively, with the associated production cross-sections calculated by HIVAP [Rei85] to be 120μb, 1.9μb and 180nb. The evaporation residues were stopped in a thermal ion source, then separated according to their mass and finally implanted into a thin carbon foil placed in front of ΔE-E telescopes. The system was designed so that $\sim$1MeV protons would be stopped in the thin ΔE detector, but positrons and higher energy β-delayed protons would pass through to the E detector, so that directly-emitted protons could be picked out in the energy spectra of the ΔE detector in anticoincidence with the E detector. These experiments showed no evidence for proton emission from any of the Terbium isotopes, although the nature of mass separator experiments, due to the delay between creation of the evaporation residue and its subsequent release from the ion source, means that nuclides with half-lives below $\sim$ 1ms are usually not detectable. A similar experiment was undertaken [Nit83] at the OASIS on-line isotope separator at Berkeley, utilising a 480MeV ^{92}Mo beam and a 1-2mg/cm^2 ^{50}Cr target to search for ^{137}Tb via the (p4n) evaporation channel. Again, no evidence for proton emission was found.

More recently, an experimental search for proton radioactivity from ^{136,137}Tb was undertaken at the Oak Ridge recoil mass separator in tandem with a DSSD-based detection system [Ryk99]. A 15pnA, 290MeV ^{50}Cr beam from the Holified Radioactive Ion Beam Facility (HRIBF) was used to bombard a 0.91mg/cm^2 ^{92}Mo target for 35 hours, but no proton decays were observed. The Oak Ridge team point out that the proton separation energy of ^{136}Tb may well be less than, or only slightly greater than, that of its odd-even neighbour ^{137}Tb, an effect demonstrated in the proton-emitting

isotopes of the odd-Z neighbour Holmium, ^{140}Ho and ^{141}Ho (E_p=1086keV and 1169keV respectively). Möller *et al* [Mol97] predict Q_p for ^{136,137}Tb to be 540keV and 510keV respectively, which would not lead to proton emission fast enough to compete with β decay, and therefore is consistent with the experimental non-observation of proton radioactivity from these nuclides. The Liran-Zeldes model predicts slightly larger Q_p values for ^{136,137}Tb of 1MeV and 0.79MeV respectively, in which case a proton decay branch in ^{136}Tb could potentially exist.

4.2.2 Experimental details and results

The search for proton emission from ^{135}Tb at the Argonne FMA was undertaken immediately after the commissioning of the new 80×80 DSSD. A beam of ^{50}Cr ions with energy 315MeV and average current 10pnA from the ATLAS accelerator was used to bombard a rotating 0.775mg/cm^2 ^{92}Mo target for approximately 96 hours. The beam energy was selected to produce the optimum centre-of-target excitation energy for the compound nucleus ^{142}Dy* to maximise the (p6n) evaporation channel (roughly 113MeV, as estimated with HIVAP [Rei85]). The FMA transmission settings were; recoil energy E=87.9MeV, mass A=135 and charge state Q=25.5, with the focal plane slits positioned to allow transmission of the two near-central charge states 25^+ and 26^+, as shown in Figure 4.4. A 0.825mg/cm^2 Aluminium degrader foil was positioned in front of the DSSD to reduce the implantation energy and depth of the recoils and so avoid overloading the amplifiers. The DSSD was instrumented with the semi-Gaussian shaping amplifiers, and the back silicon veto detector was installed immediately downstream. The ^{147}Tm data

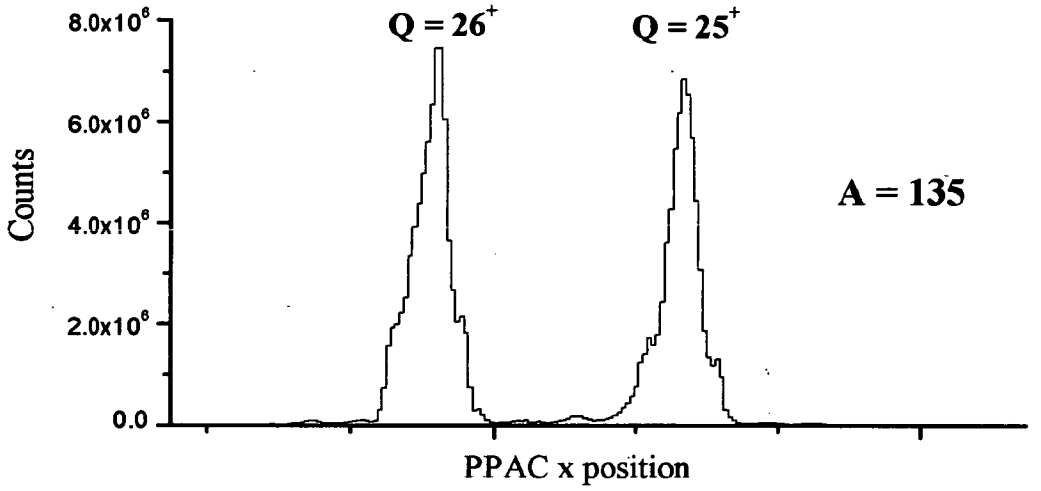

Figure 4.4: *PPAC x position spectrum for the ^{135}Tb experiment.*

from the commissioning run was used to gainmatch and calibrate the DSSD for this experiment.

The energy spectrum of decay events in the DSSD following the implantations of A=135 recoils is shown in Figure 4.5, and a two-dimensional plot of recoil-decay time against decay energy is shown in Figure 4.6. The wide peak around $\sim$ 500keV seen in Figure 4.5 is caused by background from β-decay and escaping β-delayed protons, while the approximately flat background at higher energies is also associated with β-delayed protons. In the bottom part of Figure 4.5, which shows decay events occurring within 6ms of an A=135 implantation event, an obvious peak can be seen at an energy just below 1.2MeV, with negligible background above 700keV. This energy is almost certainly too low to originate from an α-decay event, and is typical of direct proton emission. The A=135 isobars ^{135}Gd and ^{135}Eu are predicted by mass models [Mol97] to be proton-bound, while the even-Z ^{135}Dy,

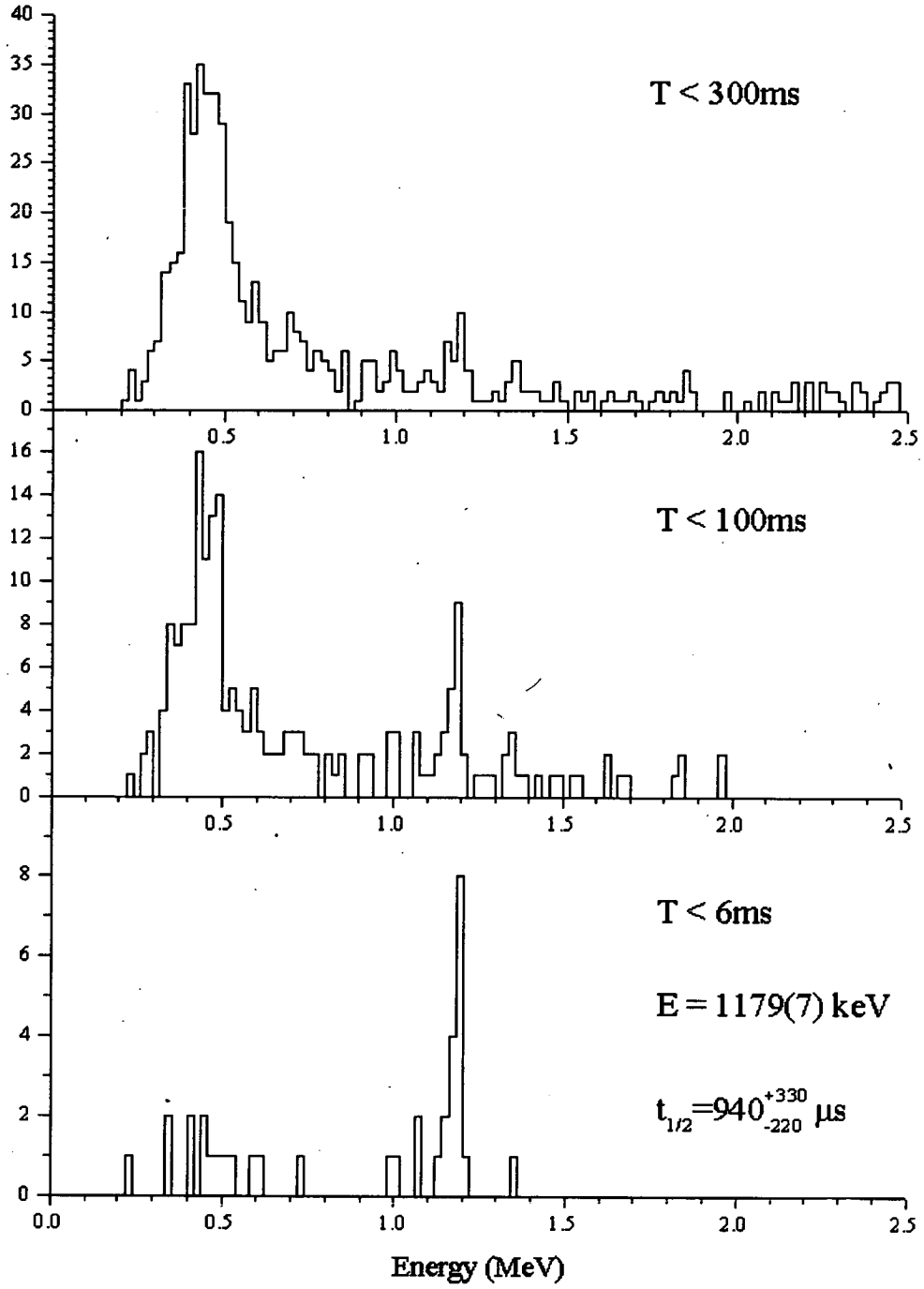

Figure 4.5: *DSSD decay events associated with A=135 recoils from the reaction* $^{50}Cr + {}^{92}Mo$.

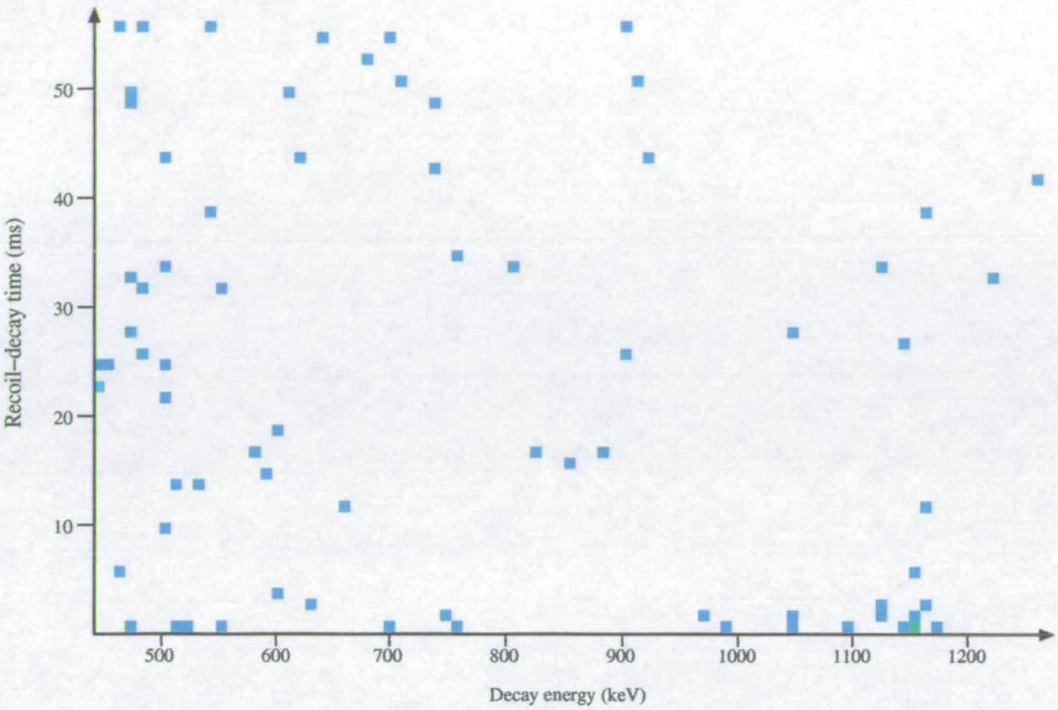

Figure 4.6: *DSSD decay events associated with A=135 recoils from the reaction* $^{50}Cr + ^{92}Mo$ *(blue indicates one count per bin, green indicates five or more counts per bin).*

although predicted to be slightly proton-unbound, would be produced by the extremely low cross-section (7n) evaporation channel, making it a very improbable candidate for the origin of the proton line. Therefore the most likely assignment for the peak is the proton decay of ^{135}Tb, produced by the (p6n) evaporation channel.

After calibration, the energy of the peak was measured to be 1179(7)keV, which gives a Q-value for the proton decay of 1188(7)keV after correction for electron screening, daughter recoil and pulse height deficit. The one-proton separation energy calculations of the macroscopic-microscopic mass model of Möller *et al* [Mol97] predict that the Q-value for the proton decay of ^{135}Tb is

1.15MeV. This particular model also successfully predicts the onset of proton emission for the isotopes of both Europium and Holmium, and demonstrates its usefulness again in this case. The Liran-Zeldes model [Lir76] predicts the one-proton separation energy of ^{135}Tb to be 1.47MeV. The half-life of the peak was calculated to be 940^{+330}_{-220}ms using the maximum likelihood method [Mey75], because there were insufficient counts in the peak to fit an accurate exponential decay curve. The production cross-section for ^{135}Tb from the (p6n) evaporation channel was found to be ~1.5nb, assuming a combined FMA and DSSD efficiency of 8%. This experiment demonstrates the first successful measurement of a (p6n) evaporation reaction product at the proton drip-line. The two examples of proton emitters created using the (p5n) evaporation channel (^{130}Eu [Dav04] and ^{140}Ho [Ryk99]) were produced with cross-sections on the order of 10nb, suggesting a (p6n) cross-section of ~1nb if we consider the approximation of the cross-section decreasing by roughly an order of magnitude with each extra neutron evaporated (as demonstrated in Table 1.1), in agreement with the experimental value. Möller *et al* [Mol97] predict the β-decay half-life of ^{135}Tb to be 193ms, so it is reasonable to assume a 100% proton decay branch for this nuclide.

It is possible that the distribution of counts visible around ~500keV in the lower part of Figure 4.5 contains several events related to protons from the decay of ^{135}Tb escaping through the front of the DSSD and depositing only part of their energy. The recoils are implanted to a depth of ~10-12μm, while the range of a 1MeV proton in silicon is slightly greater than this (~15-20μm). However, from solid angle considerations it is unlikely that >35% of protons would escape through the front of the detector, so this concept cannot explain all of the events in this region (although it probably

accounts for the majority). This explanation is also likely to apply to the two events occuring ~180keV below the main peak, which would imply that the majority of the proton energy was deposited in the detector. A half-life on the order of milliseconds would be quite short for β-decay, making that effect unlikely to be the source of the other low energy counts, so the most likely explanation for these remaining few events is simply the effect of electronic noise (particularly for the two events in this region occurring only a few microseconds after an implantation, an unfeasibly short recoil-decay time).

4.2.3 Discussion of results

If we assume that ^{135}Tb has a spherical shape and perform WKB calculations using the Bechetti-Greenlees optical potential [Bec69] based on the odd proton occupying the $s_{1/2}$, $d_{3/2}$ or $h_{11/2}$ orbitals, then the resulting theoretical proton partial half-lives are 240ns, 2.4μs and 9.5ms respectively, none of which agree with the experimental value. Möller *et al* [Mol95] predict that ^{135}Tb has a significant prolate deformation of β_2 ~0.325, so it is not surprising that the half-life cannot be explained by the simple spherical model. The odd proton is predicted to occupy the $3/2^+[411]$ Nilsson level based on the $2d_{5/2}$ spherical sub-shell, although the $5/2^+[413]$ and $7/2^-[523]$ levels (based on the $1g_{7/2}$ and $1h_{11/2}$ spherical sub-shells respectively) are predicted to be very close to the Fermi surface for the expected deformation. The proton decay rate of ^{135}Tb as a function of the deformation parameter β_2 was therefore calculated using the coupled channels Green's function method of Esbensen and Davids in the adiabatic limit [Esb00] for the likely

proton levels $3/2^+$, $5/2^+$ and $7/2^-$. The results of these calculations are shown in Figure 4.7 and compared with the experimental half-life with error bars (displayed as a horizontal band). The theoretical half-lives have been divided by the spectroscopic factor of $u^2 = 0.57$, which was estimated by a BCS calculation using single-particle level energies similar to that shown for ^{131}Eu in [Esb00]. A value for the proton pairing energy of Δ_p=0.85MeV was used in the calculation, which was obtained from the odd-even mass differences calculated by Möller *et al* [Mol95]. Figure 4.7 clearly shows that the calculated half-life for the $7/2^-$ orbital agrees very nicely with the experimental value at the predicted deformation, whereas the half-lives of the $5/2^+$ and $3/2^+$ orbitals are far too fast (by factors of ~3 and ~15 respectively). On this basis, the proton line can be confidently assigned to the $7/2^-$ orbital in this highly deformed nucleus, which means that the state decays by l_p=3 proton emission to the 0^+ ground state of ^{134}Gd. For the purposes of these calculations, an axially symmetric shape was assumed for ^{135}Tb, in contrast to the postulated slightly triaxial shape of the neighbouring proton emitter ^{141}Ho [Sew01a].

The $7/2^-$ orbital may not be the ground state of ^{135}Tb , as it is in the neighbouring ^{141}Ho. It is possible that this state is an isomer, although if this is the case then the ground state is unlikely to be the $5/2^+$ configuration. In this situation, there would be a fast (i.e. picosecond) E1 gamma transition from $7/2^-$ to the ground state, which would make any proton decay branch trivially small, unless the excitation energy of the $7/2^-$ state was less than 50eV (predicted by Weisskopf estimates), which would be an unusually small energy difference between low-lying states in medium mass nuclei (but this cannot be completely ruled out). The configuration of $3/2^+$ ground state

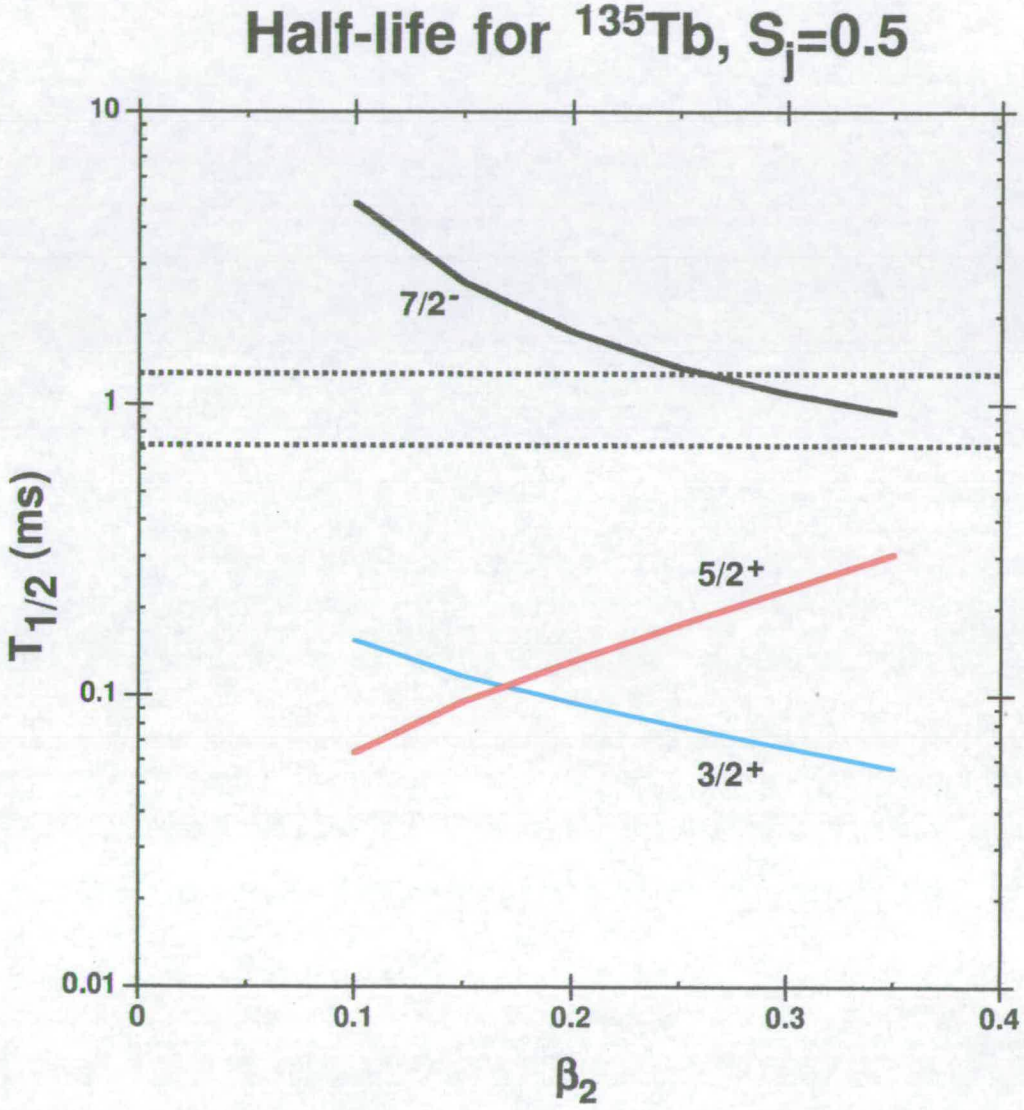

Figure 4.7: *Plot of proton decay half-life against quadrupole deformation β_2 for ^{135}Tb. The horizontal band represents the experimentally measured value (including errors), while the lines show the theoretical calculations for the three likely proton configurations.*

with $7/2^-$ proton-emitting isomer is more likely; the M2 gamma transition could occur on a similar or longer timescale to the proton decay branch with a reasonable $7/2^-$ excitation energy (Weisskopf estimate >2.5ms for excitation energies <50keV) and so would not prevent the observation of proton emission. There are no events in the energy spectrum which would obviously correspond to proton decays from a $3/2^+$ ground state of ^{135}Tb, which would probably have a half-life below 100μs - there are two events which occur ~115keV below the main proton peak, but if this were indeed the excitation energy of the $7/2^-$ state then its gamma transition rate would be an order of magnitude faster than its proton decay rate and so it would be difficult to understand the observation of a $7/2^-$ proton-decaying state. The $3/2^+$ state is in fact the predicted [Mol97] and experimentally measured ground state [Son99] of the neighbouring proton emitter ^{131}Eu. The $7/2^-$ state is the proton-emitting ground state of the nearby ^{141}Ho [Dav98]. The three possible configurations of the proton-emitting $7/2^-$ state are shown in Figure 4.8.

The phenomenon of fine structure has been observed in both ^{131}Eu and ^{141}Ho, and was anticipated as a possibility for ^{135}Tb also. Assuming that the even-even proton daughter nucleus ^{134}Gd has a similar deformation to the parent (β_2 ~0.33), the Grodzins formula [Gro62] predicts the excitation energy of the first excited 2^+ state to be ~120keV. Coupled channels calculations (in the method of [Esb00]) predict a branching ratio of ~8% to a state at this energy. In the bottom part of Figure 4.5, there are two events which correspond to this energy, lying ~115keV below the main proton peak. It is estimated [Fir95] that this state will decay by internal conversion 60% of the time, with half of these electrons being emitted from the K shell (with bind-

ing energy ~30keV) and half from the higher shells (with negligible binding energy). The internal conversion electrons will be detected simultaneously with the proton by the DSSD and their energies summed - therefore we would expect to see roughly 40% of the proton decays to the excited state appearing in a fine structure line ~120keV below the main peak (gamma decay), roughly 30% appearing ~30keV below the main peak (K-shell internal conversion) and another 30% being added back into the main proton peak (higher shell internal conversion), although one must also take into account the fact that the electrons have a much longer range in silicon than the protons and may well escape from the detector, depositing only part of their energy and producing a continuum of events between the main proton peak and the fine structure peak. The statistics gathered in this experiment are simply not sufficient to be able to make a definitive statement regarding the existence of fine structure in ^{135}Tb, although it is likely that the fine structure branching ratio is no greater than about 25% (if one considers the two events lying ~115keV below the main peak as representing 40% of the decays to the excited state), if indeed it exists. To settle the issue, the experiment should be run again (with the higher beam currents now achievable at ATLAS/FMA) to gain better statistics, and the results compared with a Monte Carlo simulation of the fine structure decay process, as performed by Sonzogni *et al* to conclusively establish the presence of fine structure in ^{131}Eu [Son99].

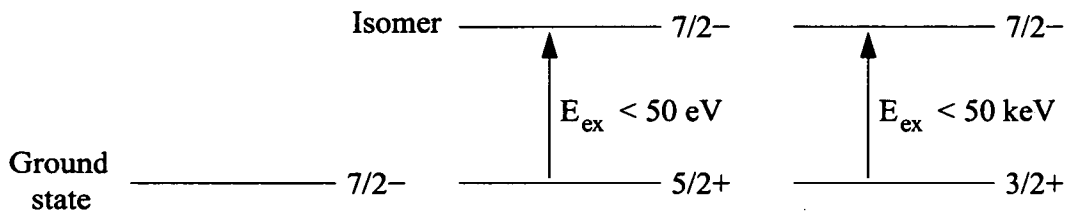

Figure 4.8: *Various possible permutations of the proton-emitting 7/2⁻ state in ^{135}Tb.*

4.3 Search for proton radioactivity of ^{126}Pm

4.3.1 Previous search experiments for proton emission from Pm isotopes

Shortly after the initial discovery of ground state proton radioactivity from ^{147}Tm and ^{151}Lu in 1982, a series of experiments were carried out at the GSI on-line mass separator to search for proton emission from neutron-deficient Prometheum isotopes [Lar83]. Beams of ^{40}Ca from the UNILAC accelerator, with energies 200-240MeV, were used with a 2.1mg/cm^2 ^{92}Mo target to produce the nuclides ^{126,127,128}Pm using the (p5n), (p4n) and (p3n) evaporation channels respectively, with production cross-sections estimated with HIVAP to be 24nb, 910nb and 27μb. The experimental set-up was identical to that described for the ^{136,137,138}Tb search mentioned in the previous section. No evidence for proton-decaying states was found for any of the nuclides, although the predicted proton partial half-life of ^{126}Pm ($<$ 1ms) would be too fast for a mass separator facility to detect. A similar experiment was undertaken [Nit83] at the OASIS on-line isotope separator at Berkeley, utilising a 213MeV ^{40}Ca beam and a 1-2mg/cm^2 ^{92}Mo target to search for ^{127}Pm

via the (p4n) evaporation channel: again, no evidence for proton emission was found. A decade later, the Edinburgh group performed an unsuccessful search for proton emission from ^{128}Pm at the Daresbury recoil mass spectrometer using a DSSD-based setup [Liv93a].

Two more recent experimental searches for proton emission from ^{126}Pm have been reported. In the first experiment at the Argonne FMA [Mah02a], a 432MeV, 3.5pnA, ^{78}Kr beam from ATLAS was used with a 751μg/cm^2 ^{54}Fe target to produce the desired nuclide. No decays faster than 300μs with an energy lower than 2MeV were observed in the DSSD, and a cross-section limit for the production of ^{126}Pm was estimated at 10nb or less. There were concerns that the beam energy was significantly above the optimum value (predicted by HIVAP) for the (p5n) evaporation channel. In the second reported search using a very similar DSSD-based setup at the Recoil Mass Spectrometer at Legnaro [Sor03], a 330MeV ^{58}Ni beam from the ALPI tandem-linac accelerator system was used with an isotopically enriched ^{74}Se target in an initial attempt, but problems with the stability of the target led to another attempt using the inverse kinematic reaction (a 425MeV 0.5pnA ^{74}Se beam on a ^{58}Ni target). This experiment produced no clear proton decay events, and suggested a production cross-section lower than 10nb.

4.3.2 Experimental details and results

After the ^{135}Tb experiment in 2001, the ATLAS-FMA system underwent a series of upgrades, including a new ECR ion source, a new FMA split anode and a new high-rate PPAC at the FMA focal plane, which enabled proton decay experiments to be run at significantly higher beam currents (and there-

fore event rates) than were previously available - see the previous chapter for more information. A search for proton emission from ^{126}Pm was undertaken in 2002 using a 238MeV 24pnA (average) ^{40}Ca beam on a 0.775mg/cm^2 ^{92}Mo target for approximately 42 hours. This beam energy produced a centre-of-target excitation energy for the compound nucleus ^{132}Sm* of 96MeV, the optimum value predicted by HIVAP for the (p5n) evaporation channel. The FMA transmission settings were E=57MeV, Q=23.5 and M=126.5, and the focal plane slits were positioned to transmit the charge states 23^+ and 24^+, as shown in Figure 4.9. For this experiment and the ^{125}Pm search, a new 80×80 DSSD, identical to the first, was installed beyond the focal plane, as the first detector had undergone significant radiation damage since its commissioning. The DSSD was instrumented with both the traditional semi-Gaussian shaping amplifiers and the fast delay-line amplifiers in parallel (see Experimental Method chapter). The back silicon veto detector was installed behind the DSSD as usual, and a Germanium detector was positioned immediately behind the detector mounting to pick up gamma rays associated with decays in the DSSD. Before the main experiment, a calibration reaction producing ^{147}Tm was performed.

The decays that occurred in the DSSD during the ^{126}Pm run with an energy below 2MeV are shown in Figure 4.10 for various recoil-decay time limits. A two-dimensional plot of recoil-decay time against decay energy is shown in Figure 4.11. These spectra were obtained via the shaping amplifiers, as the delay-line amplifiers were found to have an inferior energy resolution (FWHM greater by a factor of 2). Although there are two fast events at an energy of about 1.2MeV shown in the bottom part of Figure 4.10, the spectrum is not completely clean (due to background from β-delayed

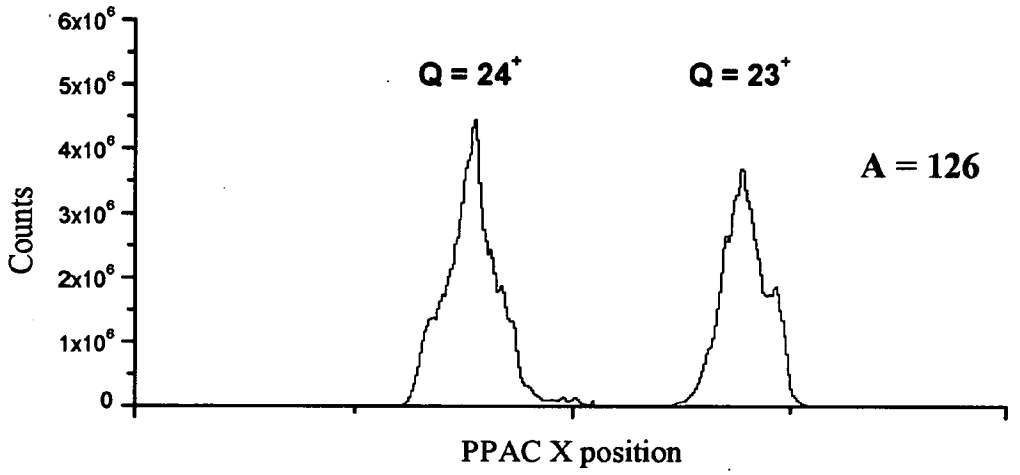

Figure 4.9: *PPAC x position spectrum for the ^{126}Pm experiment.*

protons) and there is no evidence that these events relate to proton radioactivity. A cross-section limit of ~450pb can be placed on ^{126}Pm for proton decay with $t_{1/2}$ <50ms, which represents a search of great sensitivity. This cross-section is based on the level of counts seen in the spectrum around the typical proton energy of 1MeV, the thickness of the target used, the integrated beam current on target of $\sim 2.3 \times 10^{16}$ particles and a combined FMA-DSSD efficiency of around 8%. It was assumed that experimental dead time was not an issue in terms of efficiency due to the relatively low implantation rate.

^{126}Pm is predicted by Möller *et al* [Mol97] to have a S_p of 0.58MeV, which is relatively low compared to nearby proton emitters and would be unlikely to produce a proton decay fast enough to compete with the predicted β-decay partial half-life of 175ms. The Liran-Zeldes model [Lir76] predicts S_p=0.92MeV, which is on a par with the observed S_p values of nearby proton emitters, but this model has been shown to overestimate the S_p values of

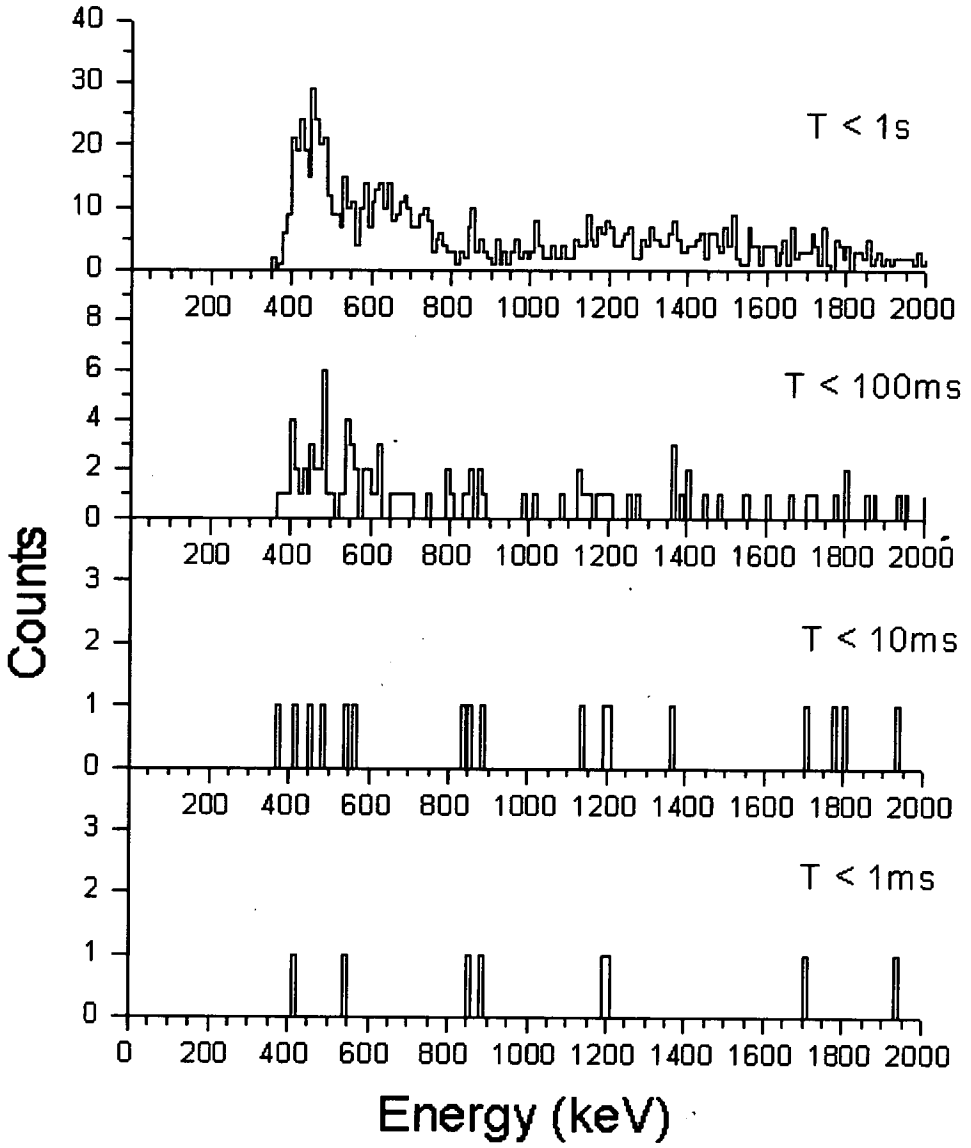

Figure 4.10: *DSSD decay events associated with A=126 recoils from the reaction* $^{40}Ca+^{92}Mo$.

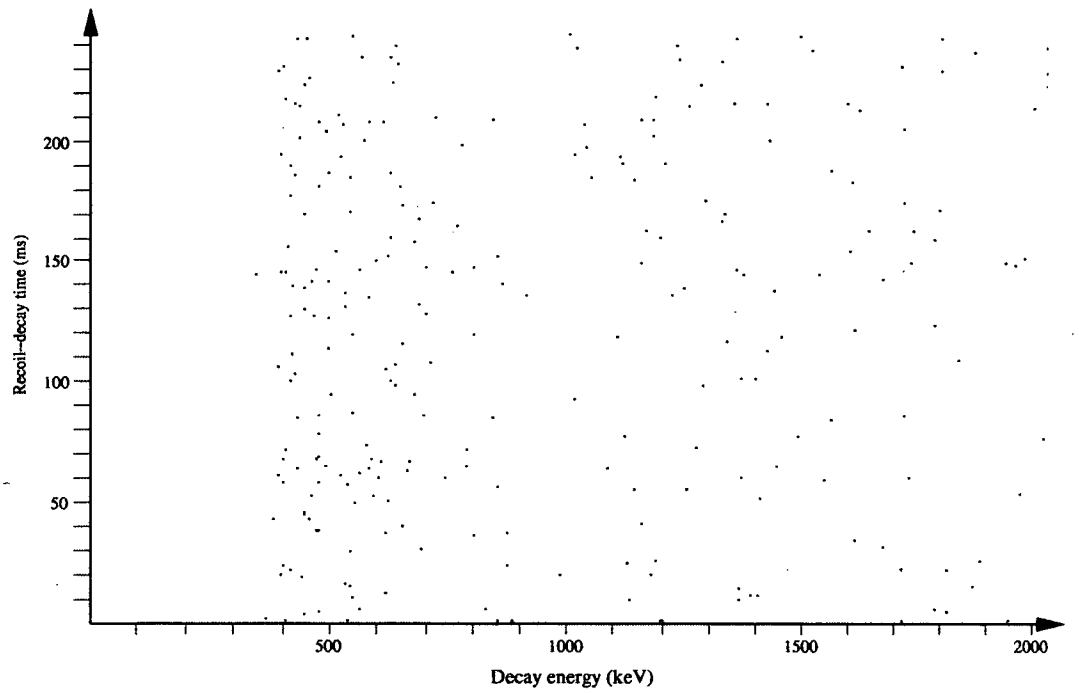

Figure 4.11: *DSSD decay events associated with A=126 recoils from the reaction* $^{50}Cr + {}^{92}Mo$.

proton emitters below Z=69 by typically 200keV (see section 4.5). Thus the non-observation of proton radioactivity from ^{126}Pm is consistent with mass model predictions.

The experiment utilised a $^{40}_{20}$Ca beam from ATLAS, which has previously seen to be contaminated with atmospheric $^{40}_{18}$Ar. As well as requesting the beam operators to regularly check the purity of the beam, the Germanium detector mounted behind the DSSD provided some comfort that nuclides in the expected region (i.e. from the compound nucleus ^{132}Sm* rather than ^{132}Nd*) were being produced. The lower half of Figure 4.12 shows the energy spectrum produced by the Germanium detector during the A=126 run, with tentative assignments for the gamma lines. Although this spectrum is not as simple to interpret as its A=125 counterpart, the 389keV line characteristic of ^{126}Cs (which is not present in the A=125 spectrum) can clearly be seen, along with lines which agree to the β-decay chain ancestors ^{126}Ba, ^{126}La, ^{126}Ce and potentially ^{126}Pr. This last nuclide should produce ^{125}La via β-delayed proton emission, and we do indeed see some lines which agree to the A=125 β-decay chain shown in the top half of Figure 4.12 (although notably not ^{125}Ce or any of its A=124 β-delayed proton descendants). These observations suggest the presence of (α2p) or (αpn) evaporation residues from the ^{132}Sm* compound nucleus produced by the ^{40}Ca beam, rather than the much lower cross-section (p5n) or (α2n) residues from a ^{132}Nd* compound nucleus produced by a ^{40}Ar beam.

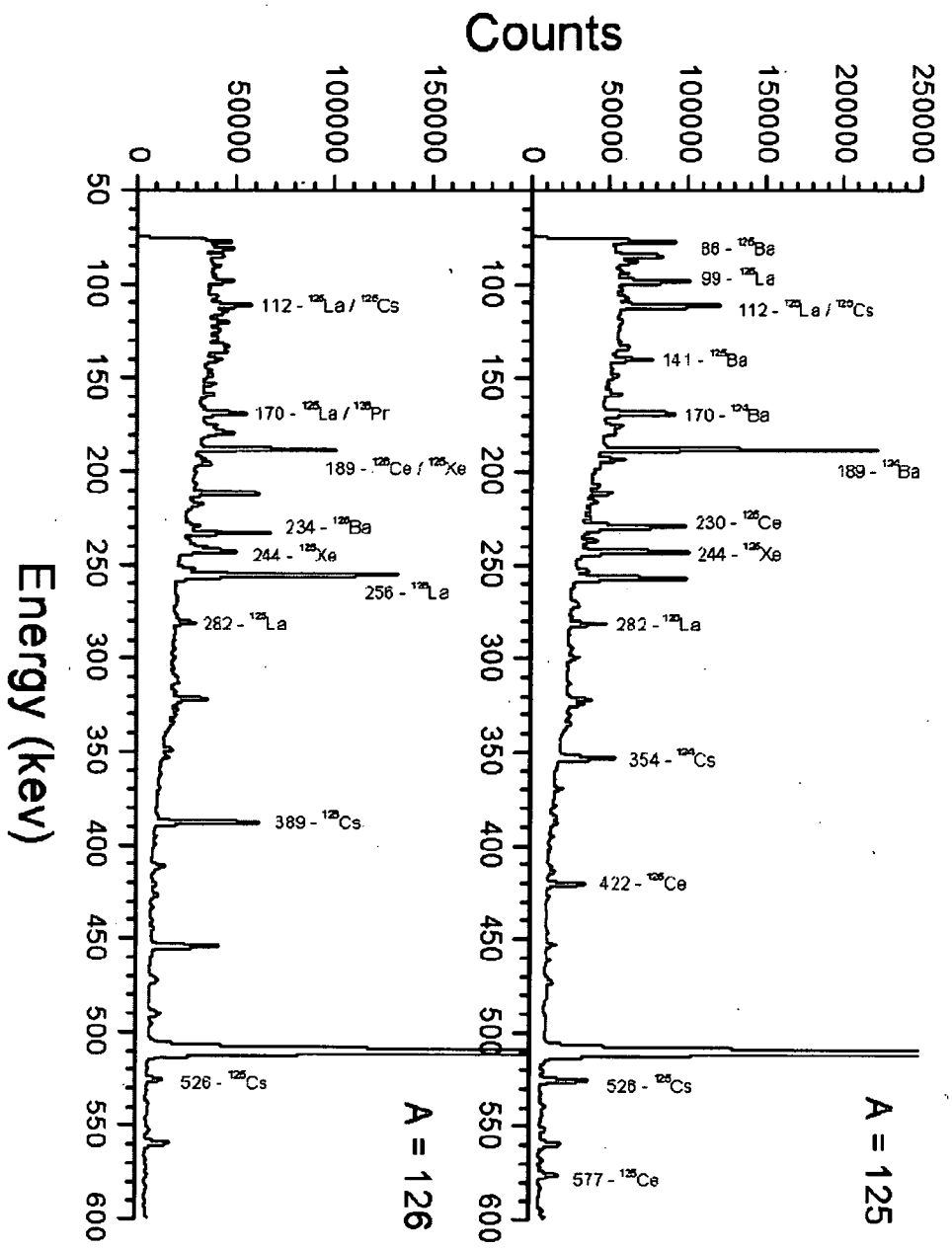

Figure 4.12: *Gamma-ray energy spectra from the Ge detector mounted behind the focal plane, for the A=125 (top) and A=126 (bottom) runs.*

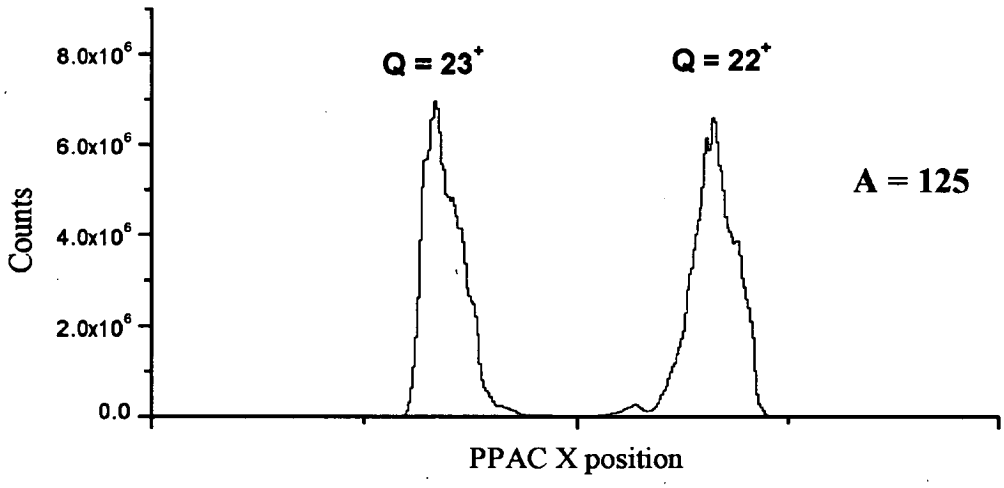

Figure 4.13: *PPAC x position spectrum for the ^{125}Pm experiment.*

4.4 Search for proton radioactivity of ^{125}Pm

An experiment searching for proton decay from ^{125}Pm was performed, the first known attempt. The run took place during the same period as the ^{126}Pm run with the same experimental set-up, lasted roughly 102 hours, and utilised a 260MeV ^{40}Ca beam, with an average current of 22pnA, producing a compound nucleus excitation energy of 108MeV in the centre of the 0.775mg/cm^2 ^{92}Mo target (the optimal excitation energy for the p6n evaporation channel). The FMA was set to transmit recoils of mass 125, energy 62.5MeV and charge state 22.5, with the focal plane slits positioned to allow transmission of the charge states 22^+ and 23^+, as shown in Figure 4.13.

The decays that occurred in the DSSD during the ^{125}Pm run with an energy below 2MeV are shown in Figure 4.14 for various recoil-decay time limits, while Figure 4.15 shows a two-dimensional plot of recoil-decay time

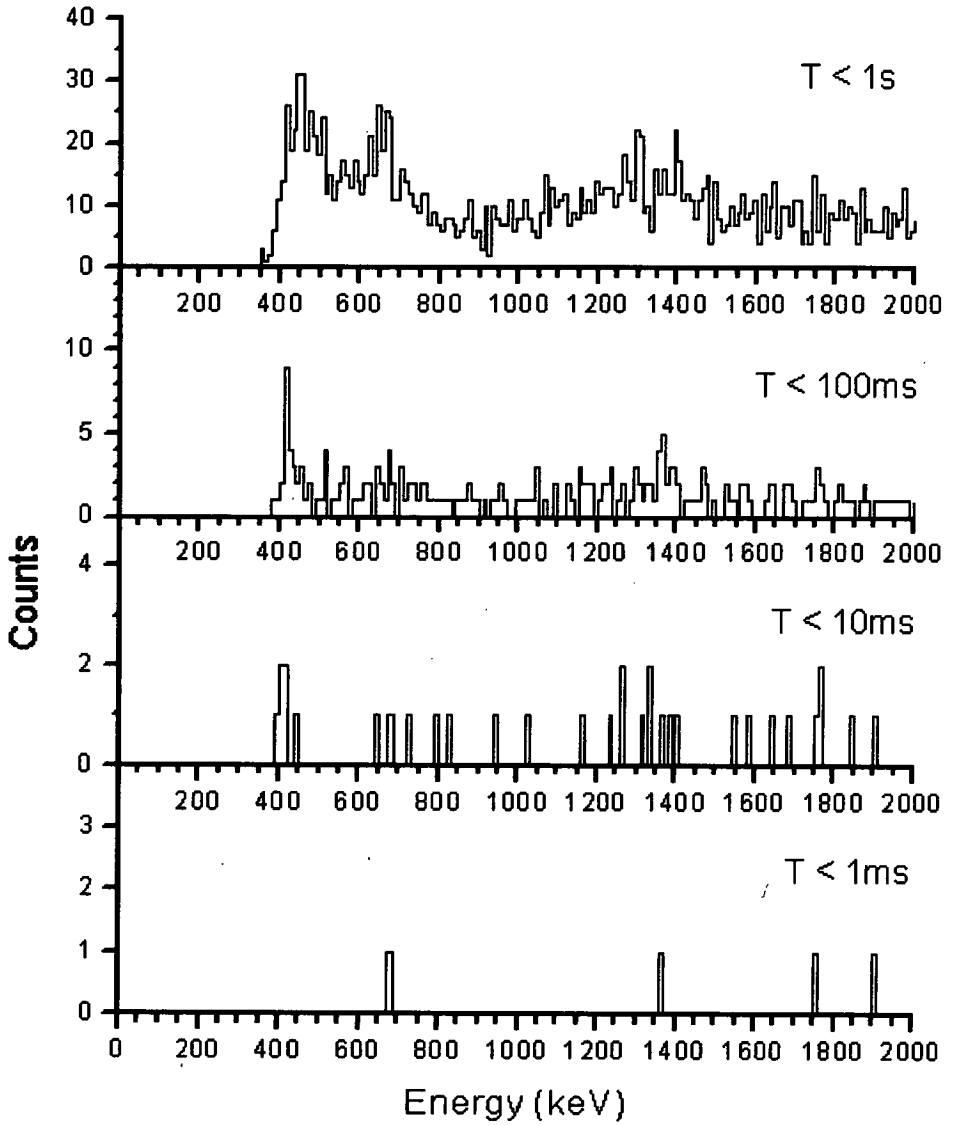

Figure 4.14: *DSSD decay events associated with A=125 recoils from the reaction* $^{40}Ca+^{92}Mo$.

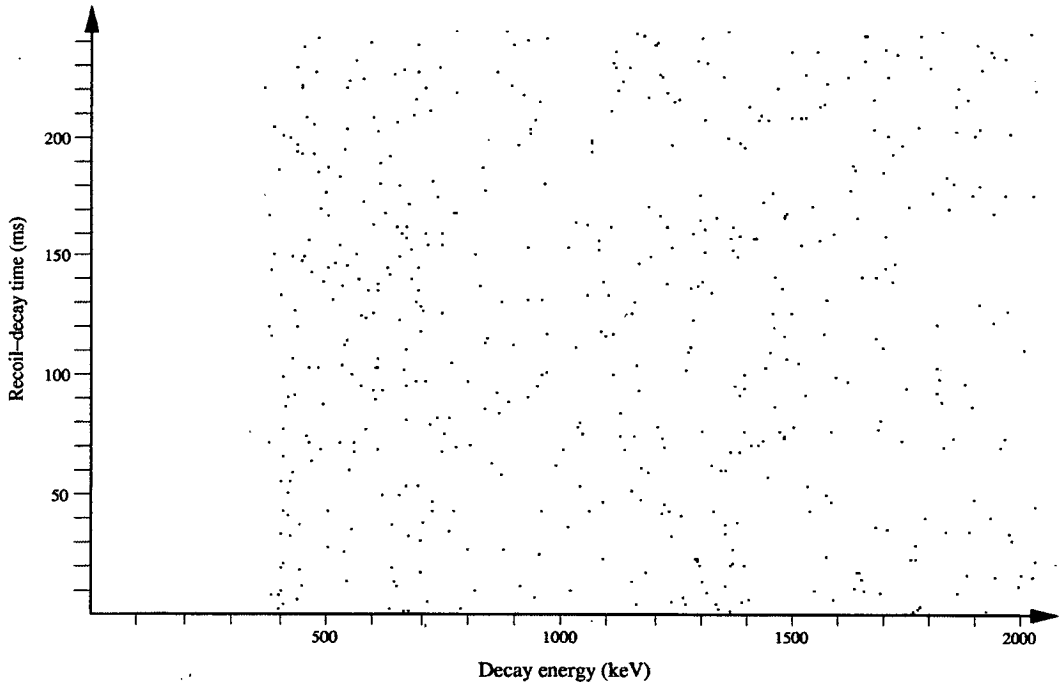

Figure 4.15: *DSSD decay events associated with A=125 recoils from the reaction* $^{50}Cr + {}^{92}Mo$.

against decay energy (again, output from shaping amplifiers rather than delay-line amplifiers were used). Although there is a fast event at an energy of about 1.35MeV shown in the bottom part of the figure, the spectrum is not completely clean (due to background from β-delayed protons) and in fact this event was found to have a recoil-decay time of less than 1μs, so it is impossible that this event could relate to proton radioactivity. The upper two sections of Figure 4.14 hint at potential candidate proton peaks in the region 1.3-1.4MeV, but a long-lived proton decay such as this cannot be cleanly identified as a vertical line (with a decaying exponential time distribution, as demonstrated for ^{135}Tb in Figure 4.6) amidst the background in the two-dimensional plot Figure 4.15. A cross-section limit of ~200pb can be placed on ^{125}Pm for proton decay with $t_{1/2}$ <50ms, based on an integrated beam current on target of $\sim 5.2 \times 10^{16}$ particles, which represents a search of unprecedented sensitivity in proton radioactivity experiments, made possible by the higher beam currents available from ATLAS and the corresponding improvements in the FMA experimental set-up (i.e. split anode, high-rate PPAC and the 80×80 DSSD).

^{125}Pm is predicted by Möller *et al* [Mol97] and Liran and Zeldes [Lir76] to have a S_p of 1.24MeV and 1.45MeV respectively, either of which one would naively expect to lead to a proton decay significantly faster than the predicted β-decay partial half-life of 158ms. Spherical WKB calculations predict $t_{1/2}$ ~50ns for the likely single-particle levels $d_{3/2}$ and $d_{5/2}$, whereas deformed calculations (in the method of Esbensen and Davids described in Chapter 2) suggest $t_{1/2}$ ~120μs for the likely $5/2^-$[532] Nilsson configuration. A proton decay with this predicted energy and half-life should be easily detectable using the FMA-DSSD experimental method, and so the non-observation of

proton emission from ^{125}Pm apparently represents a rare case of the failure of mass model predictions to localise the onset of proton radioactivity in this region. In terms of energetics, two possible explanations present themselves. The proton separation energy may be too large, and thus the decay rate too fast, for the proton decay to be observable (i.e. $t_{1/2} < 1\mu s$), in which case it is possible that Prometheum may be the only odd-Z element between Z=51 and Z=83 which does not have at least one proton-decaying isotope. However, if S_p is indeed too large for ^{125}Pm, it may in fact be lower for its more exotic odd-odd neighbour ^{124}Pm (this effect has been seen in the proton emitting partners ^{112,113}Cs and the highly deformed ^{140,141}Ho, for example). The other explanation for non-observation of ^{125}Pm is that its S_p may be too low, and thus the decay rate too slow, for proton emission to compete effectively with β-decay. It is still possible that ^{124}Pm may have a higher S_p than ^{125}Pm, which is the case for Prometheum's near-neighbours ^{130,131}Eu, and so could potentially exhibit proton decay. However, with current stable beam-target combinations the nuclide ^{124}Pm could only be produced via a (p7n) evaporation channel, which would probably be too weak to be detectable with this experimental technique, even with the recent upgrades in the ATLAS-FMA system. It is also possible that the centrifugal barrier helping to contain the odd proton in ^{125}Pm is unusually low, due to the proton having a lower l_p value than expected, which could cause the decay to occur too quickly for observation. This could be the case if the proton occupied the $1/2^+[420]$ Nilsson level (based on the $d_{5/2}$ spherical sub-shell), allowing s-wave proton emission, although this state is not expected to be close to the Fermi surface at the expected deformation, therefore this explanation seems unlikely. Of course, a final possibility is that ^{125}Pm does exhibit proton radioactivity

but the production cross-section for this particular (p6n) fusion-evaporation reaction is below ~200pb. Experimental measurements of production cross-sections of proton emitters have shown that nuclides produced via a (p5n) evaporation channel (e.g. ^{140}Ho, ^{130}Eu and ^{164}Ir) have cross sections in the range ~10-15nb, while (p4n) evaporation residues (e.g. ^{145}Tm, ^{141}Eu, ^{131}Eu and ^{117}La) exhibit cross-sections over a wide range from ~100nb to ~500nb. Given the measured (p6n) production cross-section for ^{135}Tb of ~1.5nb, it is not unreasonable that the (p6n) cross-section for ^{125}Pm could be a factor of 7-8 lower, given the factor of 5 variation in the (p4n) cross-sections. To settle the issue, the experiment should be repeated with a similarly high beam current (20-25pnA) and over a longer period, for example 200 hours, which would probe production cross-sections of 100pb or lower.

Again, the Germanium detector mounted behind the DSSD provided some comfort that ATLAS was producing a ^{40}Ca (rather than ^{40}Ar) beam. The top half of Figure 4.12 shows the gamma decay spectrum during the A=125 run, with tentative assignments for gamma lines. Lines consistent with the β-decay of the nuclides ^{125}Ce, ^{125}La, ^{125}Ba, ^{125}Cs and ^{125}Xe can be identified, along with the A=124 nuclides ^{124}Ba and ^{124}Cs, which are produced by β-delayed proton emission from ^{125}Ce. There is no clear evidence for gammas produced by the β-decay of ^{125}Pr [Pau98], which suggests that ^{125}Ce is being produced via the (α2pn) evaporation channel from the ^{132}Sm* compound nucleus produced by the ^{40}Ca beam, rather than the much lower cross-section (α3n) residues from a ^{132}Nd* compound nucleus produced by an ^{40}Ar beam.

4.5 Comparison with mass model predictions

The complete set of data on ground-state proton decay energies in the range $51 \leq Z \leq 83$ (for odd Z) was used to test the accuracy of the one-proton separation energy predictions of the two mass models described in section 2.5. It should be noted that nuclides for which proton emission has been observed from an isomer but not the ground state (i.e. ^{164m}Ir and ^{185m}Bi) have been included in the comparison, assuming that the excitation energy of the isomer is small relative to the proton separation energy of the nucleus. Similarly, ^{135}Tb has been included in the comparison, although it has not yet been established whether the proton decay proceeds from the ground state or a possible isomer, as discussed in section 4.2. The proton emitters ^{121}Pr and ^{144}Tm, which were discovered after the experiments discussed in this chapter took place (see Chapter 5 for further information), are also included in the comparison.

The comparison is extended by the inclusion of known proton separation energies of other proton-unbound nuclides (which are not sufficiently unbound to exhibit proton radioactivity). These values were taken from the most recent Atomic Mass Evaluation (AME) [Aud03], and only include those nuclides with masses derived from experimental reaction/decay measurements (rather than systematic trends). It should be noted that most of these AME S_p values were derived using experimental data on α decays measured by Edinburgh group collaborations using the mass separator-DSSD technique that has proved so fruitful in the study of proton decay (see [Pag96], [Dav97] and [Pol99] for examples).

Only one of the proton separation energy values used in this compari-

son, that of ^{189}Bi, has been surveyed by direct mass measurement techniques (as opposed to indirect methods such as the study of decays). This was achieved by Schottky mass spectrometry at the Experimental Storage Ring at GSI [Nov02, Lit05], and yielded a result of S_p=-370(110)keV, in agreement with the AME value of -470(50)keV which was derived from indirect methods. This mass measurement technique is currently limited to the study of nuclides with half-lives on the order of several hundreds of milliseconds or longer, and is therefore of limited use in further exploring the mass surface in this region of odd-Z proton-unbound nuclei. However, the ISOLTRAP Penning trap facility at CERN-ISOLDE has been shown to provide accurate mass measurements for nuclides with half-lives as short as ~70ms, so this alternative method may provide more useful mass data in this region in the future (see [Bec00] and [Lun03] for more information on this technique).

Figures 4.16 and 4.17 show the predictions of the Möller-Nix and Liran-Zeldes models compared to the experimentally-derived S_p values.

It was found that the Liran-Zeldes model produces better overall Q_p predictions than the model of Möller *et al* for this extremely neutron-deficient region, with mean and RMS deviations of -46keV and 211keV respectively, compared to -230keV and 430keV respectively for the latter model. It was observed that the Liran-Zeldes model Q_p predictions tend to be too high for the lighter (Z<69) proton emitters, thus underbinding them, while the heavier examples are overbound (with the exception of the Thallium and Bismuth isotopes). The Möller-Nix model was seen to generally overbind the nuclides over the whole mass region considered (again, with the notable exception of the Bismuth isotopes), hence the larger mean deviation. To put these deviation values in perspective, it is useful to note that the RMS

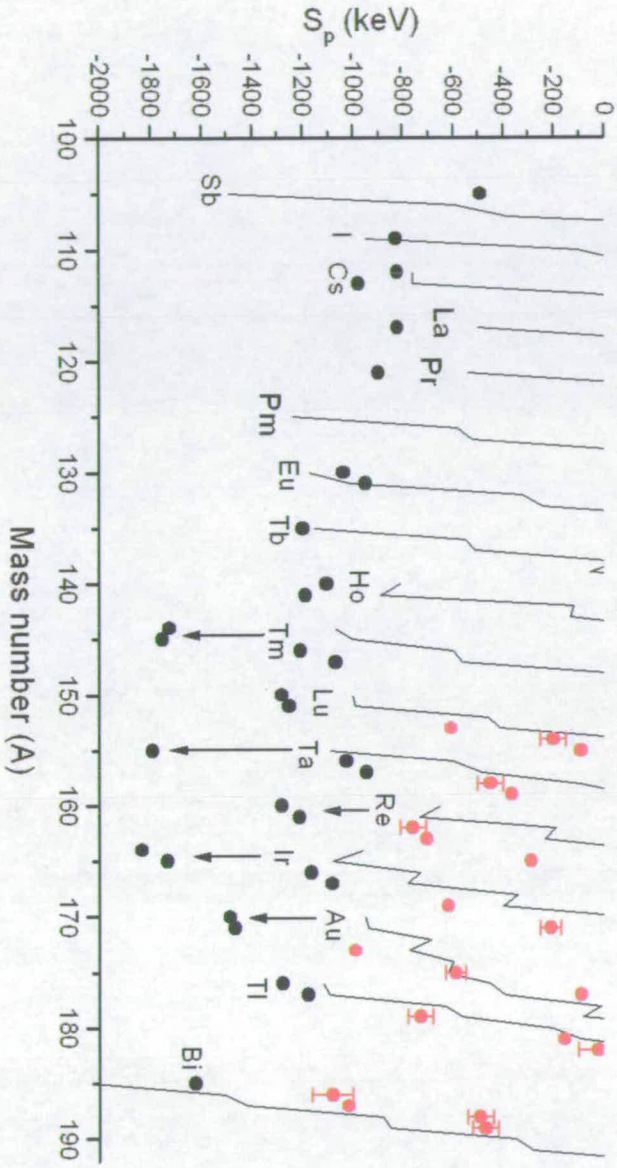

Figure 4.16: *Proton separation energy predictions of the Möller-Nix mass model compared to experimentally-measured proton decay Q-values (black circles) and proton separation energies derived from indirect experimental mass measurements (red circles, with error bars shown where they exceed the size of the data point).*

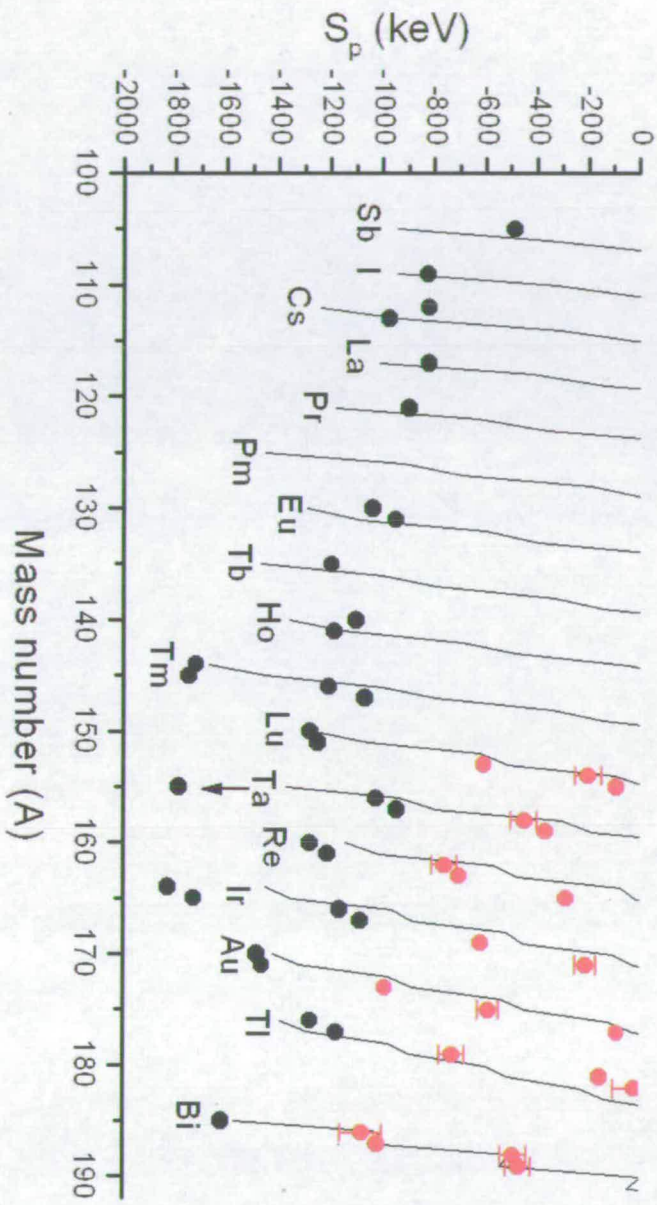

Figure 4.17: *Proton separation energy predictions of the Liran-Zeldes mass model compared to experimentally-measured proton decay Q-values (black circles) and proton separation energies derived from indirect experimental mass measurements (red circles, with error bars shown where they exceed the size of the data point).*

deviations of these two models when compared to the 2135 nuclei of an interim atomic mass compilation were found to be 586keV for Liran-Zeldes and 676keV for Möller-Nix [Lun03], which demonstrates that both models are relatively successful in this particular region.

The Liran-Zeldes model is significantly older than the macroscopic-microscopic model, although it does contain 178 independent parameters which are determined by least-squares fitting from the data of 1818 nuclides, while the Möller-Nix model contains 38 parameters, only 16 of which are evaluated by least-squares fitting to measured mass data of 1654 nuclides. Thus it is not surprising that the model with the largest parameter space and the largest data set fares best, although it is remarkable that either model comes so close to calculating the masses of such exotic nuclei, bearing in mind that these predictions are extrapolated many neutrons further from stability than the nuclides used in the model data sets. The accuracy of the Liran-Zeldes predictions for the Bismuth isotopes $^{185-189}$Bi is particularly notable, as can be seen in Figure 4.17, with an RMS deviation of only 55keV (compared to 205keV for the nuclides in the range 71<Z<81), which would probably be reduced even further if the excitation energy of the isomeric proton emitter ^{185m}Bi were known and subtracted. The success of the Bismuth predictions may be due to the proximity of the Z=82 shell closure; the predictions for the Lutetium isotopes have a relatively low RMS deviation of 129keV, which may be due to the presence of the N=82 shell closure. It has also been demonstrated that the Liran-Zeldes predictions for Q_α in the region below the Z=82 shell closure are far superior to those of the Möller-Nix model [Sew99].

Although the predictions of the Möller-Nix model in terms of absolute

Table 4.1: *Comparison of spin-parity predictions of the Möller-Nix model for deformed lanthanide proton emitters with values derived from the theoretical analysis of the experimentally-measured half-lives (assuming deformations close to those predicted by Möller-Nix). It should be noted that the spin-parity assignment for ^{131}Eu has been confirmed independently by analysis of the fine structure branching ratio [Son99].*

Nucleus	Möller-Nix Ω^π	Ω^π from $t_{1/2}$
^{117}La	$3/2^+$	$3/2^+$ or $3/2^-$
^{121}Pr	$3/2^-$	$3/2^+$ or $3/2^-$
^{131}Eu	$3/2^+$	$3/2^+$
^{135}Tb	$3/2^+$	$7/2^-$
^{141}Ho	$7/2^-$	$7/2^-$

values may be inferior, it can be seen to predict the onset of proton emission at the correct mass number for many isotopes by a large sudden increase in Q_p; for example, predicted Q_p increases by 0.7MeV between ^{132}Eu and ^{131}Eu, by 0.6MeV between ^{136}Tb and ^{135}Tb, and by 0.8MeV between ^{142}Ho and ^{141}Ho. The Liran-Zeldes model Q_p tends to increase more smoothly, with increments of 0.45MeV for the onset of proton emission in Eu, Tb and Ho. It can be seen from the figures that the effect of odd-even staggering is much more pronounced in the Möller-Nix predictions than their Liran-Zeldes counterparts, with the exception of Bismuth. This staggering includes the accurate prediction that the Q_p values of the odd-odd proton emitters ^{112}Cs and ^{140}Ho are less than their odd-even neighbours ^{113}Cs and ^{141}Ho, which is not the case in the Liran-Zeldes predictions. The Möller-Nix model also provides predictions regarding β decay (Q_β and half-life) and the spin and parity of the odd particle (as shown in Table 4.1), which were found to be accurate for ^{131}Eu and ^{141}Ho, but not ^{135}Tb (although the density of Nilsson levels in this region is likely to be finer than the precision of the model,

so this one failure is certainly not significant). The Möller-Nix model also predicts the ground-state deformation of the nucleus, and has been shown to be in excellent agreement with experimentally-derived shape information in this region. The presence of prolate deformation in the neutron-deficient lanthanide region has been demonstrated directly by the observation of rotational bands in proton emitters (e.g. in ^{141}Ho [Sew01a]), as well as indirectly by the reduced energy of the first excited state of even-even proton-decay daughter nuclei which allows fine structure branching (e.g. in ^{131}Eu [Son99]). Deformation is also implied by the failure of spherical proton decay models to reproduce the measured decay rates, and is also indicated by other experimental methods (e.g. the study of β-delayed proton emission [Xu05]).

Chapter 5

Conclusions

5.1 Summary

Searches for new examples of proton radioactivity from highly deformed lanthanide nuclei were conducted at the FMA at Argonne National Laboratory in 2001 and 2002, utilising a new purpose-built double-sided silicon strip detector (DSSD) system.

The properties of the detector (in terms of energy resolution and strip multiplicity) were found to be acceptable for such studies during a brief commissioning run, and shortly after this the new proton emitter ^{135}Tb was observed with a proton energy of 1.18MeV. This highly exotic nuclide was produced using heavy ion fusion-evaporation reactions via the (p6n) evaporation channel, the first such use of this extremely low cross-section channel, which illustrates the improved sensitivity of the FMA-DSSD technique (made possible by an increase in available beam current and the new detector). The experimental proton decay rate was compared to calculations

made by C.N. Davids, using the coupled channels method as described in [Esb00], and was found to be consistent with the large prolate deformation predicted for this isotope (due to its remoteness from closed shells for both protons and neutrons), specifically a deformation of β_2 >0.3, with the odd proton occuping a $7/2^-$ Nilsson state. It is not clear whether this proton-decaying state is the ground state of ^{135}Tb, or a low-lying isomeric state. It is also possible that this proton emitter exhibits fine structure, as is the case with its near-neighbours ^{131}Eu and ^{141}Ho, although another experiment with improved statistics is required to confirm this hypothesis. Figure 5.1 compares the decays of these three highly-deformed lanthanide odd-even proton emitters.

Experimental searches for proton emission from the nuclides ^{125,126}Pm were carried out the following year, 2002. The production reactions utilised the (p6n) and (p5n) evaporation channels respectively, and further upgrades to the experimental system (i.e. a split anode and new PPAC) allowed the experiments to be run with twice the beam current of the ^{135}Tb experiment, and thus to be more sensitive in terms of probing low production cross-sections. No evidence was found for proton radioactivity from either of these nuclides: this was not entirely surprising in the case of ^{126}Pm, as mass models predict that the proton separation energy for this isotope is unlikely to be sufficiently large for proton emission to compete effectively with β-decay. The non-observation of the proton decay of ^{125}Pm can be explained in four ways. Firstly, the proton separation energy is too large (and thus the decay process too fast) for proton emission to be observable in this experimental method. Secondly, the proton separation energy may still be too low for proton emission to compete with β-decay, despite this nuclide being further

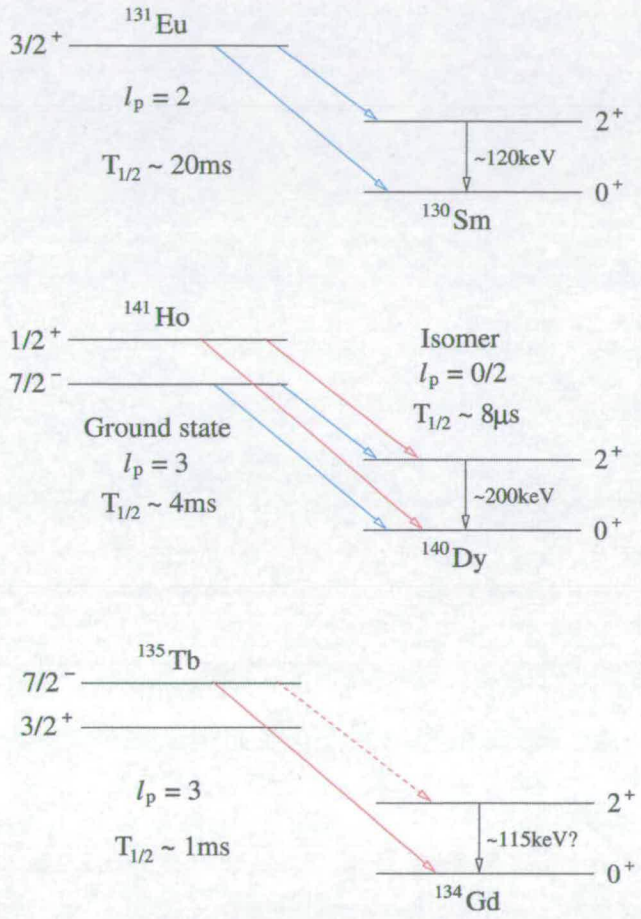

Figure 5.1: *Proton decay schemes of* ^{131}*Eu,* ^{141}*Ho and* ^{135}*Tb.*

from stability (and thus probably having a larger proton separation energy) than ^{126}Pm. Thirdly, the odd proton has a lower than expected angular momentum which reduces the height of the centrifugal barrier and allows the decay to proceed too quickly for observation. Finally, ^{125}Pm may in fact decay by proton emission on an observable timescale, but the production cross-section may be too low for the decay to have been observed in the experiment. It would be unusual if Prometheum had no observable proton-emitting isotopes at all, as at least one has been found for every odd-Z element in the range $51 \leq Z \leq 83$ (see next section), so it is important that the search for proton emission from ^{125}Pm is repeated with improved statistics in order to settle this important question. It is possible that, with yet further improvements in the sensitivity of the system, the even more exotic ^{124}Pm could be investigated in the future.

A comparison of experimentally determined proton separation energies and those predicted by mass models (specifically those models of Möller *et al* [Mol95, Mol97] and Liran & Zeldes [Lir76]) was carried out. It was found that the older Liran-Zeldes model produces results closer to experimental S_p values than the newer model of Möller *et al* (with RMS deviations of 216keV and 438keV respectively), although it should be noted that the former model contains a much larger parameter space than the latter (178 parameters in the former, 38 in the latter).

5.2 Future progress

After the experiments described in this thesis were performed, a major development in the field of proton emission from highly deformed nuclei was

the discovery of the proton radioactivity of ^{121}Pr [Rob05a], again utilising the FMA-DSSD system at Argonne. This nuclide was again produced via a (p6n) evaporation reaction, with a production cross-section comparable to that probed in the search for ^{125}Pm. The proton-decaying state was identified as either $3/2^+$ or $3/2^-$ by comparison of experimental and theoretical half-lives, and the measured half-life of ~10ms was shown to be far too fast to agree with the postulated observation of ^{121}Pr proton radioactivity by the Dubna group in the 1970s. This proton emitter was included in the mass model comparison in the previous chapter, with Q_p of 0.9MeV. The discovery of this proton emitter leaves Prometheum as the only element in the range $51 \leq Z \leq 83$ which does not have a single observable proton-emitting isotope, which emphasises the importance of further investigation of the neutron-deficient Pm isotopes. Another proton emitter, ^{144}Tm, has also been recently discovered by the Oak Ridge group [Grz05] via a (p5n) evaporation reaction with production cross-section of ~10nb (which is consistent with other examples of this evaporation channel). Two proton lines were reported, at energies of 1.70MeV and 1.43MeV, although the interpretation of these lines in terms of the structure of the nucleus is complicated by its odd-odd nature, as is the case with ^{146}Tm. For the purposes of the mass model comparison in the previous chapter, it was assumed that Q_p for ^{144}Tm is 1.7MeV.

The programme of upgrades to the FMA-DSSD detection technique includes; an upgraded ion source producing higher beam currents, a split anode in the first electric dipole of the FMA which drastically reduces the number of scattered beam particles reaching the focal plane, a new position-sensitive focal plane detector (the PPAC) with a much higher rate limit,

the new large area (and fine granularity) DSSD which is large enough to cover the full FMA image and was used for the first time in the experiments described in this thesis, and the delay-line amplifiers which now instrument the DSSD and allow accurate measurement of decay energies within $\sim 1\mu$s of an implantation. These improvements allow the experimenter to search for proton decay candidates with extremely low production cross-sections ($<$ 500 picobarns with $\sim$50 hours of beam time) and to detect decays with half-lives on the order of a few microseconds. For example, this could allow the detection of proton radioactivity from more exotic nuclides in the region of predicted high deformation such as ^{129}Eu and ^{116}La, which may possibly have Q_p values which lead to proton decays on an observable timescale (predicted $\sim$1.8MeV and $\sim$0.7-1.3MeV respectively), produced by (p6n) and (p5n) evaporation channels respectively. A cross-section limit of $\sim$5nb has already been placed on the decay of ^{116}La in a previous experiment at the FMA [Mah02a], which occurred prior to the installation of the delay-line amplifiers and thus was not sensitive to decays on the order of a few microseconds. It is possible that proton decay candidates produced via (p7n) evaporation channels could be probed in the future: for example, ^{134}Tb is predicted to have a Q_p value only slightly larger than ^{135}Tb (1.28MeV compared to 1.15MeV according to the Möller-Nix model), and so the decay could be slow enough to be detected if the nucleus could be produced in sufficient quantities. It is also possible that the improved experimental set-up could be used to search for ground-state proton decay candidates below Z=50, although it is likely that if proton emitters exist in this region then they should have already been identified in fragmentation reactions which have mapped the proton drip-line.

A repetition of the ^{135}Tb experiment with higher statistics would be very beneficial in terms of confirming or ruling out the presence of fine structure in the proton decay of this nucleus. Fine structure has already been observed in the neighbouring proton emitters ^{131}Eu and ^{141}Ho, and its presence in the decay of ^{135}Tb would provide another way of identifying the spin and parity of the decaying state (in addition to the comparison of experimental and theoretical half-lives), as well as measuring the energy of the first excited state in ^{134}Gd.

The main focus of proton radioactivity studies at the FMA in recent years has been the investigation of odd-odd nuclei to study the effect of the residual interaction between the odd proton and the odd neutron. Specifically, ^{146}Tm [Rob05b] and ^{150}Lu [Rob03] have been reinvestigated with much improved statistics compared to previous experiments. Proton emission from odd-odd nuclei is influenced by the level schemes of both parent and daughter, which may be complex due to the coupling of the odd proton and neutron, and so highly accurate measurements of the proton energy and particularly the decay half-life are essential to perform meaningful comparisons with theory and so piece together the decay schemes.

After the experiments described in this thesis, the Gammasphere detector was installed around the target chamber at the FMA. This allows the detection of gamma-rays from the fusion-evaporation recoils shortly after they are created, which can then be 'tagged' by correlating them with measured particle decay events when the recoils reach the DSSD (the so-called recoil-decay tagging, or RDT, method). This technique has previously been used to identify rotational bands in the gamma-ray spectra of ^{141}Ho [Sew01a] and ^{131}Eu [Sew01b], which acts as independent and direct confirmation of

the deformation of these nuclei (in addition to the comparison of experimental and theoretical half-lives). The RDT technique has since been used to identify rotational bands in ^{145}Tm and ^{146}Tm [Sew05].

The search for proton emitters heavier than ^{185}Bi could be facilitated by the use of gas-filled separators such as RITU, or by the use of fragmentation reactions using a ^{238}U beam [Liu04]. Fragmentation reactions were recently used to discover the second example of two-proton emission, ^{54}Zn [Bla05], at the GANIL facility, which now allows meaningful comparisons with theory for this highly exotic decay mode. A single candidate event for the two-proton decay of ^{48}Ni has also been recently reported [Dos05].

The other important recent development in the field of proton radioactivity was the discovery of direct proton emission from a 21^+ isomer in ^{94}Ag (which is proton-bound in its ground state) at the GSI on-line mass separator [Muk05]. There is preliminary evidence that this isomer also exhibits two-proton decay, as well as β-delayed proton and two-proton emission, making it a truly unique state. This discovery also represents only the second example of one-proton emission below Z=50, the other being the very first proton emitter to be discovered, ^{53m}Co, 35 years previously.

In conclusion, the study of proton radioactivity in highly-deformed neutron-deficient nuclei provides unique information on nuclear structure beyond the proton drip-line, demonstrates the effect of deformation on the tunneling process, inspires progress in theoretical proton decay models, and also provides data for comparison with (and the future improvement of) mass models. The investigation of proton emission from nuclei remains a vital and interesting branch of nuclear physics.

Bibliography

[Åbe97] S. Åberg, P. B. Semmes and W. Nazarewicz, Phys. Rev. C **56**, 1762 (1997).

[Aro86] J. Aron *et al*, Rev. Sci. Inst. **57**(5), 737 (1986).

[Aud03] G. Audi, A. H. Wapstra and C. Thibault, Nucl. Phys. A **729**, 337 (2003).

[Bat98] J. C. Batchelder *et al*, Phys. Rev. C **57**, R1042 (1998).

[Bec69] F. D. Becchetti, Jr. and G. W. Greenlees, Phys. Rev. **182**, 1190 (1969).

[Bec00] D. Beck *et al*, Eur. Phys. J. A **8**, 307 (2000).

[Ben85] T. Bengtsson and I. Ragnarsson, Nucl. Phys. A **436**, 14 (1985).

[Bla05] B. Blank *et al*, Phys. Rev. Lett. **94**, 232501 (2005).

[Blu96] D. J. Blumenthal, http://www.phys.anl.gov/fma/fmarecoil_form.html (1996).

[Boh69] A. Bohr and B. R. Mottelson, *Nuclear Structure*, Vol. 1, McGraw-Hill (1969).

[Bol93] L. M. Bollinger *et al*, Nucl. Instr. Methods A **328**, 221 (1993).

[Bug85] V. P. Bugrov *et al*, Sov. J. Nucl. Phys. **41**, 717 (1985).

[Bug89] V. P. Bugrov and S. G. Kadmensky, Sov. J. Nucl. Phys. **49**, 967 (1989).

[Cer70] J. Cerny *et al*, Phys. Lett. B **33**, 284 (1970).

[Dav89] C. N. Davids and J. D. Larson, Nucl. Instr. Methods B **40/41**, 1224 (1989).

[Dav92] C. N. Davids *et al*, Nucl. Instr. Methods B **70**, 358 (1992).

[Dav94] C. N. Davids, Nucl. Instr. Methods A **345**(3), 528 (1994).

[Dav96] C. N. Davids *et al*, Phys. Rev. Lett. **76**, 592 (1996).

[Dav97] C. N. Davids *et al*, Phys. Rev. C **55**, 2255 (1997).

[Dav98] C. N. Davids *et al*, Phys. Rev. Lett. **80**, 1849 (1998).

[Dav00a] C. N. Davids and H. Esbensen, Phys. Rev. C **61**, 054302 (2000).

[Dav00b] C. N. Davids, *Proc. 1st Int. Symposium on Proton-Emitting Nuclei*, ed. J. C. Batchelder, American Institute of Physics, 200 (2000).

[Dav02] C. N. Davids, Argonne Annual Report 2002, 104 (2002).

[Dav04] C. N. Davids *et. al.*, Phys. Rev. C **69**, 011302(R) (2004).

[Dos05] C. Dossat *et al*, Phys. Rev. C **72**, 054315 (2005).

[Esb00] H. Esbensen and C. N. Davids, Phys. Rev. C **63**, 014315 (2000).

[Fae84] T. Faestermann *et al*, Phys. Lett. B **137**, 23 (1984).

[Fes92] H. Fesbach, *Theoretical Nuclear Physics: Nuclear Reactions*, John Wiley and Sons Inc., New York (1992).

[Fir95] R. B. Firestone, *Table of Isotopes 8th edition*, John Wiley and Sons Inc., New York (1995).

[Gam28] G. Z. Gamow, Phys. **51**, 204 (1928).

[Gil87] A. Gillitzer *et al*, Zeitschrift für Physik A **326**, 107 (1987).

[Gin03] T. N. Ginter *et al*, Phys. Rev. C **68**, 034330 (2003).

[Gio02] J. Giovinazzo *et al*, Phys. Rev. Lett. **89** 102501 (2002).

[Gro62] L. Grodzins, Phys. Lett. **2**, 88 (1962).

[Grz05] R. Grzywacz *et al*, Eur. Phys. J. A **25**, 145 (2005).

[Hax49] O.Haxel, J. H. D. Jensen and H. E. Suess, Phys. Rev **75**, 1766 (1949).

[Hof81] S. Hofmann *et al*, Zeitschrift für Physik A **299**, 281 (1981).

[Hof82a] S. Hofmann *et al*, Zeitschrift für Physik A **305**, 111 (1982).

[Hof82b] S. Hofmann *et al*, GSI Sci. Rep. 1981 **GSI 81-1**, 241 (1982).

[Hof89] S. Hofmann, in *Particle Emission from Nuclei* Vol. **2**, eds. D. N. Poenaru and M. S. Ivascu, CRC Press Inc., Florida (1989).

[Hua76] K. N. Huang and H. Mark, At. Data Nucl. Data Tables **18**, 243 (1976).

[Jac70] K. P. Jackson *et al*, Phys. Lett. B **33**, 281 (1970).

[Kan05] R. Kanungo *et al*, Eur. Phys. J. A **25**, 327 (2005).

[Kar03] M. Karny *et al*, Phys. Rev. Lett. **90** 012502 (2003).

[Ket01] H. Kettunen *et al*, Acta Phys. Pol. B **32**, 989 (2001).

[Kle82] O. Klepper *et al*, Zeitschrift für Physik A **305**, 125 (1982).

[Lar83] P. O. Larsson *et al*, Zeitschrift für Physik A, **314**, 9 (1983).

[Len86] W. N. Lennard *et. al.*, Nucl. Instr. Methods A **248**, 454 (1986).

[Lir76] S. Liran and N. Zeldes, At. Data Nucl. Data Tables **17**, 431 (1976).

[Lit05] Yu. A. Litvinov *et al*, Nucl. Phys. A **756**, 3 (2005).

[Liu04] Z. Liu *et al*, Nucl. Instr. Methods A **543**, 591 (2004).

[Liu05] Z. Liu *et al*, Phys. Rev. C **72**, 047301 (2005).

[Liv93a] K. Livingston *et al*, Phys. Rev. C **48**, 3113, (1993).

[Liv93b] K. Livingston *et al*, Phys. Lett. B **312**, 46, (1993).

[Liv96] K. Livingston *et al*, Nucl. Instr. Methods A **370**, 445, (1996).

[Lun03] D. Lunney, J. M. Pearson and C. Thibault, Rev. Mod. Phys. **75**, 1021 (2003).

[Mag98] E. Maglione, L. S. Ferreira and R. J. Liotta, Phys. Rev. Lett. **81**, 538 (1998).

[Mah02a] H. Mahmud, PhD Thesis, University of Edinburgh (2002).

[Mah02b] H. Mahmud *et al*, Eur. Phys. J. A **15**, 85 (2002).

[May49] M. G. Mayer, Phys. Rev **75**, 1969 (1949).

[Mey75] S. L. Meyer, *Data Analysis for Scientists and Engineers*, John Wiley and Sons Inc., New York (1975).

[Moe02] D. P. Moehs *et al*, Rev. Sci. Inst. **73**(2), 576 (2002).

[Mol95] P. Möller *et al*, At. Data Nucl. Data Tables **59**, 185 (1995).

[Mol97] P. Möller, J. R. Nix and K.-L. Kratz, At. Data Nucl. Data Tables **66**, 131 (1997).

[Muk05] I. Mukha *et al*, Phys. Rev. Lett. **95**, 022501 (2005).

[Mun79] G. Münzenberg *et al*, Nucl. Instr. Methods **161**, 65 (1979).

[Mye77] W. D. Myers, *Droplet Model of the Atomic Nucleus*, Plenum, New York (1977).

[Nil55] S. G. Nilsson, Dan. Mat.-Fys. Medd **29**, 16 (1955).

[Nit83] J. M. Nitschke, M. D. Cable and W. D. Zeitz, Zeitschrift für Physik A **312**, 265 (1983).

[Nov02] Y. N. Novikov *et al*, Nucl. Phys. A **697**, 92 (2002).

[Pag92] R. D. Page *et al*, Phys. Rev. Lett. **68**, 1287 (1992).

[Pag94] R. D. Page *et al*, Phys. Rev. Lett. **72**, 1798 (1994).

[Pag96] R. D. Page *et al*, Phys. Rev. C **53**, 660 (1996).

[Pau95] E. S. Paul *et al*, Phys. Rev. C **51**, 78 (1995).

[Pau98] E. S. Paul *et al*, Phys. Rev. C **58**, 801 (1998).

[Pen01] T. Pennington *et al*, Argonne Annual Report 2001, 96 (2001).

[Pfu02] M. Pfutzner *et al*, Eur. Phys. J. A **14**, 279 (2002).

[Poe89] *Particle Emission from Nuclei*, Vol. 3, eds. D. N. Poenaru and M. S. Ivascu, CRC Press Inc., Florida (1989).

[Pol99] G. L. Poli *et al*, Phys. Rev. C **59**, R2979 (1999).

[Pra73] H. C. Pradhan, Y. Nogami and J. Law, Nucl. Phys. A **201**, 357 (1973).

[Rai50] J. Rainwater, Phys. Rev. **79**, 432 (1950).

[Rei85] W. Reisdorf, Zeitschrift für Physik A **444**, 154 (1985).

[Rob03] A. P. Robinson *et al*, Phys. Rev. C **68**, 054301 (2003).

[Rob05a] A. P. Robinson *et al*, Phys. Rev. Lett. **95**, 032502 (2005).

[Rob05b] A. P. Robinson, *et al*, Eur. Phys. J. A **25**, 155 (2005).

[Ryk99] K. Rykaczewski *et al*, Phys. Rev. C **60**, 011301 (1999).

[Sel92a] P. J. Sellin *et al*, Nucl. Instr. Methods A **311**, 217 (1992).

[Sel92b] P. J Sellin, PhD Thesis, University of Edinburgh (1992).

[Sel93] P. J. Sellin *et al*, Phys. Rev. C **47**, 1933 (1993).

[Sew97] D. Seweryniak *et al*, Phys. Rev. C **55**, R2137 (1997).

[Sew99] D. Seweryniak *et al*, Phys. Rev. C **60**, 031304 (1999).

[Sew01a] D. Seweryniak *et al*, Phys. Rev. Lett. **86**, 1458 (2001).

[Sew01b] D. Seweryniak *et al*, Nucl. Phys. A **682**, 247c (2001).

[Sew03] D. Seweryniak *et al*, Acta Phys. Pol. B **34**, 2419 (2003).

[Sew05] D. Seweryniak *et al*, Eur. Phys. J. A **25**, 159 (2005).

[She61] R. K. Sheline, T. Sikkeland and R. N. Chanda, Phys. Rev. Lett. **7**, 446 (1961).

[She69] H. Sherif, Nucl. Phys. A **131**, 532 (1969).

[Son99] A. A. Sonzogni *et al*, Phys. Rev. Lett. **83**, 1116 (1999).

[Sor01] F. Soramel *et al*, Phys. Rev. C **63**, R031304 (2001).

[Sor03] F. Soramel *et al*, *Proc. 2nd Int. Symposium on Proton-Emitting Nuclei*, eds. E. Maglione and F. Soramel, American Institute of Physics (2003).

[Str67] V. M. Strutinsky, Nucl. Phys. A **95**, 420 (1967).

[Str68] V. M. Strutinsky, Nucl. Phys. A **122**, 1 (1968).

[Tan85] I. Tanihata *et al*, Phys. Rev. Lett. **55**, 2676 (1985).

[Tig94] R. J. Tighe *et al*, Phys. Rev. C **49**, R2871 (1994).

[Woo54] R. D. Woods and D. S. Saxon, Phys. Rev. **95**, 577 (1954).

[Woo89] P. J. Woods *et al*, Nucl. Instr. Methods A **276**, 196 (1989).

[Woo97] P. J. Woods and C. N. Davids, Annu. Rev. Nucl. Part. Sci. **47**, 541 (1997).

[Woo04] P. J. Woods *et al*, Phys. Rev. C **69**, 051302 (2004).

[Yor87] J. Yorkston *et al*, Nucl. Instr. Methods A **262**, 353 (1987).

[Xu05] S. W. Xu *et al*, Phys. Rev. C **71**, 054318 (2005).